Summer 8-15-2018

# Development and Application of Hybrid Wray-Agarwal Turbulence Model and Large-Eddy Simulation

Xu Han
*Washington University in St. Louis*

## Recommended Citation

Han, Xu, "Development and Application of Hybrid Wray-Agarwal Turbulence Model and Large-Eddy Simulation" (2018). *McKelvey School of Engineering Theses & Dissertations*. 363.
https://openscholarship.wustl.edu/eng_etds/363

WASHINGTON UNIVERSITY IN ST. LOUIS

School of Engineering & Applied Sciences
Department of Mechanical Engineering & Material Science

Dissertation Examination Committee:
Dr. Ramesh Agarwal, Chair
Dr. Kenneth Jerina
Dr. Mark Meacham
Dr. David Peters
Dr. Palghat Ramachandran

# Development and Application of Hybrid Wray-Agarwal Turbulence Model and Large-Eddy Simulation

by
Xu Han

A dissertation presented to
The Graduate School
of Washington University in
partial fulfillment of the
requirements for the degree
of Doctor of Philosophy

August 2018
St. Louis, Missouri

# Table of Contents

# List of Figures

# List of Tables

# Nomenclature

$A$ = flow variable for demonstrating the hybrid scheme of WA-DES model

*CFD* = Computational Fluid Dynamics

$C_f$ = skin friction coefficient

$C_p$ = pressure coefficient

c = hump length, NACA 4412 chord length, bump length

DES = Detached-Eddy Simulation

DDES = Delayed Detached-Eddy Simulation

$D_1$ = NASA Glenn S-Duct inlet diameter

$d$ = distance to the nearest wall

$\tilde{d}$ = DES length scale of SA-DES model

$F_{DES}$ = characteristic length scale ratio of DES model

$F_{IDDES}$ = characteristic length scale ratio of IDDES model

$f_d$ = shielding function of DDES model

$f_{comp,k}$ = density fluctuation effects of SST $k$-$\omega$ model

$f_{comp,R}$ = density fluctuation effects of WA-DV model

$f_{R\text{-}S}$ = relation function between $R$ and $S$

$f_1$ = blending function of Wray-Agarwal model

$f_\mu$ = wall damping function of Wray-Agarwal model

H = backward facing step height, diffuser inlet height

h = periodic hill height

IDDES = Improved Delayed Detached-Eddy Simulation

$k$ = turbulent kinetic energy

$LES$ = Large Eddy Simulation

$L_R$ = turbulent length scale of WA2018-EB model

$l_{DES}$ = characteristic length scale of DES model

$l_{DDES}$ = characteristic length scale of DDES model

$l_{HYB}$ = hybrid length scale of IDDES model

$l_{k\text{-}\omega}$ = characteristic length scale of SST $k$-$\omega$ model

$l_{LES}$ = characteristic length scale of LES model

$l_{RANS}$ = characteristic length scale of RANS model

$l_{ref}$ = reference length scale of WA2018-EB model

$M$ = Mach number

$P_R$ = transport variable of elliptic blending equation

$P_w$ = wall pressure

$Q_w$ = wall heat flux

$T_w$ = wall temperature

$T'$ = temperature fluctuation

$R$ = undamped eddy viscosity, $k/\omega$

$RANS$ = Reynolds-Averaged Naiver-Stokes

$Re$ = Reynolds number

$S$ = mean strain rate magnitude

$SA$ = Spalart-Allmaras

$SST$ = Shear Stress Transport

$s$ = NASA Glenn S-Duct centerline curve length

$u$ = x-component of velocity

$v$ = y-component of velocity

$W$ = mean vorticity magnitude

$WA$ = Wray-Agarwal

$y^+$ = non-dimensional wall distance

$\Delta$ = grid spacing

$\Delta_{DES}$ = grid spacing of DES model

$\Delta_{IDDES}$ = grid spacing of IDDES model

$\Delta_{WN}$ = grid spacing in wall normal direction

$\varepsilon$ = turbulent dissipation

$\nu$ = molecular kinematic viscosity

$\nu_T$ = turbulent viscosity

$\tilde{\nu}$ = transport variable of Spalart-Allmaras model

$\rho$ = density

$\bar{\rho}$ = mean density

$\rho'$ = density fluctuation

$\rho'^2$ = transport variable of density fluctuation equation

$\omega$ = specific turbulent dissipation rate

# Acknowledgments

I sincerely appreciate the guidance from Dr. Agarwal during my research. This work could not be successfully conducted without unfailing trust, continuous encouragement and professional guidance from an excellent mentor.

I was delighted to receive the efforts and time of my committee members to read the dissertation and provide valuable comments.

I would like to thank my family for their constant love and support. And special thanks to all my friends in CFD lab that make our workplace wonderful.

I would also like to thank the staff of the MEMS department during my time at Washington University.

The financial support for this work was provided by a NASA EPSCoR Grant. It is gratefully acknowledged.

Computations were mainly performed using the facilities of the Washington University Center for High Performance Computing.

Xu Han

*Washington University in St. Louis*

*August 2018*

Dedicated to my family.

## Abstract of the Dissertation

# Development and Application of Hybrid Wray-Agarwal Turbulence Model and Large-Eddy Simulation

by

Xu Han

Doctor of Philosophy in Mechanical Engineering

Washington University in St. Louis, 2018

Research Advisor: Ramesh Agarwal

Rapid development in computing power in past five decades along with the development and progress in building blocks of Computational Fluid Dynamics (CFD) technology has made CFD an indispensable tool for modern engineering analysis and design of fluid-based products and systems. For CFD analysis, Reynolds-Averaged Navier-Stokes (RANS) equations are currently the most widely used fluid equations in the industry. RANS methods require modeling of turbulence effect (i.e. turbulence modeling) based on empirical relations and therefore often produce low accuracy results for many flows. In recent years, the Large Eddy Simulation (LES) approach has been developed which has shown promise of achieving higher accuracy, however it is computationally very intensive and therefore has remained limited to computing relatively simple flows from low to moderate Reynolds numbers. As a result, a hybrid technique called Detached Eddy Simulation (DES) has been proposed in recent years. This technique has shown improved accuracy and computational efficiency for solution of wide variety of complex turbulent flows. The goal of this dissertation has been to develop a DES model based on a recently proposed very promising RANS model, known as the 'Wray-Agarwal (WA)' model and the LES. Decaying Isotropic Turbulence (DIT) case is computed to determine the coefficient in the DES model by matching its energy spectrum with the Kolmogorov spectrum. The new WA-DES model (DES model based on WA model) is applied to compute a wide variety of wall bounded separated flows to assess it accuracy and computational efficiency compared to the widely used RANS turbulence models in the industry, namely the Spalart-Allmaras (SA) and SST $k$-$\omega$ models. Improved Delayed-Detached Eddy Simulation (IDDES) and Elliptic Blending are also considered as further refinements of WA model to improve its accuracy.

# Chapter 1: Introduction

## 1.1 Background and Motivation

Computational Fluid Dynamics (CFD) is playing an important role in modern engineering analysis and design including automobiles, aircrafts, turbomachinery, and many other industrial applications. Almost all flows in industrial applications are turbulent. After more than a century of concerted effort, accurate prediction of turbulent flows still remains a challenging problem even for incompressible wall bounded flows with separation. To date, the solution of Reynolds-Averaged Navier-Stokes (RANS) equations for simulating turbulent flows remains the most widely used approach in industry. The RANS equations include the so called ‘turbulent stresses’ that need to be modeled in order to achieve closure to the equations. Modeling of ‘turbulent stresses’ is called ‘turbulence modeling’ which introduces empiricism and is a major source of difficulty in accurately predicting the turbulent flows. In recent years, higher fidelity approaches namely the Large Eddy Simulation (LES) and Direct Numerical Simulation (DNS) have been developed which have shown promise, however they are computationally very intensive and therefore will remain limited to the computation of relatively simple flows at moderate to low Reynolds numbers respectively in the foreseeable future. As a result, in recent years, hybrid techniques which combine the best features of RANS and LES in a flow domain have been proposed; these techniques have shown improved accuracy and computational efficiency for the solution of 3D complex turbulent flows. These are called the “Detached Eddy Simulation (DES)” methods.

## 1.2 Objectives

The goal of this work is to develop a new DES model based on a recently developed very promising one equation turbulence model based on the k-ω closure, known as the ‘Wray-Agarwal (WA)’ model. The new DES model is designated as the ‘WA-DES’ model. In the boundary layer regions close to the wall, DES model solves the RANS equations while away from the wall in the complex separated flow regions, it employs LES where RANS equations are not quite accurate. In the literature, DES models have been developed based on the widely used one-equation Spalart-Allmaras (SA) model [1] and the two-equation SST $k$-$\omega$ model [2]. The development of WA-DES model requires the accurate determination of a modeling coefficient $C_{DES}$ (which allows the switch between the RANS and LES in the flow) which is determined by simulation of Decaying Isotropic Turbulence (DIT) and matching its energy spectrum with the Kolmogorov spectrum in both the inertial and viscous range. The WA-DES model is applied to compute a variety of wall bounded separated flows, namely the separated flows over a NASA hump and a backward facing step, and inside a diffuser and a S-Duct to assess it accuracy and computational efficiency compared to RANS turbulence models.

Another goal of this work is to refine the original WA model. Currently, the most widely used turbulence models in industry are the SA model and SST $k$-$\omega$ model. SA model provides robustness and efficiency for CFD simulations. SST $k$-$\omega$ model is used for relatively better accuracy compared to SA model. Both models were originally developed in 1980’s and continue to be updated until today. The newly developed WA model, which has been proven to be better in accuracy than SA model and competitive with SST $k$-$\omega$ model in accuracy for a wide variety of flows, still requires adjustments to some of the coefficients and other improvements and extensions due to its relatively very recent origin. In addition to its extension to WA-DES and

WA-IDDES, its baseline original formulation is improved by including a zero strain-rate correction, a wall distance free approach formulation and an elliptic relaxation/blending method.

## 1.3 Outline

The goal of this dissertation is twofold: (1) To extend the WA model to create a validated hybrid WA/LES model, i.e. the WA-DES model and its other variations namely the WA-DDES and WA-IDDES models and (2) to improve the accuracy of original baseline WA model by including a zero strain-rate correction, a wall distance free formulation and an elliptic relaxation/blending method.

A brief summary of various chapters and their content is given below:

**Chapter 2: Turbulence Modeling:** This chapter briefly describe the concept of turbulent flows and turbulence modeling. The two main approaches for computing turbulent flows namely the Reynolds-Averaged Navier-Stokes (RANS) equations with turbulence models and the Large-Eddy Simulation (LES) with a sub-grid scale model are briefly described.

**Chapter 3: Computational Fluid Dynamics:** In this chapter, a brief introduction to computational fluid dynamics (CFD) is given. In particular, the two main software employed in this dissertation for developing and testing the new models, namely the OpenFOAM and Dakota are briefly described. OpenFOAM is used to develop the new models and run the validation cases. Dakota is used to optimize the model coefficients. A brief description of hardware used for CFD calculations is also given.

**Chapter 4: The WA-DES Model:** This chapter gives a brief introduction of Detached-Eddy Simulation (DES), and the Wray-Agarwal (WA) turbulence model, which is combined with LES to derive the Wray-Agarwal Detached-Eddy Simulation (WA-DES) model. The model constant $C_{DES}$ in WA-DES model is calibrated by performing the benchmark test case of Decaying Isotropic Turbulence (DIT) and comparing the WA-DES energy spectrum with Kolmogorov energy spectrum both in inertial and viscous region. Several benchmark validation cases from NASA TMR are computed to show the benefits of this hybrid WA-DES model.

**Chapter 5: The WA-IDDES Model:** A brief introduction of two refinements to DES model, namely the Delayed Detached-Eddy Simulation (DDES) and the Improved Delayed Detached-Eddy Simulation (IDDES) is given in this chapter. DDES approach is discussed and is shown to be not very beneficial as extension of WA-DES. IDDES approach is developed based on WA-DES model to derive the WA-IDDES model. The capability of WA-IDDES model is tested by computing a number of benchmark validation cases from NASA TMR.

**Chapter 6: The Wall Distance Free and Elliptic Blending:** This chapter describes several extensions to the original Wray-Agarwal model (WA2017) to improve its implementation and accuracy. The extensions include (1) modification to the model to remain accurate and robust under the special condition of zero strain-rate in the flow field, (2) a wall distance free (WDF) formulation to provide improved accuracy near curved surfaces, and (3) elliptic blending to improve the accuracy of wall bounded mildly separated flows. The WA model with all the three extensions (WA2018-EB model) is tested on several benchmark test cases.

**Chapter 7: Summary and Future Work:** This chapter provides a summary of the work accomplished in this dissertation, including modeling and testing of the WA-DES, WA-IDDES and WA2018-EB models. The future work describes the density variance correction to the Wray-Agarwal model to extend its capability for computing high speed compressible flows.

# Chapter 2: Turbulence Modeling

## 2.1 Turbulent Flow

### 2.1.1 Laminar and Turbulent Flow

The flow is laminar only at very low Reynolds numbers (the ratio of inertial force and viscous force). Such flows are encountered in very few engineering applications such as those involving very small sizes and velocities, e.g. droplets and bubbles, and in microfluidics and biological applications.  In laminar flows, the flow is considered to move in laminas, and there is little transfer of momentum and energy between the adjacent layers of laminas. However, as the Reynolds number increases, chaotic or random fluctuations occur that result in low momentum diffusion, high momentum convection, and rapid variation in pressure and velocity in space and time in a fluid region. The laminar flows undergo transition to turbulent flows with an extremely complex flow behavior as the Reynolds number increases above a critical value. Both laminar and turbulent flows can be described by the laws of conservation of mass, momentum and energy which are expressed by the continuity equation, momentum equation and energy equation. The governing mass and momentum conservation equations for an incompressible fluid are shown in Eq. (1) below.

$$\begin{gathered} \frac{\partial u_j}{\partial x_j} = 0 \\ \rho \frac{\partial u_i}{\partial t} + \rho u_j \frac{\partial u_i}{\partial x_j} = -\frac{\partial p}{\partial x_i} + \frac{\partial}{\partial x_j}\left(2\mu S_{ij}\right) \end{gathered} \tag{1}$$

### 2.1.2 Separated Flow

Many wall bounded flows encounter separation of turbulent boundary layer attached to the surface because of adverse pressure gradient. When the flow separates, the boundary layer is detached from the solid surface and creates eddies and vortices in the separated flow region.

Depending upon the pressure gradient, the separation region can be small or massive. Pressure drag of the object often increases due to low pressure in the separation region. Separation is very common in industrial applications. For example, separation occurs on airfoils/wings at high angles of attack and behind automobiles and causes large increase in pressure drag. Additionally, at high Mach numbers, the separation can occur due to shock/boundary layer interaction in transonic, supersonic and hypersonic flow. Accurate prediction of wall bounded separated flows remains a challenging task for turbulence models.

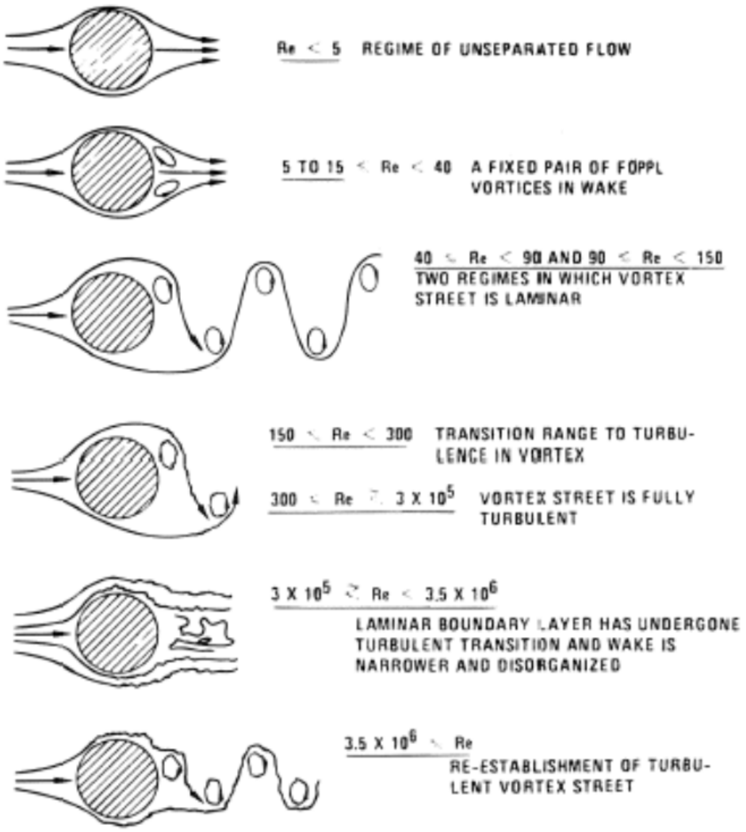

**Figure 2.1: Flow past a circular cylinder at different Reynolds numbers.**

Figure 2.1 shows the evolution of separated flows behind a circular cylinder as Reynolds number increases. Computation of this flow at high Reynolds numbers remains a challenging task to date for all turbulence models used with RANS equations. It is also not possible to calculate the flow at high Reynolds numbers using LES or DNS because of the inadequacy of the computational resources currently available. One of the main objectives of this thesis is to improve the accuracy of turbulence models for predicting wall bounded separated turbulent flows.

## 2.2 Turbulence Modeling

### 2.2.1 Background

Behavior of laminar flow is determined by a single length scale, which mainly comes from the boundaries of the flow region. If one can accurately describe the boundaries of a laminar flow region, the flow behavior in it can be calculated precisely using the Navier-Stokes equations. For very simple geometries and fully developed laminar flows, it has been possible to obtain a few exact analytical solutions of the Navier-Stokes. However, when the flow becomes turbulent, the turbulent fluctuations can only be fully characterized by an infinite number on length and time scales varying from very small to large values.

### 2.2.2 Reynolds-Averaged Navier-Stokes (RANS) Equations

Dating back to early 1900 since Osborne Reynolds, there have been three major approaches that have been developed to model and approximate mathematically the turbulent fluid behavior. The oldest developed in early 1900 is based on time-averaging of the Navier-Stokes equations which results in the Reynolds-Averaged Navier-Stokes (RANS) equations. RANS averaging results in the so called “turbulent stresses” or “Reynolds Stresses” which are unknown and require modeling using empiricism. Thus, RANS equations are not closed; it is known as the “Closure Problem” in RANS equations. Closure of RANS equations requires empirical models for “Reynolds Stresses”; these models are called the “RANS Turbulence Models.” The solution of RANS equations with turbulence models to date remains the most widely used method in industry for solving the turbulent flows.

### 2.2.3 Large-Eddy Simulation (LES)

There are two other approaches that have been developed since 1980s which are more accurate than RANS equations in conjunction with a turbulence model but are computationally very intensive and are still not practical for industrial applications. These are known as the Large Eddy Simulation (LES) and the Direct Numerical Simulation (DNS). The Sub-Grid Scale (SGS) model is used in LES to reduce the computational cost. In LES, the velocity field is filtered to separate the motion of large and small eddies. Only the large eddies are resolved directly without modeling, however the smaller eddies require modeling. The models used to characterize the small eddies are called the Sub-Grid Scale (SGS) models. Most well-known among them are the Smagorinsky model [3] and Germano model [4] among others. LES has a much higher level of accuracy compared to RANS but is computationally expensive, especially for computing turbulent boundary layers. In DNS, all the length scales, from the largest down to the Kolmogorov scale where the turbulent kinetic energy is dissipated to heat, the turbulent flow is resolved by solving the Navier-Stokes equations directly without any modeling. DNS is the most accurate method but has the highest computational cost and requires enormous computing power which is currently possible and affordable only for calculating flows at low Reynolds number for very simplest geometries [5]. As mentioned before, most of the industrial flows in complex 3D geometries are currently computed using the RANS equations with a turbulence model.

# Chapter 3: Computational Fluid Dynamics

## 3.1 Introduction

Experimental and theoretical methods are the two main traditional approaches for solving the fluid mechanic and heat transfer problems. With the rapid development of digital computers since 1950's. It is now feasible to solve almost routinely in most cases the ordinary and partial differential equations numerically. The numerical solution at the same time, has been aided by the software developments including Computer-Aided Design (CAD), finite-difference/finite-volume/finite-element methods and data reduction visualization techniques, etc. Making use of these developments in hardware and software, CFD has now become the third and the most widely used main method for solving fluid dynamics problems.

Currently, CFD has been successfully used in a large number of industrial applications and it now keeps on growing at a faster pace. The fundamental transport equations solved in a CFD code are being reinvestigated by data science methodology due to the availability of large data sets along with the development of statistical methods [6]. In addition, heterogenous systems implemented with accelerators like Graphical Processing Units (GPUs) have helped in improving the runtime of the time-consuming parts (mostly the iterative matrix multiplications) using massive parallelization [7]. With the development of physical modeling, mathematics/numerical methods and computer science, the future of CFD appear to be more promising than ever before.

## 3.2 Software

### 3.2.1 OpenFOAM

In this research, the CFD flow solver OpenFOAM (Open source Field Operation And Manipulation) is employed. OpenFOAM is an open source CFD software developed on Linux operating system. It was initially released in 2004 and continues to be developed by addition of all kind of CFD capability in complex fluid physics modeling, type of grids and numerical algorithms, and turbulence models. It includes the most well-known turbulence models namely the SA model, SST $k$-$\omega$ model, and $k$-$\epsilon$ model among others. It can therefore be used for wide range of applications, including incompressible and compressible turbulent flows, buoyancy-driven flows, multiphase flows, and application with heat transfer, combustion and particle dynamics etc.

In contrast to commercial CFD software such as ANSYS Fluent, COMSOL, STAR-CD etc., OpenFOAM provides the source code which makes it easy to modify it by adding needed capability to solve a particular problem. It has been developed in C++ programming language which has many good features like modularity and extensibility. Users can easily and effectively develop and test the new CFD capability. The commercial CFD software only provides the executable code which requires the development and implementation of a User Defined Function (UDF) to add new capability which is a tedious process.

In this work, all the simulations are performed using OpenFOAM, and the new models are developed and implemented as OpenFOAM libraries. Some of the simulation cases (e.g. flat plate, NASA hump, etc.) are also performed in ANSYS fluent, and FUN3D (NASA CFD code) to be verification of simulation result. All the three codes yield the same CFD results for flow quantities such as the velocity profiles, pressure coefficients and skin-friction coefficients in different flow configurations.

### 3.2.2 Dakota

In order to investigate and optimize the coefficients of new models developed in this work, another open source software called Dakota is used for optimization of the coefficients. Dakota served as an interface between the CFD code and the iterative system analysis method. As a result, its flexibility and extensibility allow the user to analyze any “black box” even though the robustness is usually not guaranteed. The algorithms contained in Dakota include: gradient-based and non-gradient-based methods; uncertainty quantification with sampling, reliability, and stochastic expansion methods; parameter estimation with nonlinear least squares methods; and sensitivity/variance analysis with design of experiments and parameter study methods [8].

The effect of coefficients in WA model has been previously investigated using uncertainty qualifications based on non-intrusive Polynomial Chaos Expansion (PCE) method [9]. In this research, the coefficients of the new models are optimized by the NL2SOL algorithm in order to minimize the difference between the experimental data and the model outputs. The NL2SOL algorithm is a non-linear least-squares algorithm, which is significantly more efficient than generally used optimization algorithms when user can provide the gradients of each term in the sum-of-squares [8]. However, this algorithm can only provide the local optimization result. The global optimal result is approximated by dramatically changing the initial guess of the coefficient, but not applying any expensive general global optimizer such as a genetic algorithm.

## 3.3 Hardware

Most of the computations in this research have been performed on the computing cluster at the Center for High-Performance Computing (CHPC) of Mallinckrodt Institute of Radiology at Washington University School of Medicine in St. Louis [10]. CHPC provides access to high performance computing resources for computationally intensive scientific projects. The cluster contains 2,500 high speed CPU cores, 17TB of combined memory, 74 Tesla-class GPUs and 150TB of internal high speed shared storage.  Software package (e.g. OpenFOAM) installation and code parallelization support is also provided via CHPC staff.

# Chapter 4: The WA-DES Model

## 4.1 Introduction

### 4.1.1 Detached-Eddy Simulation

Detached-Eddy Simulation (DES) is a hybrid turbulence modeling method first proposed in 1997 by Spalart et al. [1], aimed at predicting the massive flow separation at high Reynolds number without a significant increase in computational cost. DES is a combination of RANS and LES methods. In the separation region, DES is designed to run in the LES mode; its turbulent viscosity becomes a function of local grid spacing which is determined by a SGS model such as the Smagorinsky-Lilly model. Outside the separation regions, especially in the turbulent boundary layer, DES runs in the RANS mode. As a result, DES only needs fine LES type grid in the separation region, and thus the high computational cost of LES computation in the boundary layer is avoided by running RANS equations on coarse grids.

The first DES model called DES97 was based on the well-known one equation Spalart-Allmaras (SA) turbulence model. It was defined as "a three-dimensional unsteady numerical solution technique using a single turbulence model, which functions as a sub-grid-scale model in regions where the grid density is fine enough for a large-eddy simulation, and as a Reynolds-averaged model in other regions" [11]. The switch between RANS and LES is determined by their length scales: wall distance in the SA model and the grid spacing in LES. Recently DES models have been developed for the two equation SST $k$-$\omega$ model [2] and the four equation $v^2$-$f$ model [12]. Additionally, Delayed Detached-Eddy Simulation (DDES) and Improved Delayed Detached-Eddy Simulation (IDDES) are being developed to refine the original DES method.

## 4.2 Review of the SA-DES, SST-DES and WA Turbulence Model

### 4.2.1 Review of the SA-DES Model

The Spalart-Allmaras (SA) turbulence model is a well-known widely used model for the solution of RANS equations. It is a one-equation model originally designed for aerodynamic applications with wall-bounded flows at low Reynolds number [13]; however, it has been also widely used for computing many turbulent flows in all kinds of industry. In SA model, a viscosity-like variable $\tilde{\nu}$ is introduced, which is proportional to the turbulent viscosity.

$$\mu_t = \rho\tilde{\nu}f_{v1} \tag{2}$$

The transport equation for $\tilde{\nu}$ is derived by empiricism and arguments of dimensional analysis. It contains a destruction term which decreases with increase in the wall distance. Compared to other well-known turbulence models such as SST *k*-*ω* and *k*-$\epsilon$, SA model sometime is less in accuracy but is very efficient and shows better convergence and stability in computations. The equation of SA model is given in Eq. (3).

$$\begin{aligned}\frac{\partial\tilde{\nu}}{\partial t} + u_j\frac{\partial\tilde{\nu}}{\partial x} = c_{b1}(1-f_{t2})\tilde{S}\tilde{\nu} - \left[c_{w1}f_w - \frac{c_{b1}}{\kappa^2}f_{t2}\right]\left(\frac{\tilde{\nu}}{d}\right)^2 \\ + \frac{1}{\sigma}\left[\frac{\partial}{\partial x_j}\left((\nu+\tilde{\nu})\frac{\partial\tilde{\nu}}{\partial x_j}\right) + c_{b2}\frac{\partial\tilde{\nu}}{\partial x_i}\frac{\partial\tilde{\nu}}{\partial x_i}\right]\end{aligned} \tag{3}$$

The SA-DES model is the first DES type model reported in the literature. SA-DES model replaces wall distance *d* in SA model with a new length scale $\tilde{d}$ defined as:

$$\tilde{d} = min(d, C_{DES}\Delta) \tag{4}$$

In Eq. (4), $C_{DES}$ is a constant and $\Delta$ is the largest grid spacing among the three coordinate directions.

$$\Delta = max(\Delta_x, \Delta_y, \Delta_z) \tag{5}$$

In the near wall region, the wall distance is very small and the DES length scale $\tilde{d}$ is equal to the original length scale *d* in the SA model; SA-DES model has the same behavior as SA. These regions are usually the turbulent boundary layers. As the wall distance increases, the DES length scale gradually changes to the LES length scale $C_{DES}\Delta$ and results in a turbulent viscosity given by the Smagorinsky type model.

$$\mu_t \sim \rho S \Delta^2 \tag{6}$$

### 4.2.2 Review of the SST-DES Model

Menter's Shear Stress Transport (SST) k-ω model is another widely used linear eddy viscosity turbulence model developed by combining the *k-ω* and *k-ε* models [14]. It is a two-equation model using the transport equations for turbulent kinetic energy *k* and the specific dissipation rate *ω*. In the SST model, the $F_1$ function in the model switches the equations to the *k-ω* type model in the near wall region and *k-ε* type model in the free stream region. It avoids the problem of *k-ω* model being too sensitive to the inlet free stream turbulence properties and preserves its accuracy in the regions away from the wall. The equations of SST *k-ω* model are shown in Eq. (7).

$$\begin{gathered}\frac{\partial k}{\partial t} + U_j \frac{\partial k}{\partial x_j} = P_k - \beta^* k\omega + \frac{\partial}{\partial x_j}\left[(\upsilon + \sigma_k \upsilon_T)\frac{\partial k}{\partial x_j}\right] \\ \frac{\partial \omega}{\partial t} + U_j \frac{\partial \omega}{\partial x_j} = \alpha S^2 - \beta\omega^2 + \frac{\partial}{\partial x_j}\left[(\upsilon + \sigma_\omega \upsilon_T)\frac{\partial \omega}{\partial x_j}\right] + 2(1 - F_1)\sigma_{\omega 2}\frac{1}{\omega}\frac{\partial k}{\partial x_i}\frac{\partial \omega}{\partial x_i}\end{gathered} \tag{7}$$

The turbulent viscosity of SST *k*-*ω* model is defined by the turbulent kinetic energy and the specific dissipation rate as follows:

$$\mu_t = \frac{a_1 \rho k}{max(a_1 \omega, SF_2)} \tag{8}$$

Even though the SST *k*-*ω* model is often considered a better way to predict flows with adverse pressure gradients and separation, the simulation results are still poor compared to LES. SST-DES model therefore was developed by again switching the length scale between RANS and LES.

$$\begin{gathered} l_{DES} = min(l_{k-\omega}, C_{DES}\Delta) \\ l_{k-\omega} = \frac{\sqrt{k}}{\beta^* \omega} \end{gathered} \tag{9}$$

In Eq. (9), $\beta^*$ and $C_{DES}$ are constants defining the RANS and LES length scale, respectively. The dissipative term in *k*-equation is modified to generate the Smagorinsky-like turbulent viscosity when the model is operating in LES mode. In RANS regions, this transport equation is the same as in the original SST *k*-*ω* model. The *k*-equation of SST-DES model is shown in Eq. (10).

$$\frac{\partial k}{\partial t} + U_j \frac{\partial k}{\partial x_j} = P_k - \frac{k^{3/2}}{l_{k-\omega}} + \frac{\partial}{\partial x_j}\left[(\upsilon + \sigma_k \upsilon_T)\frac{\partial k}{\partial x_j}\right] \tag{10}$$

### 4.2.3 Review of the WA RANS Model

The recently developed Wray-Agarwal model [15], designated as (WA2017) is a new one-equation linear eddy-viscosity turbulence model derived from *k*-*ω* closure. In this model, a new variable *R* is introduced which is defined as *k*/*ω*. It includes a cross diffusion term and a blending function $f_1$ to switch between the two destruction terms. The equation of WA2017 model is shown in Eq. (11).

$$\frac{\partial R}{\partial t}+\frac{\partial u_j R}{\partial x_j}=\frac{\partial}{\partial x_j}\left[(\sigma_R R+\nu)\frac{\partial R}{\partial x_j}\right]+C_1 RS+f_1 C_{2k\omega}\frac{R}{S}\frac{\partial R}{\partial x_j}\frac{\partial S}{\partial x_j} - (1-f_1)C_{2k\varepsilon}R^2\left(\frac{\frac{\partial S}{\partial x_j}\frac{\partial S}{\partial x_j}}{S^2}\right) \tag{11}$$

The turbulence eddy viscosity is given by the equation:

$$\nu_T = f_\mu R \tag{12}$$

The wall blocking effect is accounted for by the damping function $f_\mu$. The value of $C_w$ was determined by calibrating the model to a simple zero pressure gradient flat plate flow. $\nu$ has the usual definition of dynamic viscosity.

$$f_\mu = \frac{\chi^3}{\chi^3+{C_w}^3}, \qquad \chi = \frac{R}{\nu} \tag{13}$$

*S* is the mean strain described below.

$$S = \sqrt{2S_{ij}S_{ij}}\,, \qquad S_{ij} = \frac{1}{2}\left(\frac{\partial u_i}{\partial x_j}+\frac{\partial u_j}{\partial x_i}\right) \tag{14}$$

The model can behave either as a one equation *k-ω* or one equation *k-ε* model based on the switching function $f_1$. The switching function $f_1$ is limited by an upper value of 0.9 for better stability.

$$f_1 = min(tanh(arg_1^4), 0.9) \tag{15}$$

$$arg_1 = \frac{1+\frac{d\sqrt{RS}}{\nu}}{1+\left[\frac{max\left(d\sqrt{RS}, 1.5R\right)}{20\nu}\right]^2} \tag{16}$$

The values of constants used in WA2017 model are listed below [16].

$$\begin{gathered}
C_{1k\omega} = 0.0829 \quad C_{1k\varepsilon} = 0.1127 \\
C_1 = f_1(C_{1k\omega} - C_{1k\varepsilon}) + C_{1k\varepsilon} \\
\sigma_{k\omega} = 0.72 \quad \sigma_{k\varepsilon} = 1.0 \\
\sigma_R = f_1(\sigma_{k\omega} - \sigma_{k\varepsilon}) + \sigma_{k\varepsilon} \\
\kappa = 0.41 \\
C_{2k\omega} = \frac{C_{1k\omega}}{\kappa^2} + \sigma_{k\omega} \quad C_{2k\varepsilon} = \frac{C_{1k\varepsilon}}{\kappa^2} + \sigma_{k\varepsilon} \\
C_w = 8.54
\end{gathered} \tag{17}$$

The WA model has shown improved accuracy over the SA model and has been found to be competitive with the SST *k-ω* model for a wide variety of wall-bounded and free shear layer flows [16]. Being a one equation model, it has the advantage in efficiency over multi-equation models in computational cost. Even though the WA2017 model appears promising, it also has limitations in accuracy for computing wall bounded separated flows.

## 4.3 Technical Approach for Developing WA-DES Model

### 4.3.1 Formulation of the WA-DES Model

The very first DES model, the DES97 based on the SA model switches between RANS and LES by comparing the length scales between the two. The length scale of the SA model, wall distance *d*, is compared to the LES length scale, grid spacing Δ and the DES model behaves as LES when the grid is fine enough [17]. The general definition of the DES length scale is:

$$l_{DES} = min(l_{RANS}, l_{LES}) \equiv min(l_{RANS}, C_{DES}\Delta) \tag{18}$$

We need to determine the length scale of the WA model. The turbulence length scale is a physical quantity describing the size of eddies containing large amount of energy. In the SST *k-ω* model, the length scale is defined by *k* and *ω* as given in Eq. (9). Since the WA model is derived from *k-ω* closure, we can use a similar definition for *R* defined as *k*/*ω* in the derivation of WA-DES model [18]. The final step is to implement the DES length scale into the WA equation.

After the implementation, the equation should have a Smagorinsky-like turbulent viscosity when the model is operating in LES mode. The simplest approach is to make the resulting eddy viscosity of the form of $S\Delta^2$. In the RANS mode, the equation should remain the same as the original WA equation. The equation of WA-DES model is formulated as:

$$\frac{\partial R}{\partial t} + \frac{\partial u_j R}{\partial x_j} = \frac{\partial}{\partial x_j}\left[(\sigma_R R + \nu)\frac{\partial R}{\partial x_j}\right] + C_1 RS + f_1 C_{2k\omega}\frac{R}{F_{DES}^2 S}\frac{\partial R}{\partial x_j}\frac{\partial S}{\partial x_j} - (1 - f_1) C_{2k\varepsilon}\frac{R^2}{F_{DES}^2}\left(\frac{\frac{\partial S}{\partial x_j}\frac{\partial S}{\partial x_j}}{S^2}\right) \tag{19}$$

In Eq. (19), $F_{DES}$ is the characteristic length scale ratio.

$$F_{DES} = \max\left(\frac{l_{RANS}}{l_{LES}}, 1\right) \tag{20}$$

$$l_{RANS} = \sqrt{\frac{R}{S}} \tag{21}$$

$$\begin{gathered} l_{LES} = C_{DES}\Delta_{DES} \\ \Delta_{DES} = max\left(\Delta_x, \Delta_y, \Delta_z\right) \end{gathered} \tag{22}$$

### 4.3.2 Calibration of the WA-DES Model

To calibrate the DES constant $C_{DES}$, the simulation of decaying isotropic turbulence (DIT) is performed. This is a standard test case used in determining $C_{DES}$ in the DES models; it matches the computed energy spectrum of isotropic turbulence from DES model with the Kolmogorov energy spectrum. A cubic computational domain is employed which has sides of length $L_{BOX}$ = $2\pi$ with periodic boundary conditions in all directions. The initial velocity field employs the $32^3$ truncations of $512^3$ DNS data of Wray [19] at $Re_\lambda = 104.5$. Quantities in the DES model are initialized by running the Smagorinsky LES model for some time with the frozen initial velocity field. After the initialization, WA-DES model is forced to run in the LES mode ($F_{DES} = \frac{l_{RANS}}{l_{LES}}$) using a central difference convection scheme for 30 large eddy turnover time. The resulting energy spectrum is compared to the DNS data as shown in Figure 4.1. The line labeled '-5/3' is the theoretical Kolmogorov data corresponding to its prediction that *E(k)* is proportional to $k^{-5/3}$. The calibrated value of $C_{DES}$ is 0.41.

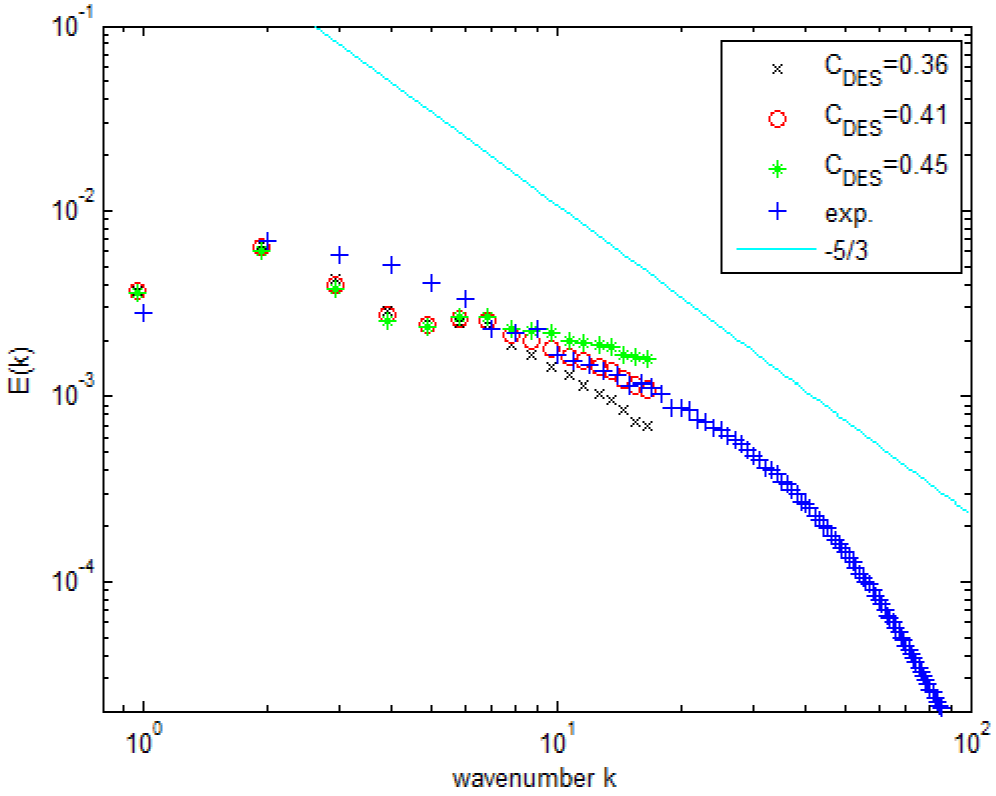

**Figure 4.1: Decaying Isotropic Turbulence test for WA-DES model.**

## 4.4 Numerical Schemes for WA-DES Model

The choice of the numerical schemes is very important for accurate CFD simulations. LES equations require high order schemes. For time integration 2nd order backward difference scheme is adequate. However, for spatial discretization, the truncation error of the low order scheme can be of the same order as the grid spacing, which is used as a length scale in the DES model.

Furthermore, even order schemes are desirable since they are less dissipative and do will not affect the accuracy of the SGS model significantly. The 2$^{nd}$ order central differencing scheme is a standard choice for spatial discretization of LES.

However, the central differencing scheme can lead to oscillations in the solution and may cause divergence when the grid is not fine enough. In DES, equations operate in RANS mode in the coarse grid region. The 2$^{nd}$ order upwind scheme can avoid this problem, and also ensure the 2$^{nd}$ order accuracy. As a result, one needs to employ a hybrid numerical scheme for DES. A variable $F_{DES}$ defined in Eq. (20) is used to interpolate the central differencing scheme and the 2nd order upwind scheme by comparing the length scales of RANS and LES. As $F_{DES}$ increases from 0 to 1, the DES model changes from RANS to LES and the hybrid scheme will gradually switch from 2nd order upwind to central differencing. For example, flow variable $A$ is calculated by:

$$A = \frac{1}{F_{DES}} A_{2ndUpwind} + \left(1 - \frac{1}{F_{DES}}\right) A_{CentralDifference} \tag{23}$$

## 4.5 Validation Cases

### 4.5.1 Flat Plate Flow

Since the WA-DES model is being implemented in OpenFOAM for the first time, it is necessary to verify that the implementation has been done correctly. First, the case of flow on a flat plate is computed to test the ability of WA-DES model to reproduce the physics of this simple flow.

The flat plate flow is a basic verification/validation case for any turbulence model. A cross section of the computational setup is shown in Figure 4.2 [20]. The plate was extended one meter from the inflow boundary to reduce its influence. Periodic boundary condition in z-direction is used for the LES part in DES. Computational results for wall skin friction coefficient ($C_f$) vs.

Reynolds number *Re* in *x* direction ($Re_x$) are compared to the experimental data. $Re_x$ is a function of *x* defined as:

$$Re_x = \frac{\rho_\infty U_\infty x}{\mu_\infty} \tag{24}$$

The prediction of skin friction is of particular interest in this case. It can be seen from Figure 4.3 that the WA-DES model matches the computed skin friction coefficient data with the experimental results [21] quite well.

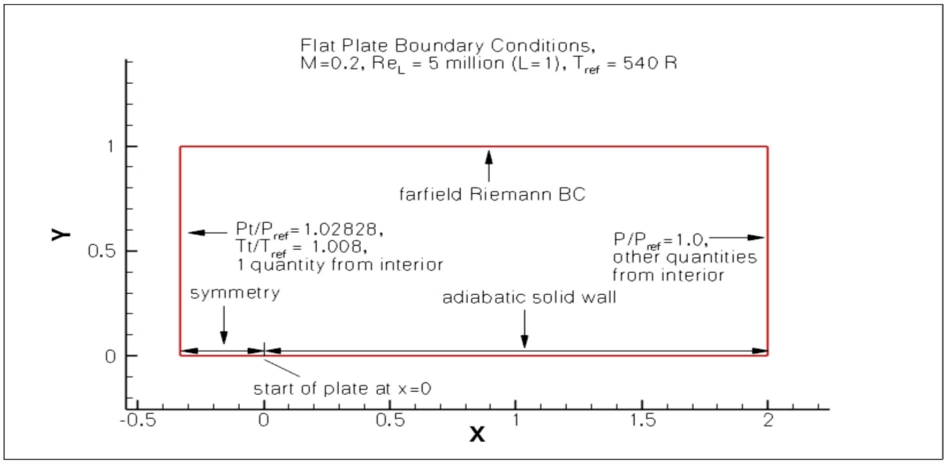

Figure 4.2: Flow past a flat plate in zero pressure gradient [20].

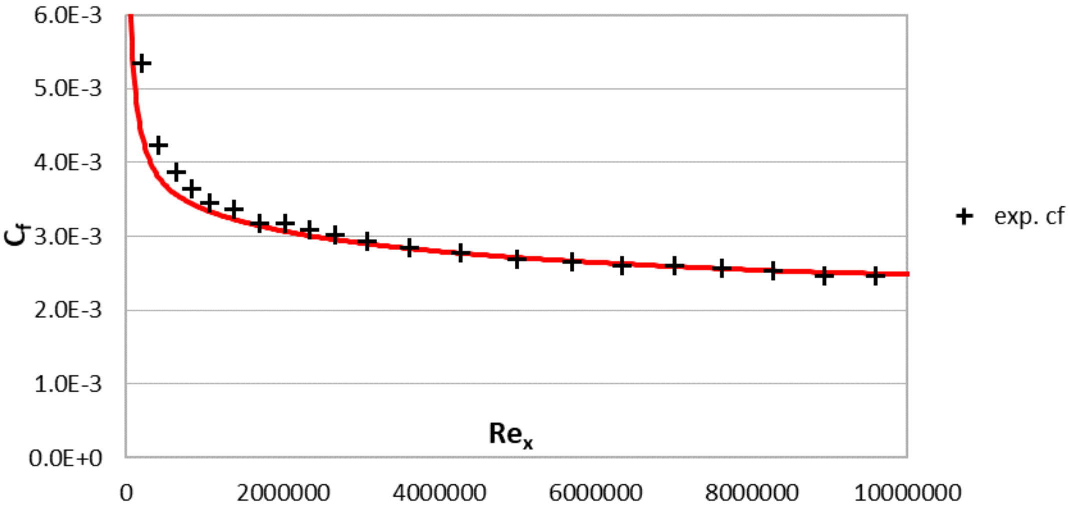

**Figure 4.3: Comparison of computed skin friction distribution on the flat plate using the WA-DES model with the experimental data.**

### 4.5.2 Flow past NACA0012 Airfoil

Subsonic flow past a NACA0012 airfoil is used as another validation case for the new WA-DES model. The freestream Mach number is 0.15 and the Reynolds number based on the Chord length is Re = 6 million. The angle of attack is 10 degrees. In the simulation, the outermost boundary of the computational domain is at 25 chords upstream from the leading edge of the airfoil. Surface pressure coefficients data from the experiment of Ladson et al. [22] is used to compare the simulations. The result from WA-DES model matches the experimental data quite well.

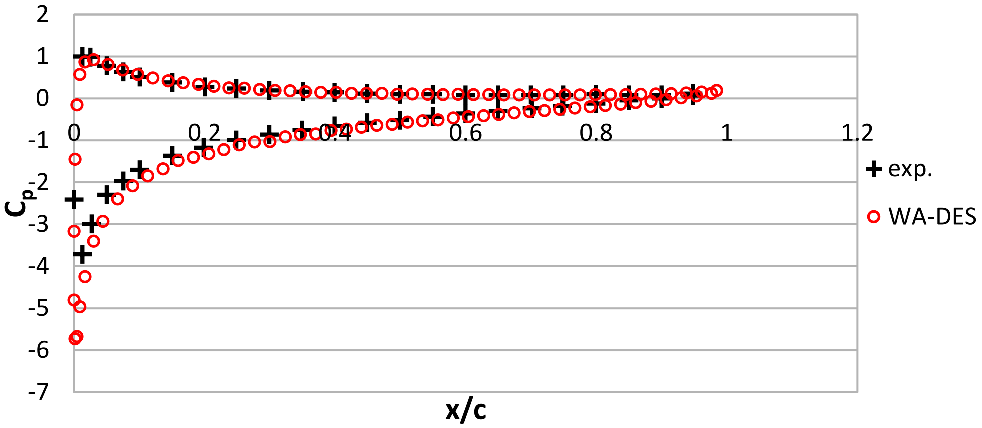

**Figure 4.4: Comparison of computed pressure distribution with WA-DES model on the surface of NACA 0012 airfoil with experimental data.**

### 4.5.3 Flow over NASA Wall-Mounted Hump

Figure 4.5 shows the geometry of the NASA wall-mounted hump with computational domain and boundary conditions [20]. The freestream Mach number is 0.1 and Reynolds number based on hump chord length is $Re_c$ = 936,000. This is a challenging case for testing the accuracy of various turbulence models.

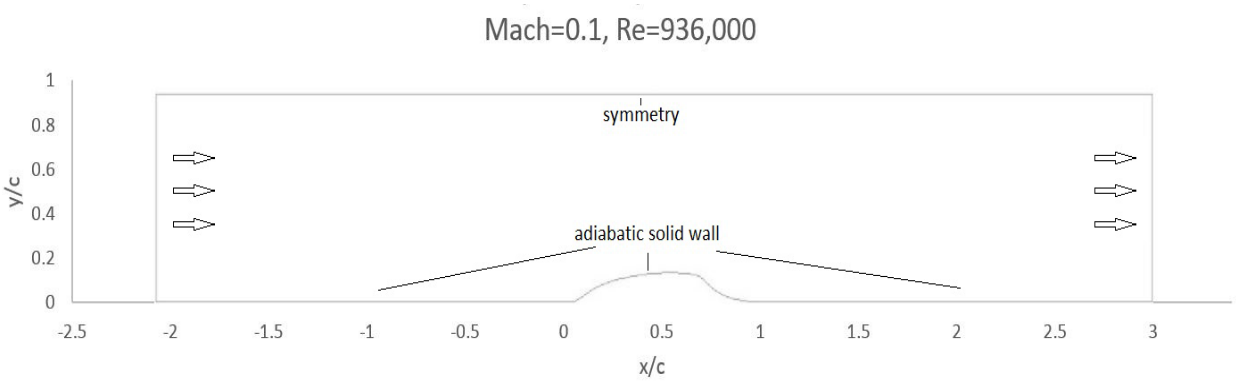

**Figure 4.5: Geometry of NASA wall-mounted hump, computational domain and boundary conditions.**

Figure 4.6 shows the comparison of computed pressure distribution obtained using the WA-DES model, WA model and SA model with the experimental data. Figure 4.7 shows the comparison of computed skin-friction distribution obtained using the same models and experimental data. It can be noted that the WA-DES model predicts the pressure distribution in most regions of the flow field quite well. From the skin friction distribution plot, it can be noted that the predicted separation occurs at x/c = 0.666 and reattachment at x/c = 1.12. These values are very close to the experimental data for separation and reattachment at 0.665 and 1.1 respectively. WA model and SA model over-predict the reattachment point at x/c = 1.4 and 1.3 respectively.

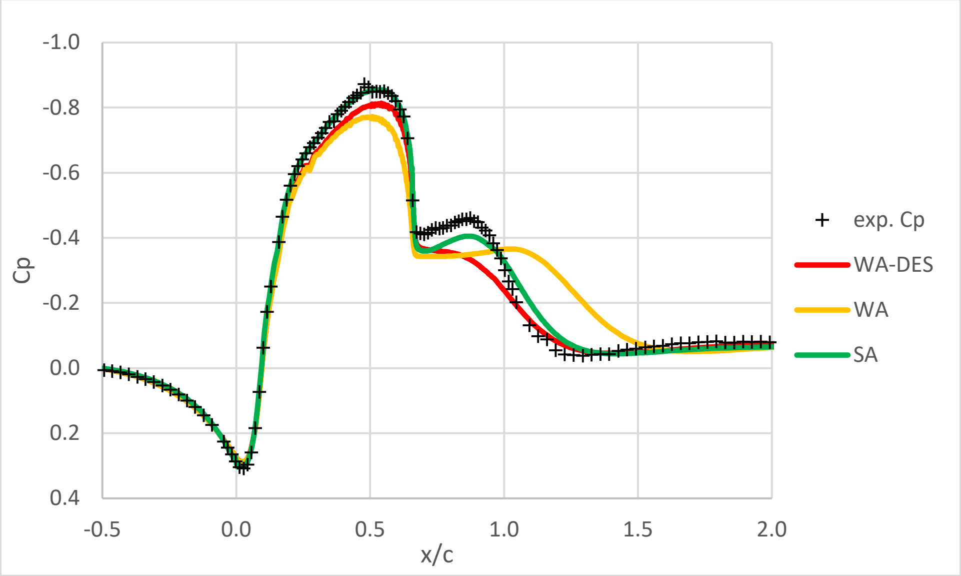

**Figure 4.6: Comparison of pressure distribution on the surface of the hump.**

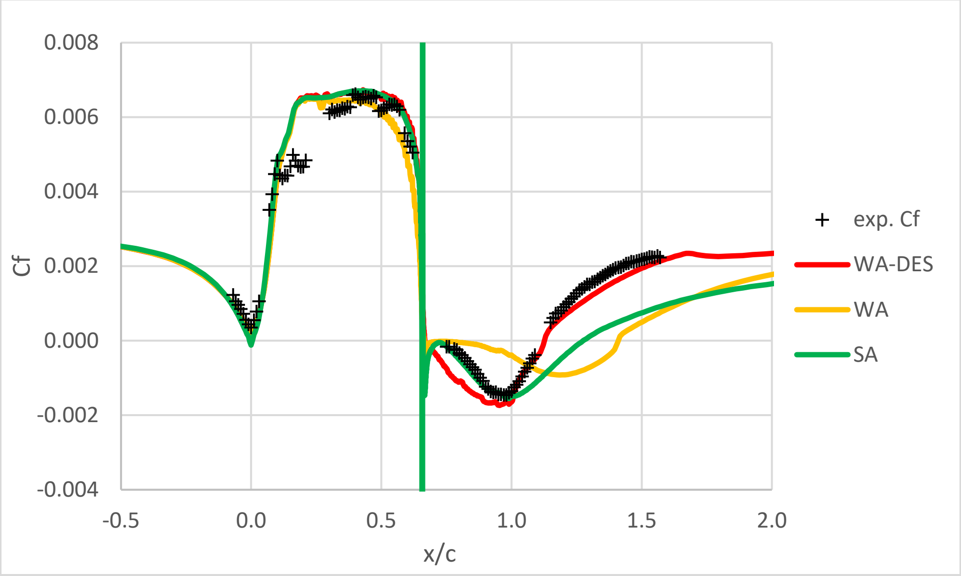

**Figure 4.7: Comparison of Skin-Friction distribution on the surface of the hump.**

Comparisons of the predicted velocity profiles from WA-DES, WA and SA models and experimental data are shown in Figure 4.8, Figure 4.9 and Figure 4.10 respectively. It can be seen that the velocity profiles predicted by the WA-DES model agree quite well with the experimental data before and through the separation region. Downstream of the separation, recovery is slower than expected but it is still faster than that obtained with WA and SA models. Overall the results obtained using the WA-DES model are much more accurate than those obtained with conventional eddy-viscosity models [20].

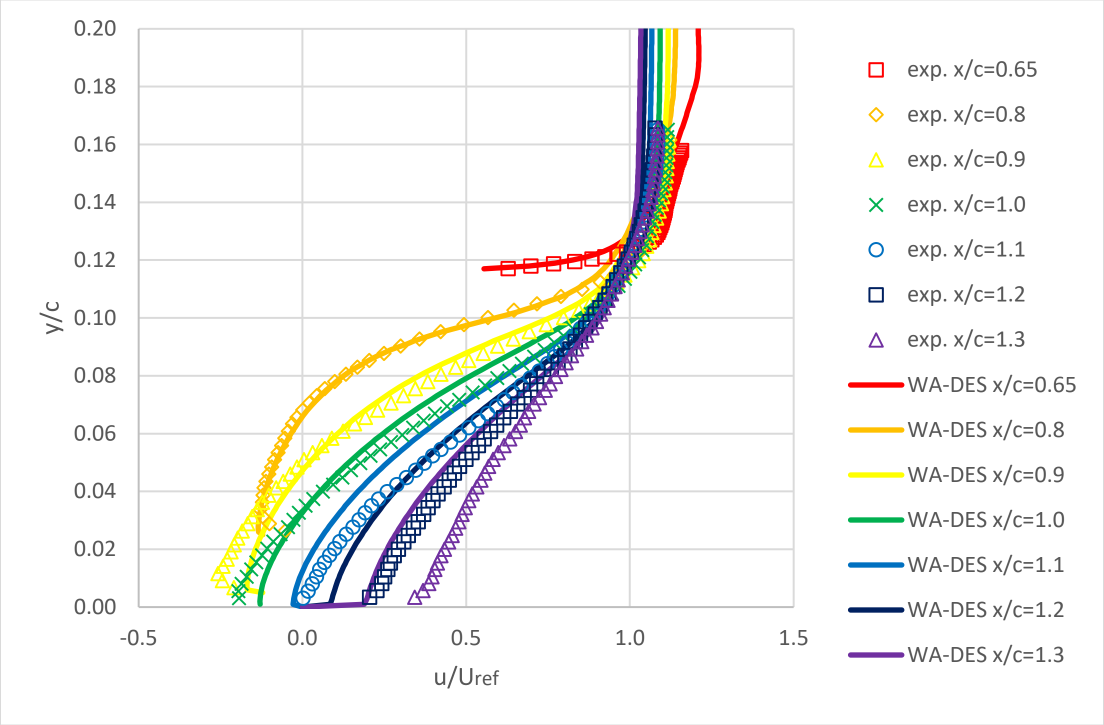

**Figure 4.8: Comparison of velocity profiles from WA-DES model and experimental values at various locations on the hump.**

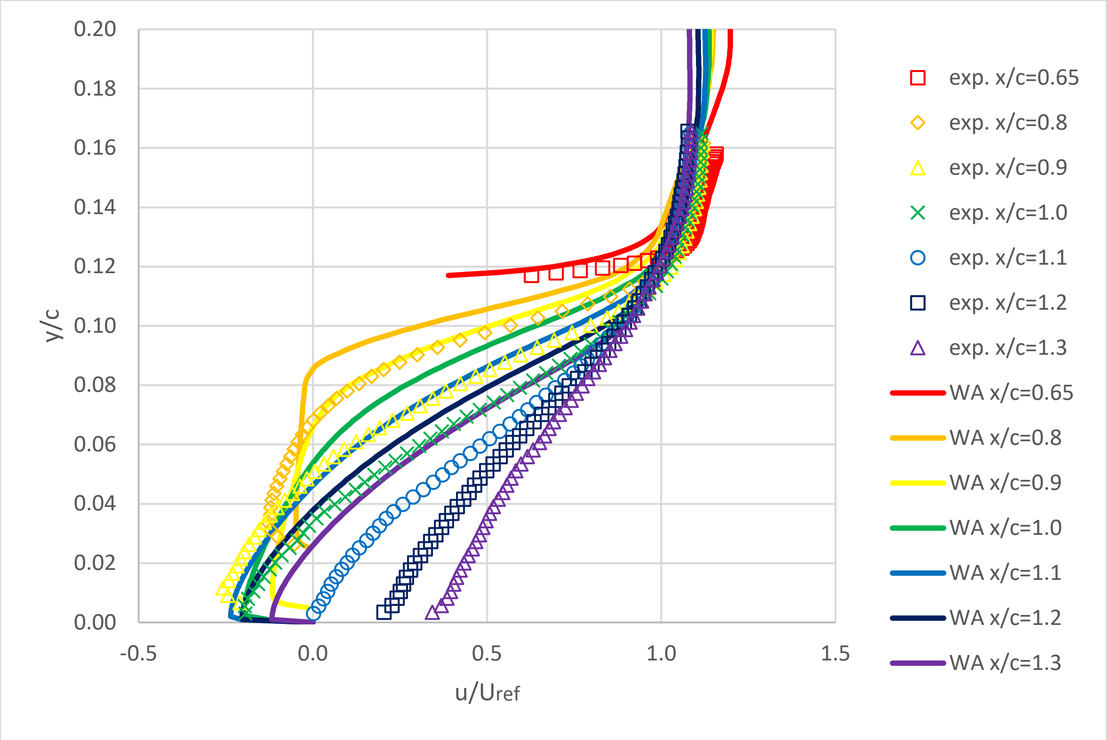

**Figure 4.9: Comparison of velocity profiles from WA model and experimental values at various locations on the hump.**

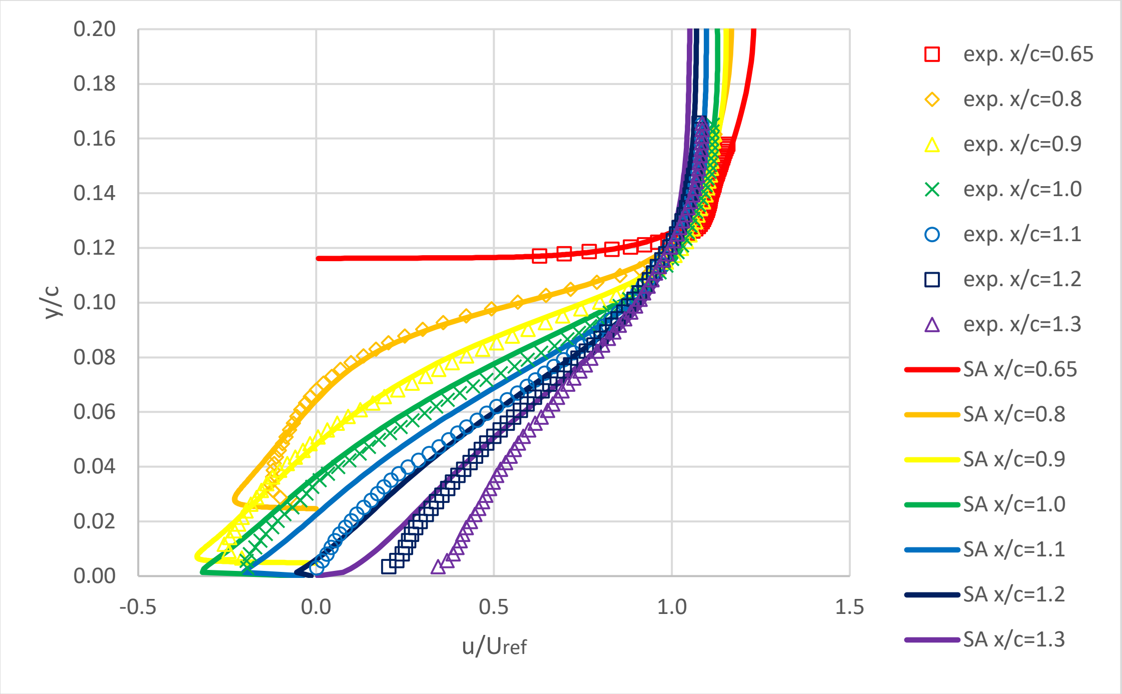

**Figure 4.10: Comparison of velocity profiles from SA model and experimental values at various locations on the hump.**

### 4.5.4 Flow over a Backward Facing Step

In flow over a backward facing step, a sudden back step is encountered by the flow resulting in flow separation. Figure 4.11 shows the geometry of the backward facing step and corresponding boundary conditions [20]. The Mach number at reference point (x/H = -4) is 0.128 and the Reynolds number based on the step height is 36,000. This is a typical benchmark case for testing the ability of the turbulence models in predicting flow separation.

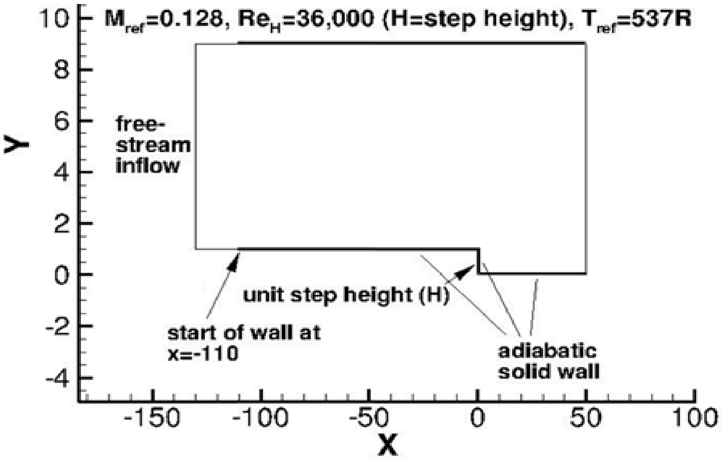

**Figure 4.11: Geometry of backward facing step, computational domain and boundary conditions [20].**

Figures 4.12 and 4.13 show the pressure distribution and skin friction coefficient respectively computed by the WA-DES model and their comparison with the experimental data. The computed reattachment point is at x/H = 6.24 by WA-DES model compared to the experimental location range from 6.16 to 6.36. Pressure distribution and skin friction coefficient predicted by the WA-DES model generally match the experimental data, and show improved accuracy over WA model. Figures 4.14, 4.15 and 4.16 show the comparison of computed velocity profiles obtained using the WA-DES, WA and SA model with the experimental data, respectively. Velocity profiles from WA-DES and WA models at x/H = 1 and x/H = 4 are closer to the experimental results compared to the SA model, but the discrepancy between the computations and experimental data becomes larger when the flow approaches and moves beyond the reattachment point (e.g. at x/H = 6 and 10). The WA-DES model generally gives the same results as the WA model; both show good agreement with the experimental data.

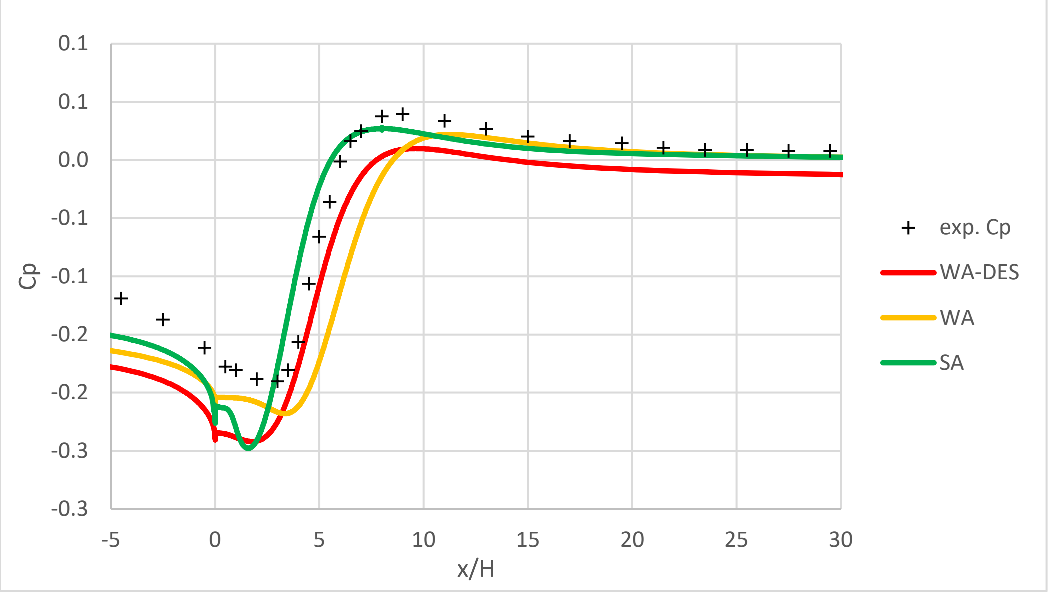

Figure 4.12: Comparison of pressure distribution on the surface of the backward facing step.

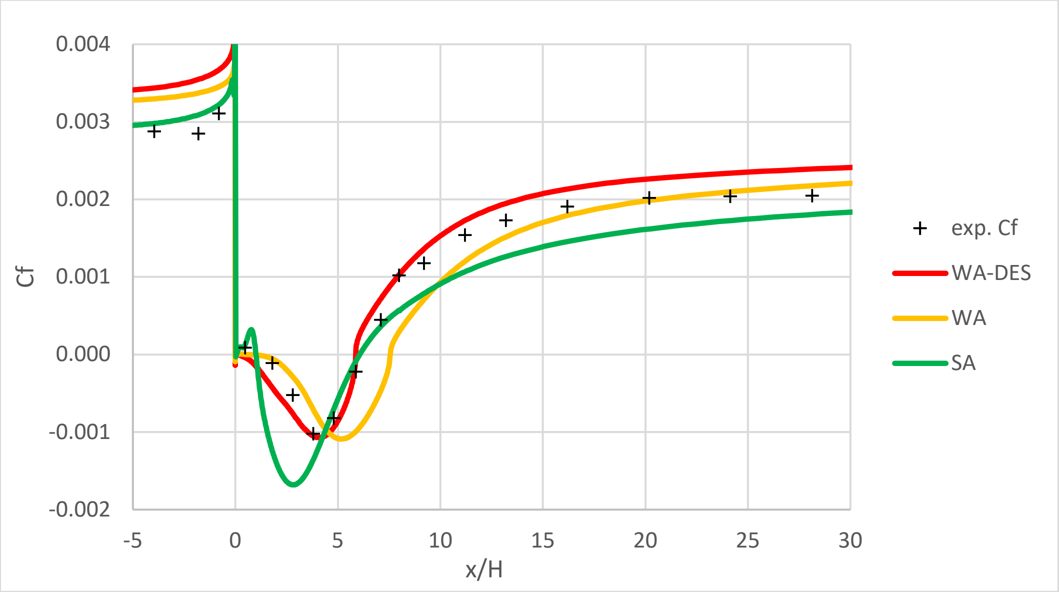

Figure 4.13: Comparison of Skin-Friction distribution on the surface of the backward facing step.

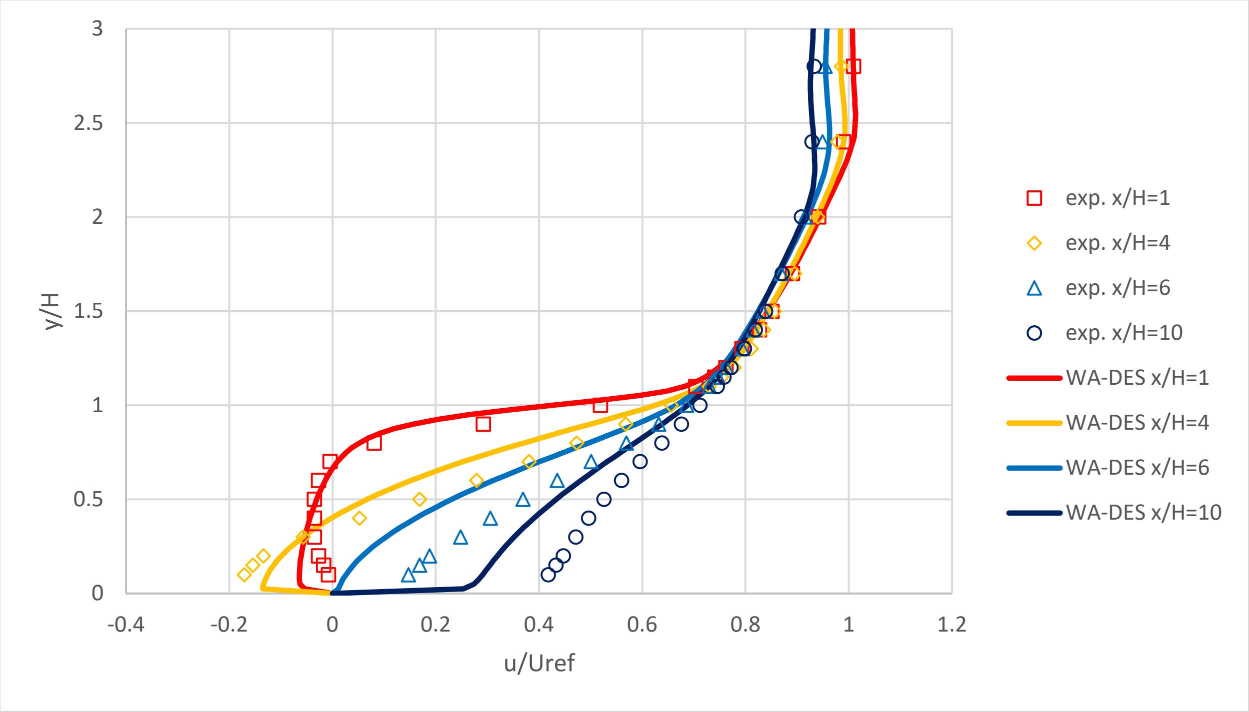

**Figure 4.14: Comparison of velocity profiles from WA-DES model and experimental values at various locations on the step.**

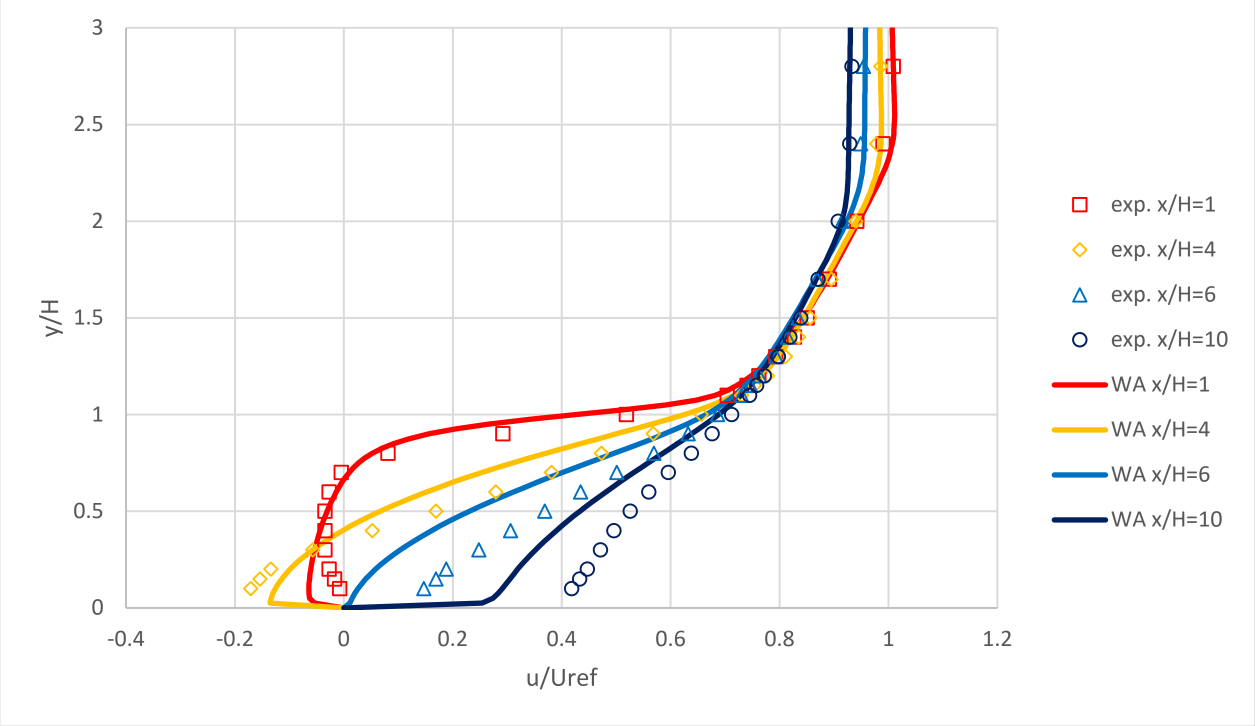

**Figure 4.15: Comparison of velocity profiles from WA model and experimental values at various locations on the step.**

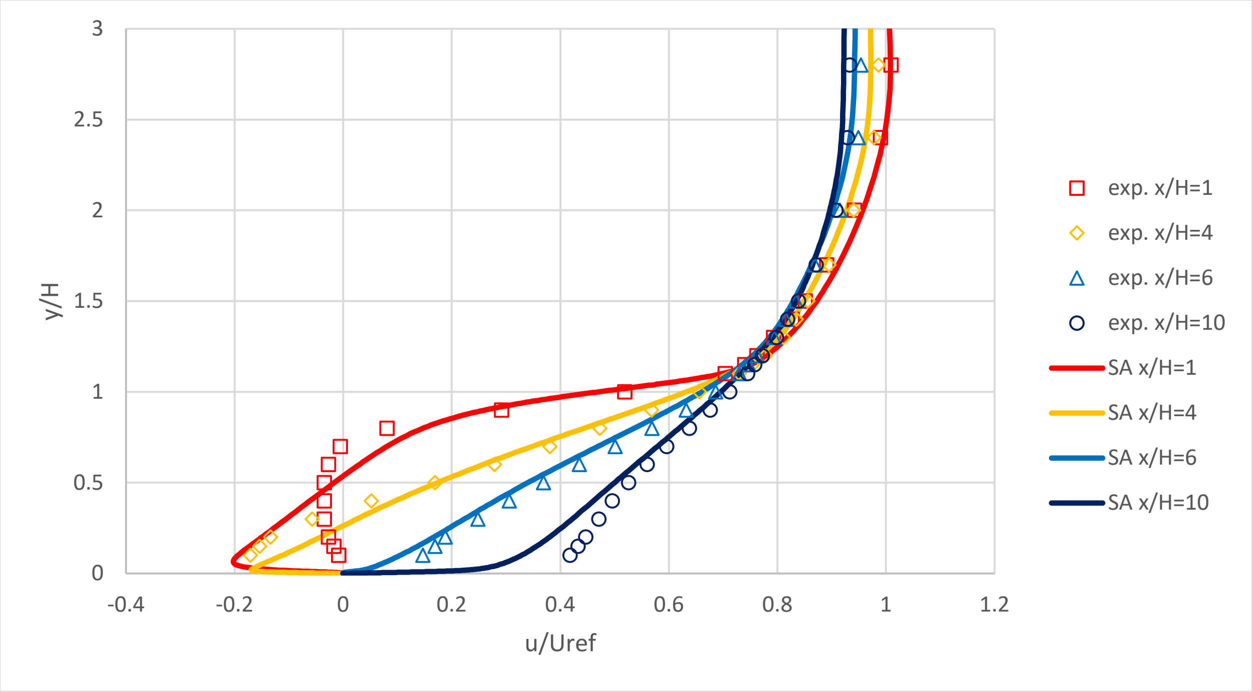

**Figure 4.16: Comparison of velocity profiles from SA model and experimental values at various locations on the step.**

### 4.5.5 Flow in an Asymmetric Plane Diffuser

Figure 4.17 shows the geometry of an asymmetric plane diffuser. Details of the geometry and boundary conditions are included in the NPARC Alliance CFD Verification and Validation Achieve (study #1) [23]. The inflow Mach number is 0.06 and the Reynolds number based on the inflow height H is $Re_H$ = 20,000 [24]. Adverse pressure gradient occurs on the inclined wall which contributes to flow separation. WA-DES results are compared to the RANS results with WA and SA models and the experimental data for both the pressure coefficient and the skin friction distribution on the bottom wall and the top wall of the diffuser. Figures 4.18 and 4.19 show the comparison of pressure distribution on the top and bottom wall of the diffuser respectively. Results of WA model best match the experimental data and the predictions of WA-DES model are slightly worse than that of the WA model. The computations from SA model have the poorest agreement with the experimental data among the three models. Figures 4.20 and 4.21 show the comparison of skin-friction distribution on the top and bottom wall of the diffuser respectively. As shown in Figure 4.20, WA-DES and WA models have good agreement with the experimental data for skin-friction on the top wall of the diffuser while SA model shows the poorest agreement. According to the experiment, the separation point occurs at x/H ≈ 6.6 and flow reattaches at x/H ≈ 27.5 on the top wall. In Figure 4.21, WA-DES model predicted separation region on the bottom wall begins at x/H = 7.31 and ends at x/H = 26.13. This result is closer to the experimental value compared to that obtained using the WA and SA models, which predict the separation region on the bottom wall from x/H = 7.03 to 30.97 and x/H = 4.26 to 31.29, respectively.

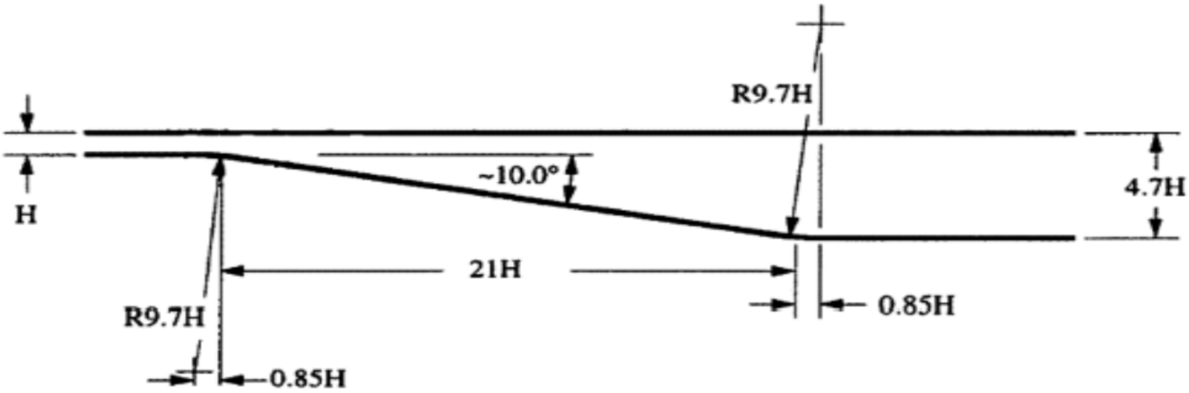

**Figure 4.17: Geometry of the asymmetric plane diffuser [23].**

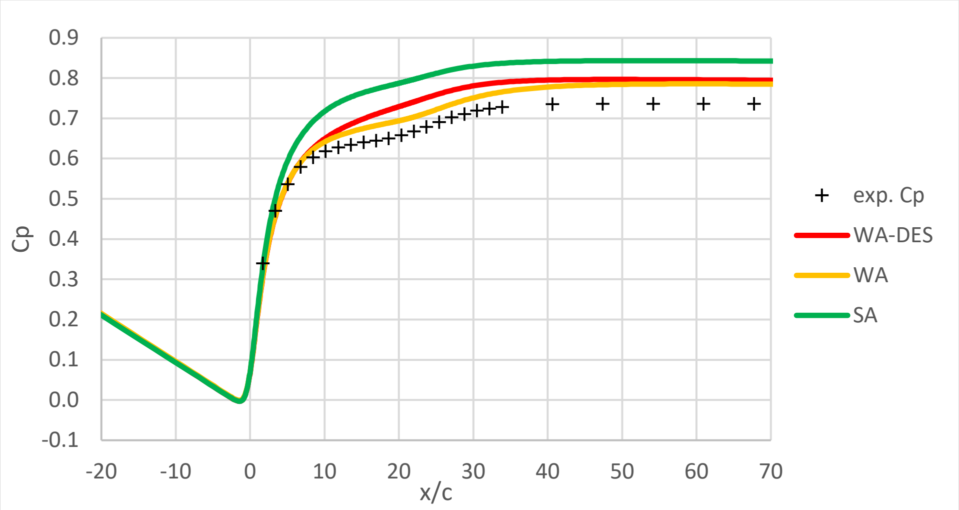

**Figure 4.18: Comparison of pressure distribution on the top wall of the diffuser.**

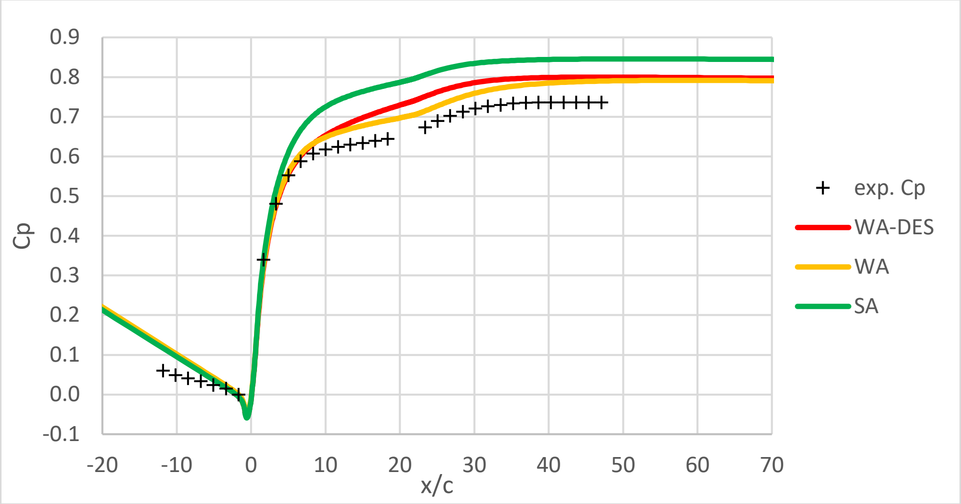

**Figure 4.19: Comparison of pressure distribution on the bottom wall of the diffuser.**

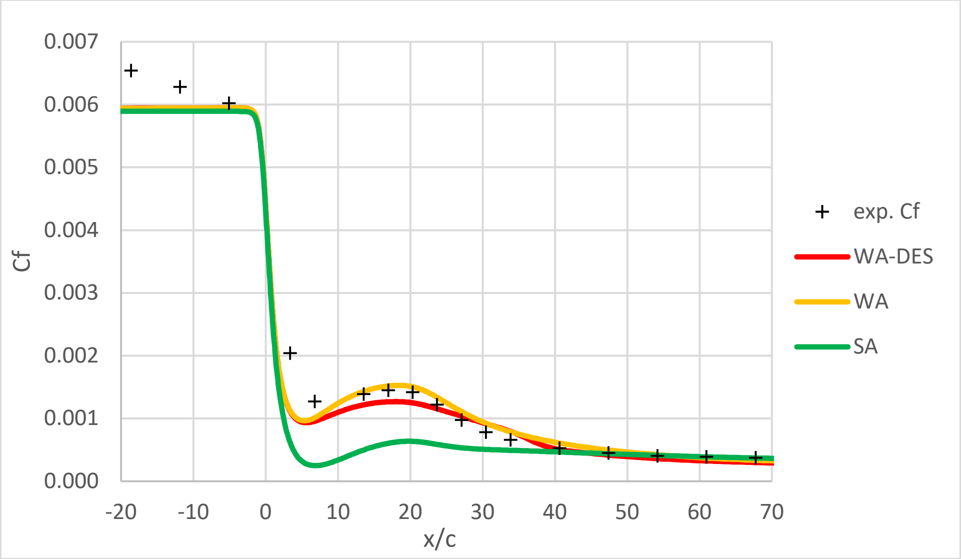

**Figure 4.20: Comparison of Skin-Friction distribution on the top wall of the diffuser.**

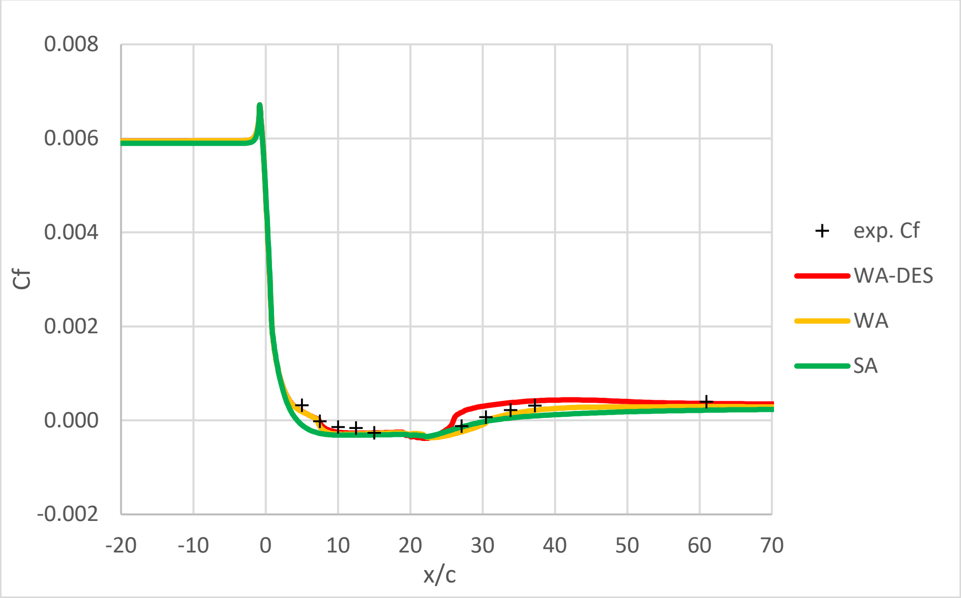

**Figure 4.21: Comparison of Skin-Friction distribution on the bottom wall of the diffuser.**

### 4.5.6 Flow past a NACA 4412 Airfoil

Subsonic flow past a NACA4412 airfoil is another benchmark test case used for evaluating the capability of the new WA-DES model. The freestream Mach number is 0.09 and the Reynolds number based on the Chord length is Re = 1.52 million. The angle of attack is 13.87 degrees. In the simulation, the outermost boundary of the computational domain is at a distance of 30 chords upstream from the leading edge of the airfoil. Surface pressure coefficient data and velocity profiles from the experiment of Coles et al. [25] are used to compare the simulations. No skin friction data is available, but the velocity profiles indicate that separation near the trailing edge occurs between x/c = 0.7 and 0.8. Computations using the WA-DES and WA model agree quite well with the experimental pressure coefficients, especially in the trailing edge region where separation occurs (x/c > 0.8) as shown in Figure 4.22 and Figure 4.23. However, SA model is unable to predict the separation region near the trailing edge accurately as shown in Figure 4.23. WA-DES, WA and SA model predict separation point at x/c = 0.76, 0.75 and 0.79, respectively.

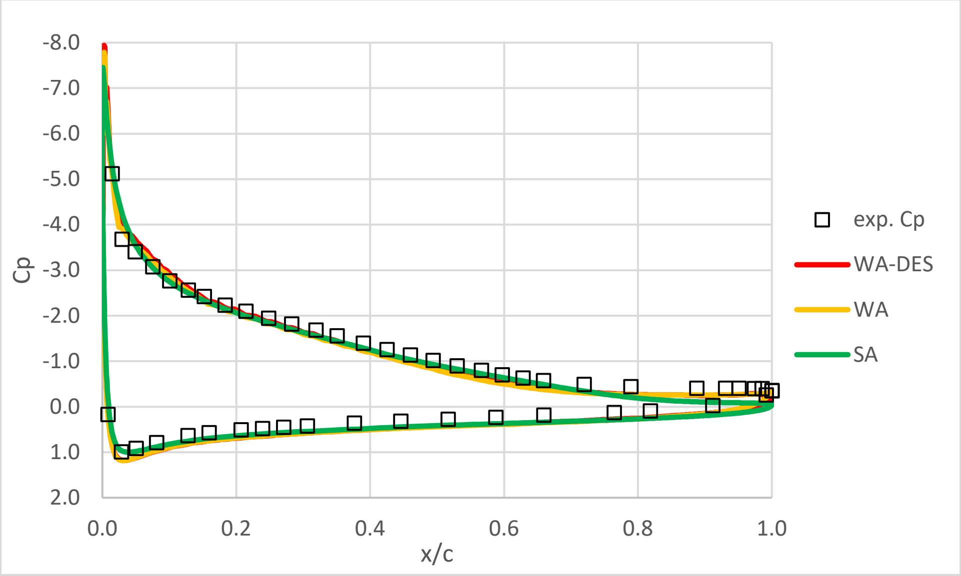

**Figure 4.22: Comparison of pressure coefficient distribution on the surface of the NACA 4412 airfoil.**

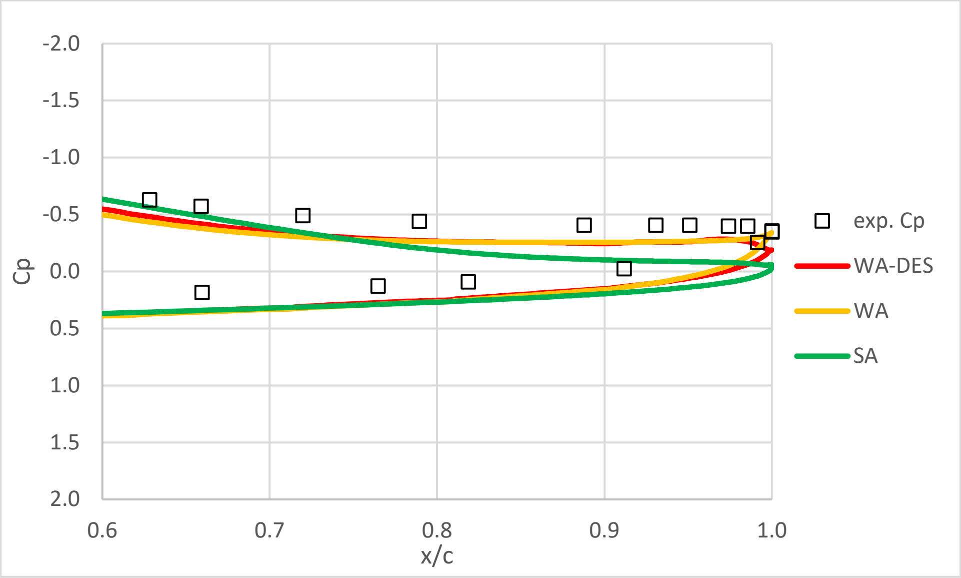

**Figure 4.23: Zoomed-in-View of pressure coefficient distribution in the trailing edge separation region of NACA 4412 airfoil.**

Figures 4.24, 4.25 and 4.26 compare the stream-wise velocity profiles at different locations on the airfoil surface. WA-DES computations show significant improvement in the results compared to those from the WA model and the SA model in the separation region (x/c > 0.8) when compared to the experimental data. In the region before the separation point, the result of WA-DES model is better than that of the WA model but is worse than that of the SA model. Both WA-DES and WA models under-predict the magnitude of stream-wise velocities and the

SA model over-predicts them. Figures 4.27, 4.28 and 4.29 compare the vertical velocity profiles. Results of WA-DES model are much closer to the experimental data compared to the WA model. In contrast to the predictions for the stream-wise velocity profiles, WA-DES model and WA model over-predict the magnitude of vertical velocities and the SA model under-predicts them.

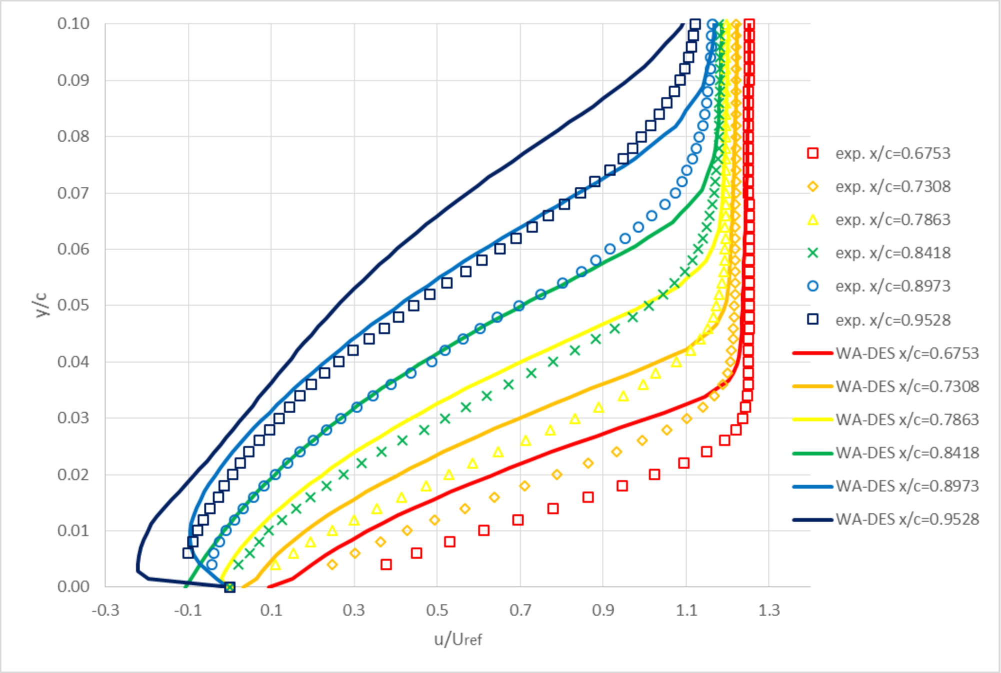

**Figure 4.24: Comparison of streamwise velocity profiles computed from WA-DES model and experimental values at various locations on the NACA 4412 airfoil.**

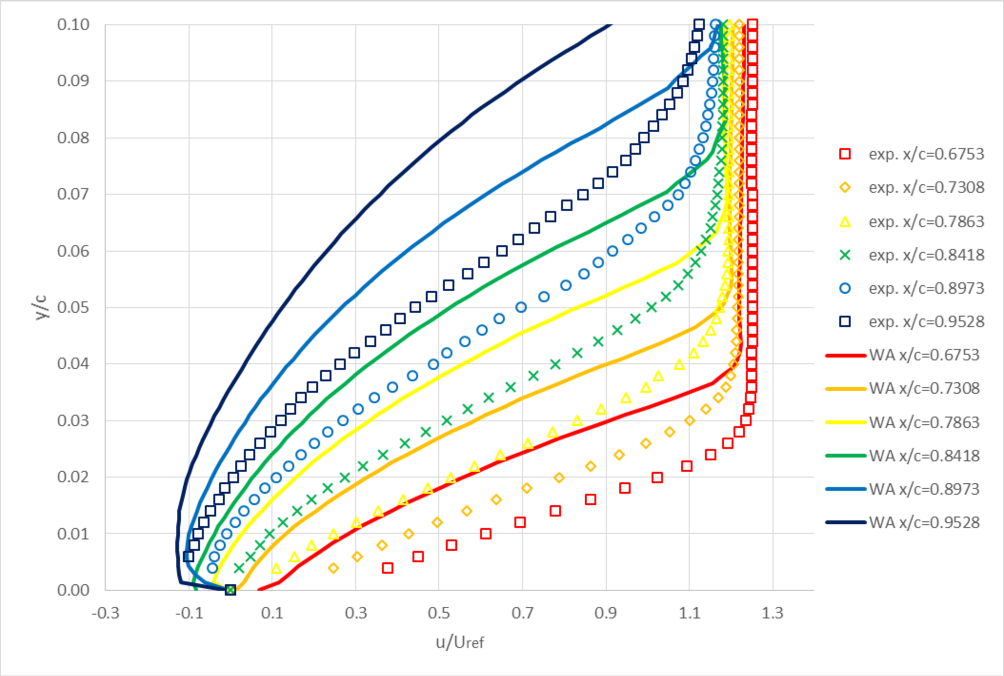

**Figure 4.25: Comparison of streamwise velocity profiles computed from WA model and experimental values at various locations on the NACA 4412 airfoil.**

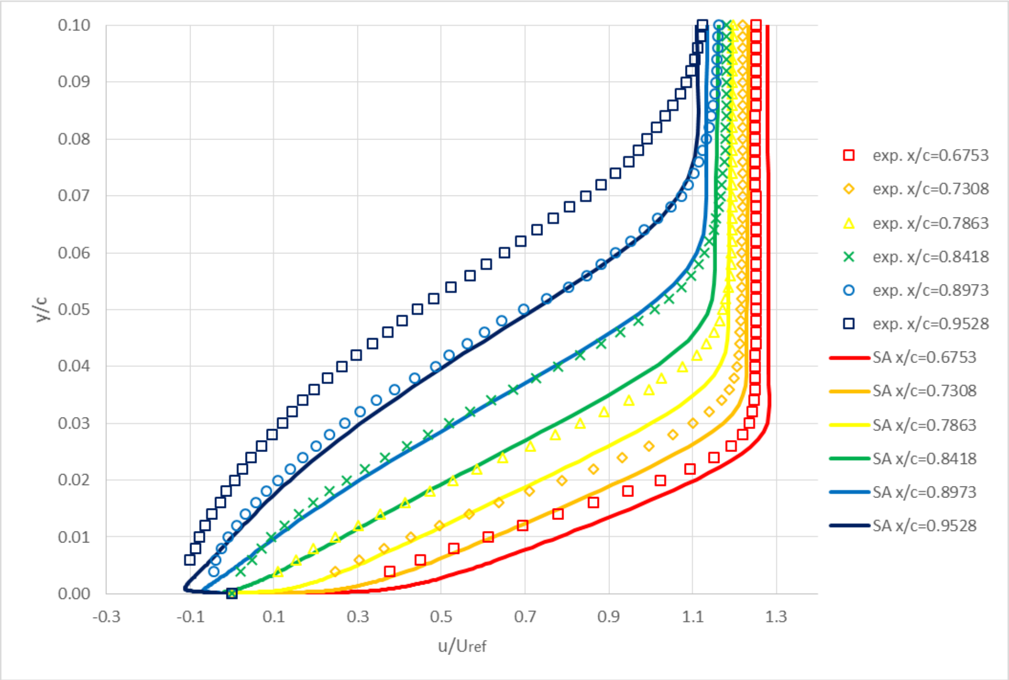

**Figure 4.26: Comparison of streamwise velocity profiles computed from SA model and experimental values at various locations on the NACA 4412 airfoil.**

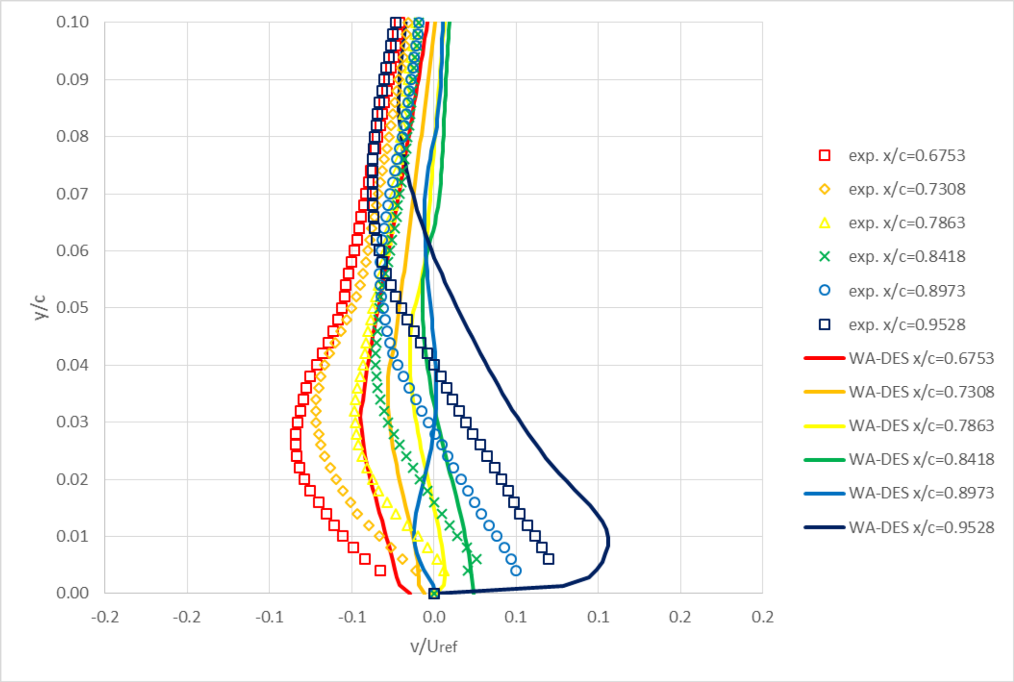

**Figure 4.27: Comparison of vertical velocity profiles computed from WA-DES model and experimental values at various locations on the NACA 4412 airfoil.**

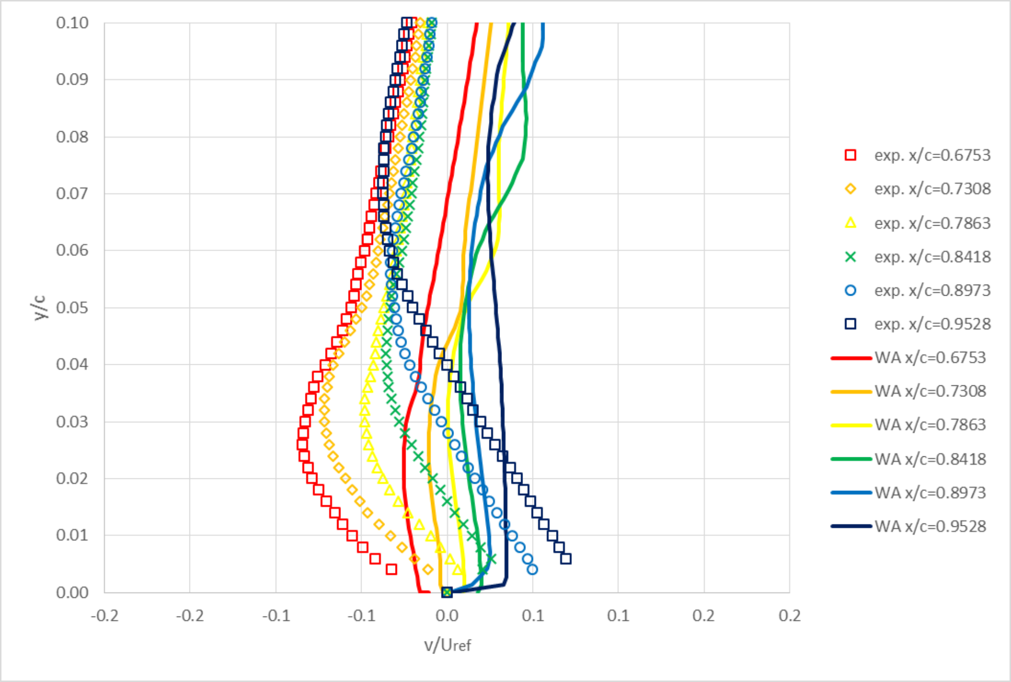

**Figure 4.28: Comparison of vertical velocity profiles computed from WA model and experimental values at various locations on the NACA 4412 airfoil.**

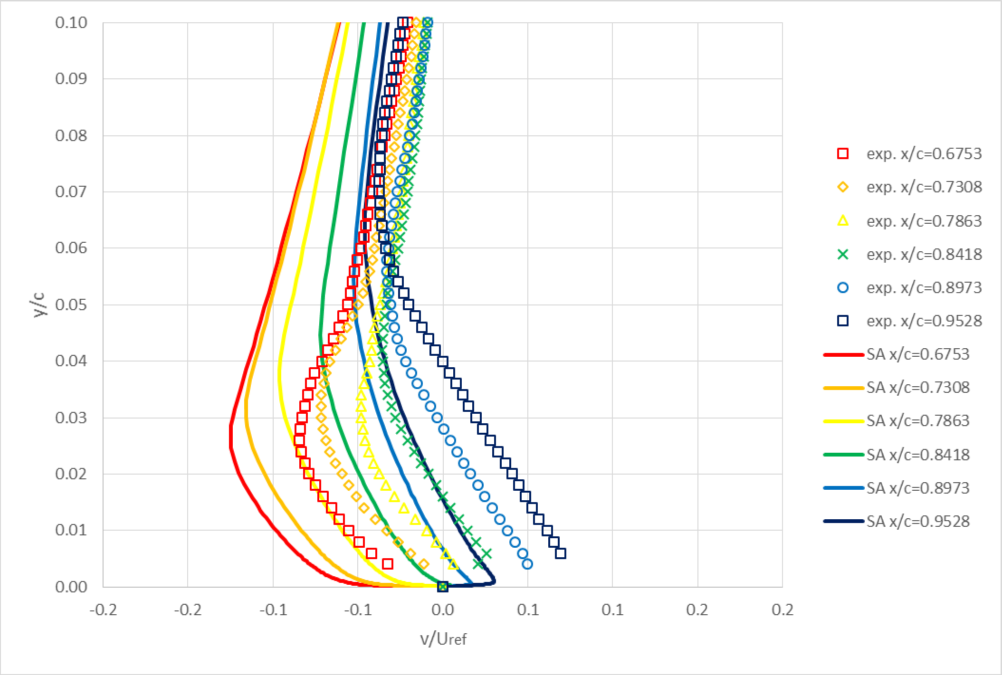

**Figure 4.29: Comparison of vertical velocity profiles computed from SA model and experimental values at various locations on the NACA 4412 airfoil.**

### 4.5.7 Flow over a Periodic Hill

Flow over a periodic hill is a popular benchmark test case for predicting the flow separation and reattachment. Details of this case are included in the European Research Community on Flow, Turbulence and Combustion (ERCOFTAC) database (case 81) [26]. The hill has a height h = 28mm, crests are separated by $L_x$ = 9h and channel height is $L_y$ = 3.035h. Except for the top and bottom patches which are set as no-slip wall, all the other four patches in the spanwise and streamwise directions are set as periodic boundary conditions. The Reynolds number is 10,595 based on the hill height h and the bulk velocity $U_b$ at the crest of the first hill. Flow is driven by a constant body force to ensure that the corresponding bulk velocity can yield the correct Reynolds number.

Simulation results from WA-DES model are compared to the LES results by Frohlich et al. [27] provided in the ERCOFTAC database and NASA Langley Research Center Turbulence Modeling Resource [20]. Figure 4.30 compares the skin friction distribution on the hill. None of the models match the LES solution very well. However, in Figures 4.31 and 4.32, the comparison of pressure coefficients on the hill and top wall show the improved results obtained by the WA-DES model. SA model shows the largest discrepancy in the computed pressure coefficient compared to the experimental data. Velocity profiles at ten different locations upon the hill are compared in Figure 4.33, in which the profiles computed by SA model show slightly better agreement with the experimental data than those computed by WA and WA-DES model.

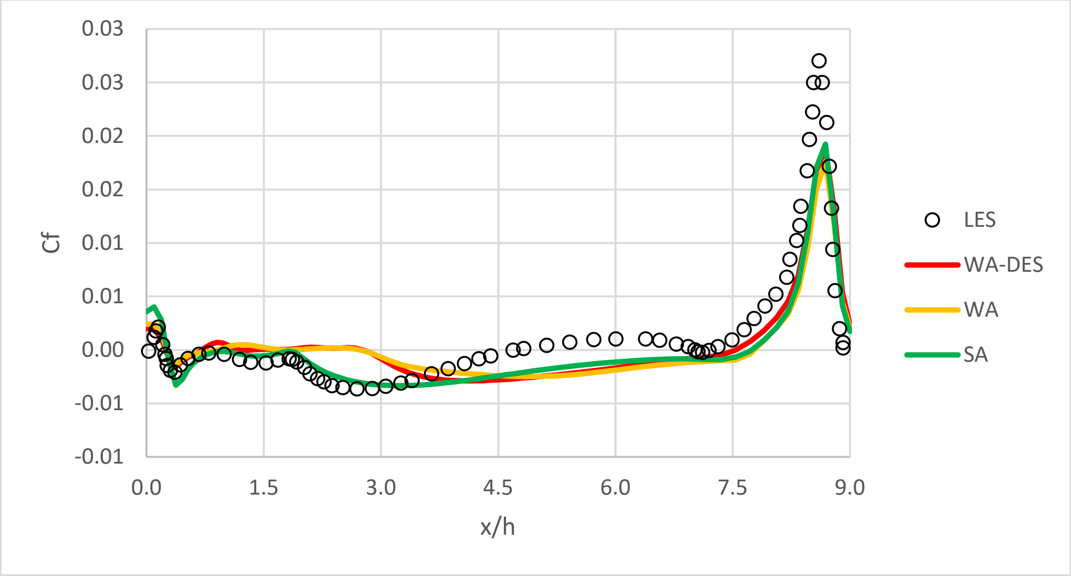

**Figure 4.30: Comparison of skin friction coefficient distribution on the period hill.**

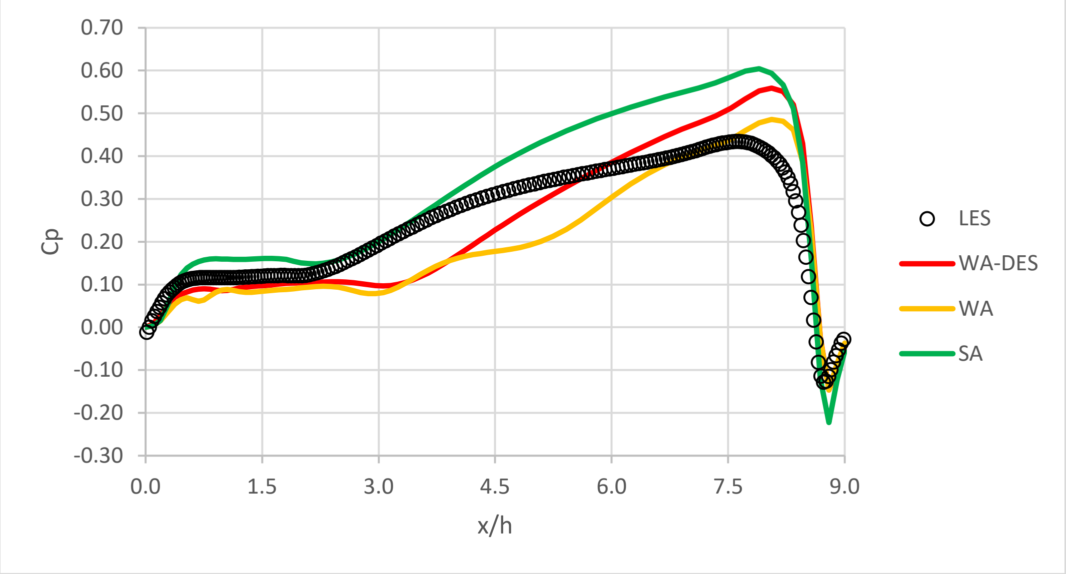

Figure 4.31: Comparison of pressure coefficient distribution on the period hill.

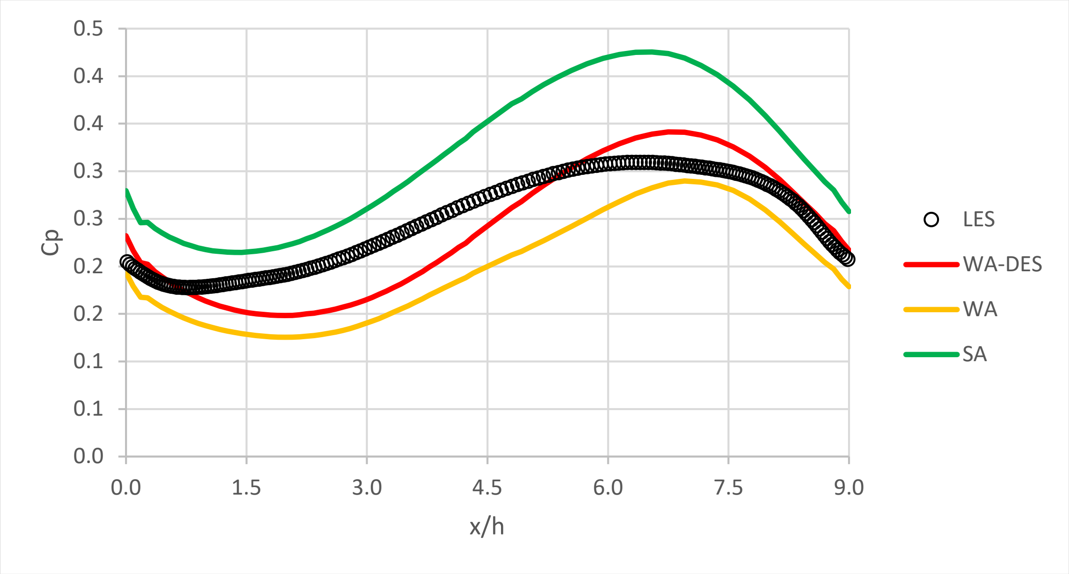

Figure 4.32: Comparison of pressure coefficient distribution on the top wall.

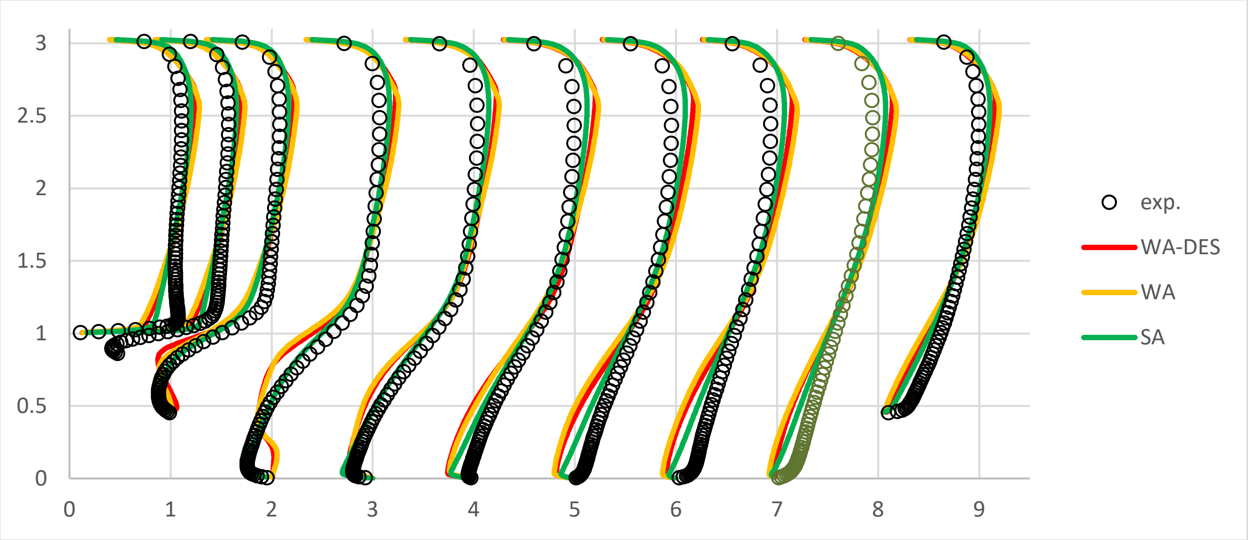

**Figure 4.33: Comparison of velocity profiles on periodic hill.**

### 4.5.8 Transonic Flow over an Axisymmetric Bump

The geometry of an axisymmetric bump is shown in Figure 4.34. The inflow Mach number is M = 0.875 and Reynolds number based on the bump chord length is $Re_c$ = 2.763 million. Experiment by Bachalo and Johnson [28] shows that flow separation occurs after the shock wave on the bump. Oil flow visualization indicates that the flow separation and reattachment occur at x/c = 0.7 and 1.1, respectively. The predicted pressure coefficients along the bump surface are compared to the experimental data in Figure 4.35. WA-DES model matches the experimental data more closely than the WA and SA model, in particular the WA-DES model improves the result of WA model in the near shock region as well as in the separation region. In a small region after the reattachment (x/c = 1.1 to 1.3), the result of WA model is better than the other two models. Predicted separation and reattachment points are compared to the experimental data in Table 4.1. WA model has a relatively large error in predicting the separation point, which is improved by the WA-DES model. WA-DES model also most accurately predicts the reattachment point, but the error is of the same magnitude as in the other two models.

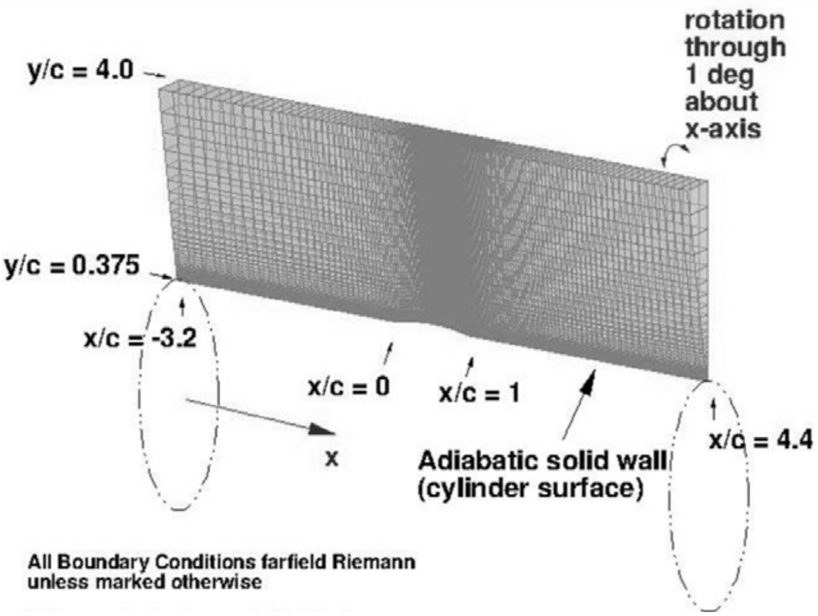

**Figure 4.34: Geometry and boundary conditions of transonic axisymmetric bump [20].**

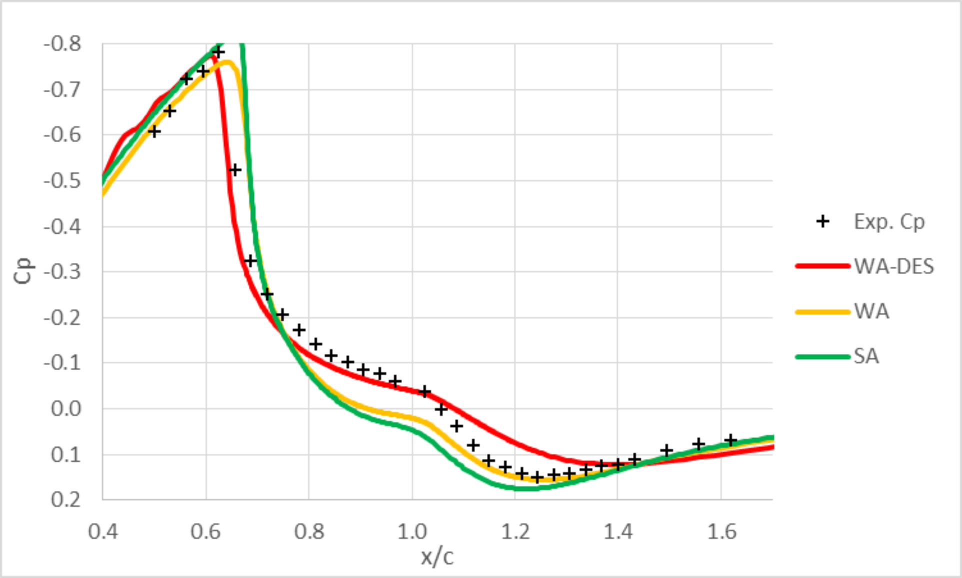

**Figure 4.35: Comparison of pressure coefficient distribution on the surface of the axisymmetric bump.**

**Table 4.1: Comparison of flow separation and reattachment points of the axisymmetric bump.**

| | Experiment | WA-DES | % Error | WA | % Error | SA | % Error |
|---|---|---|---|---|---|---|---|
| Separation | 0.7 | 0.696 | 0.57 | 0.817 | 16.71 | 0.688 | 1.71 |
| Reattachment | 1.1 | 1.166 | 6.00 | 1.123 | 2.09 | 1.16 | 5.46 |

The comparisons of velocity profiles between the experimental data and the computed results from the three turbulence models are presented in Figures 4.36, 4.37 and 4.38. Before the separation region (x/c = -0.25 and 0.688), WA-DES and WA model better predict the experimental velocities. In the separation region (x/c = 0.813 and 1), WA-DES model has the best match with experimental velocities. After the separation (x/c = 1.125 and 1.375), the velocity profiles from SA model are closest to the experimental values. However, both the WA-DES model and WA model are not significantly worse than SA model in this region.

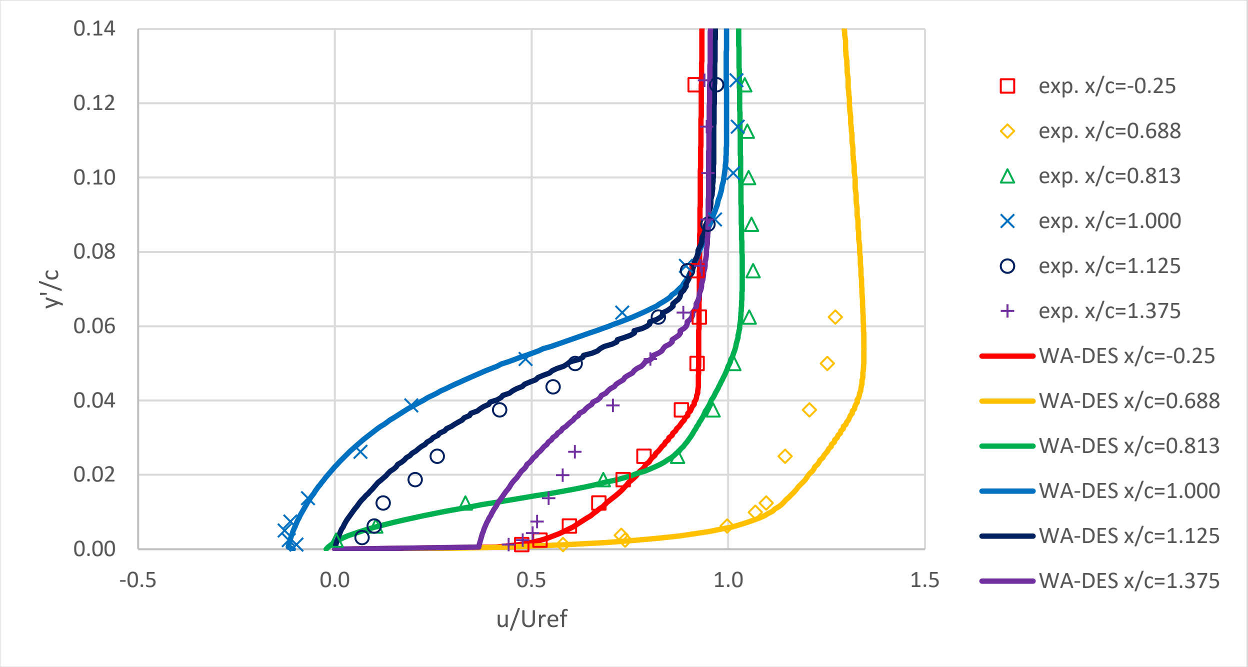

**Figure 4.36: Comparison of vertical velocity profiles computed from WA-DES model and experimental values at various locations on the axisymmetric bump.**

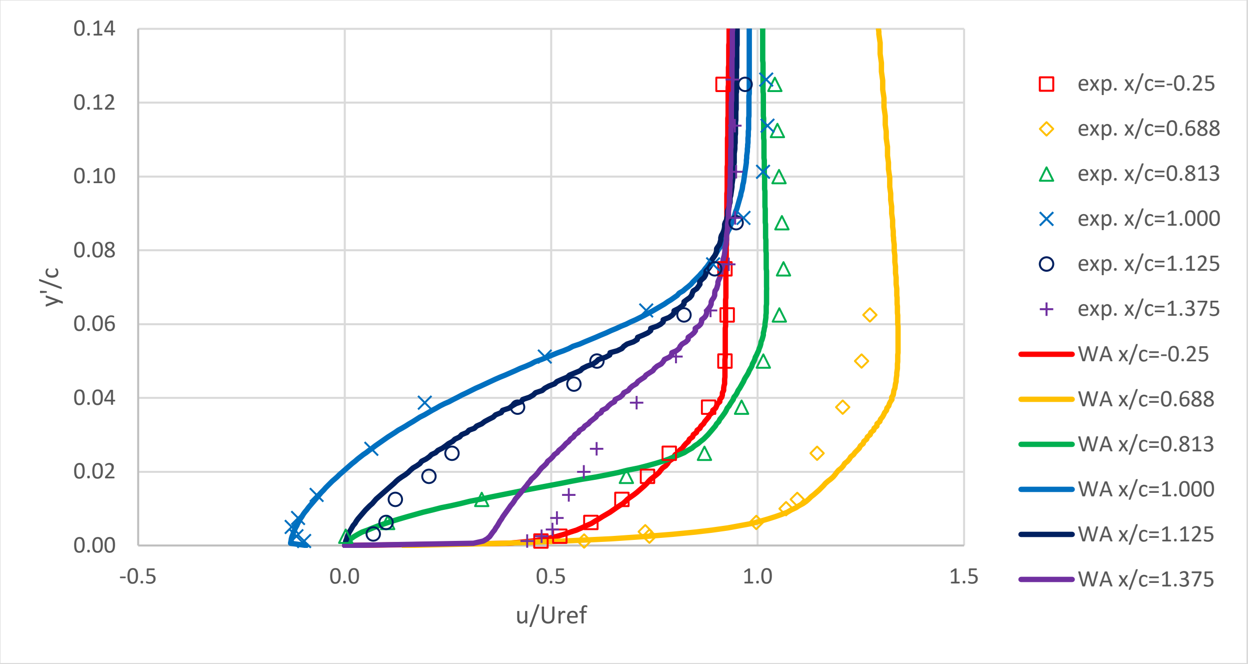

**Figure 4.37: Comparison of vertical velocity profiles computed from WA model and experimental values at various locations on the axisymmetric bump.**

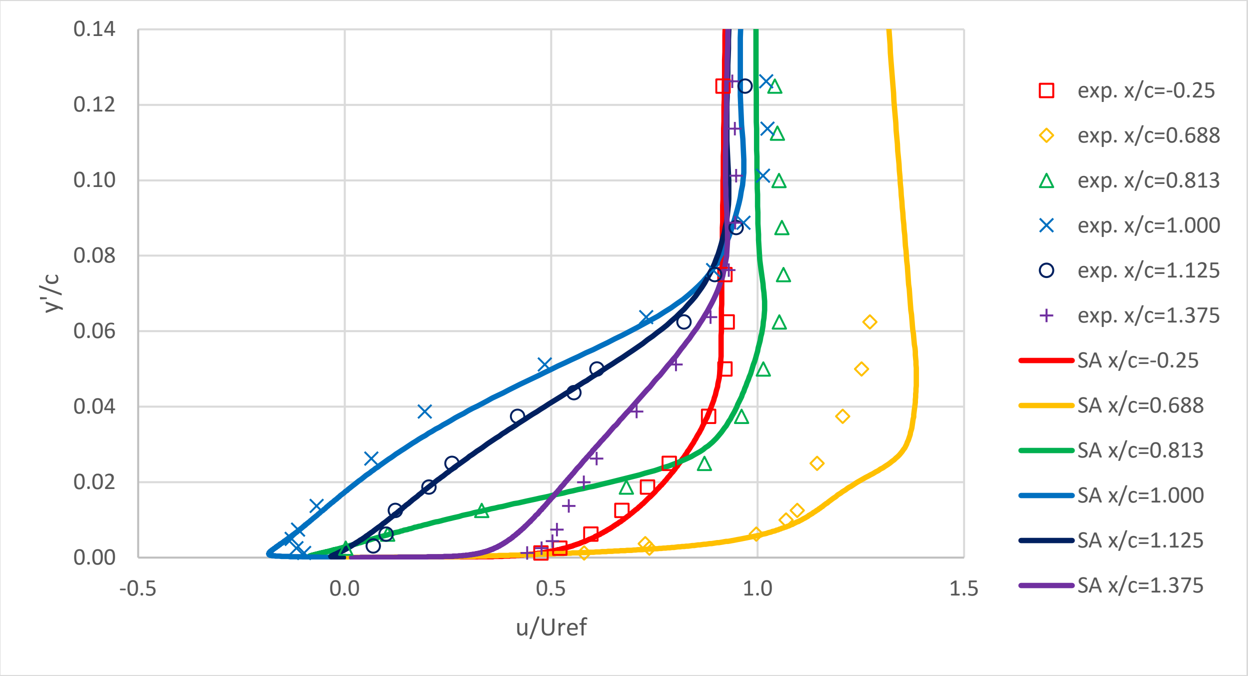

**Figure 4.38: Comparison of vertical velocity profiles computed from SA model and experimental values at various locations on the axisymmetric bump.**

### 4.5.9 Flow in 3D NASA Glenn S-Duct

The NASA S-duct was designed to study the complex three-dimensional flow phenomena such as the boundary layer separation and secondary flows [29, 30]. The duct's centerline was created by the union of two identical circular arcs, both of the same radius R = 1.02m and located in the same plane as shown in Figure 4.39. The area ratio of S-duct (ratio between the outlet and inlet sections) is equal to 1.52. The inlet diameter, $D_1$, is 0.2042m and the outlet diameter, $D_2$, is 0.2514m. The offset of the intake resulting from the centerline curvature is 1.34 times the inlet diameter.

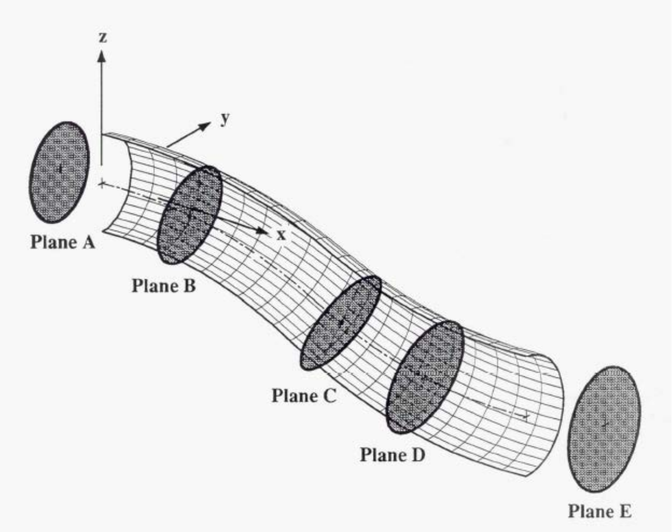

**Figure 4.39: S-Duct geometry with planes of interest [29].**

Inflow conditions are matched using the NASA Glenn's experimental conditions [29]. Figure 4.39 shows the NASA Glenn's S-Duct with planes of interests in analyzing the flow field. In order to compare the experimental and computational results, the non-dimensional ratio of centerline curve length to inlet diameter ($s/D_1$) is used. The 'reference inlet' flow conditions in the experiment are the centerline Mach number M = 0.6 and Reynolds number Re = 2.6 million at the position $s/D_1 = -0.5$ (Plane A in Figure 4.39). At the reference inlet plane the flow is considered turbulent and fully developed since it has not reached the curved portion of the duct yet. The outlet of the duct is at $s/D_1 = 5.23$. The Aerodynamic Interface Plane (AIP), where the turbine face is located, is at $s/D_1 = 5.73$ (Plane E in Figure 4.39).

Computational results are compared with the experimental data for static pressure coefficients, Cp. Figure 4.40 shows the experimental static pressure coefficient along the non-dimensional duct centerline (s/D1) for three different angular sections of the duct, φ = 10º, 90º, and 170º. Results from all the three models are shown in Figures 4.41, 4.42 and 4.43. Compared to the SA model, the WA and WA-DES models show better agreement with the experiment at all the three angular locations. In the separation region ($s/D_1$=2.01 to 4.12), especially at the beginning of separation, the pressure predicted by the WA-DES model best fits the experimental result. Table 4.2 compares the prediction of flow separation from the three models. All the models precisely predict the separation point, but they underestimate the length of the separation region. The closest prediction of reattachment point is by WA model which still has a 10% error. Figures 4.43 and 4.44 compare the total pressure coefficient contours and Mach number contours at AIP, respectively. Both WA and WA-DES model predict the total pressure coefficient 0.9 and Mach 0.4 line reasonably well.

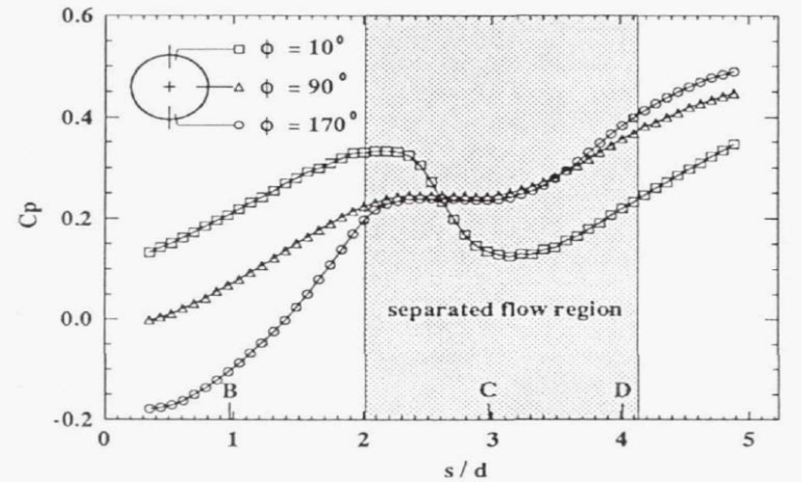

**Figure 4.40: Non-dimensional static pressure coefficient along the S- duct in NASA Glenn's experiment [29].**

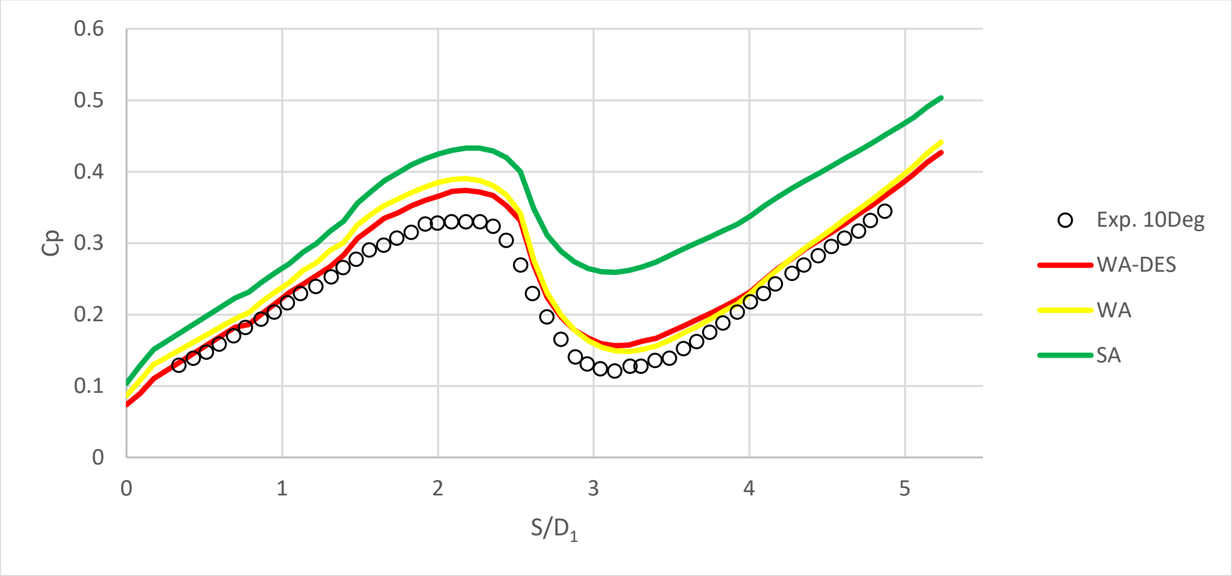

Figure 4.41: Comparison of experimental and computed pressure coefficients at 10º angular position.

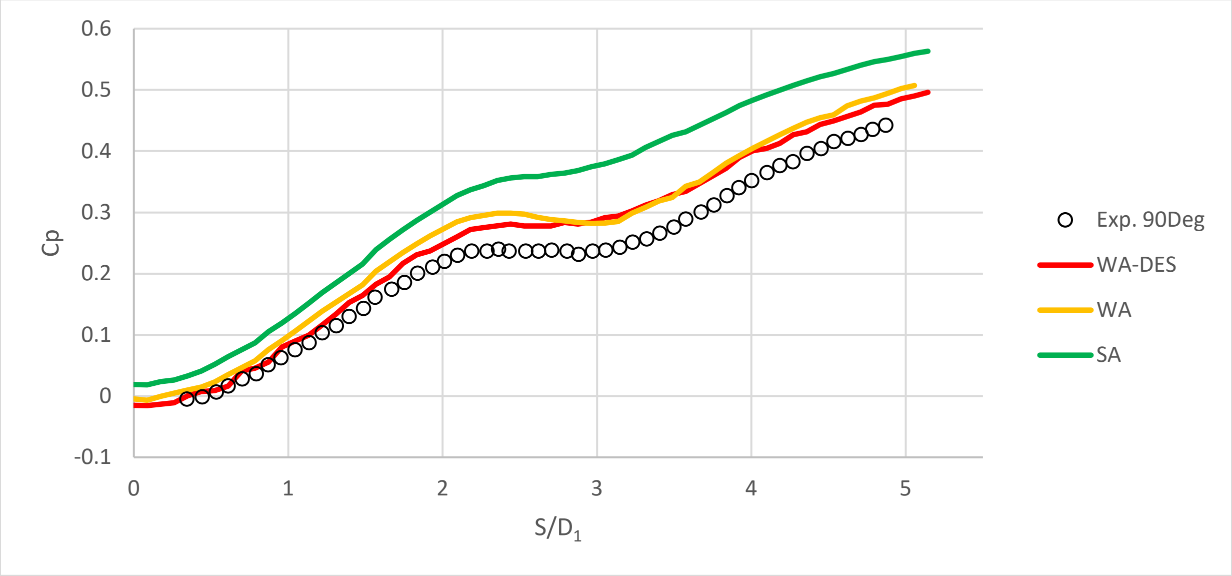

Figure 4.42: Comparison of experimental and computed pressure coefficients at 90º angular position.

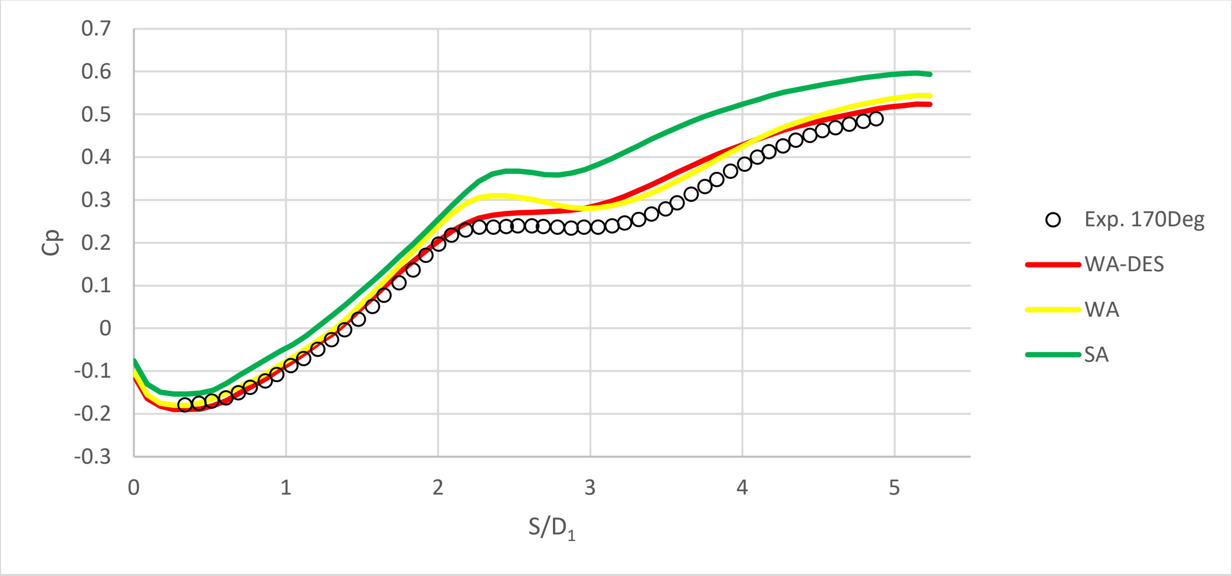

**Figure 4.43: Comparison of experimental and computed pressure coefficients at 170º angular position.**

**Table 4.2: Comparison of flow separation and reattachment points for the S-Duct.**

| | Experiment | WA-DES | % Error | WA | % Error | SA | % Error |
|---|---|---|---|---|---|---|---|
| Separation | 2.01 | 2.00 | 0.50 | 1.97 | 1.99 | 1.97 | 1.99 |
| Reattachment | 4.12 | 3.53 | 14.32 | 3.70 | 10.19 | 3.58 | 13.11 |

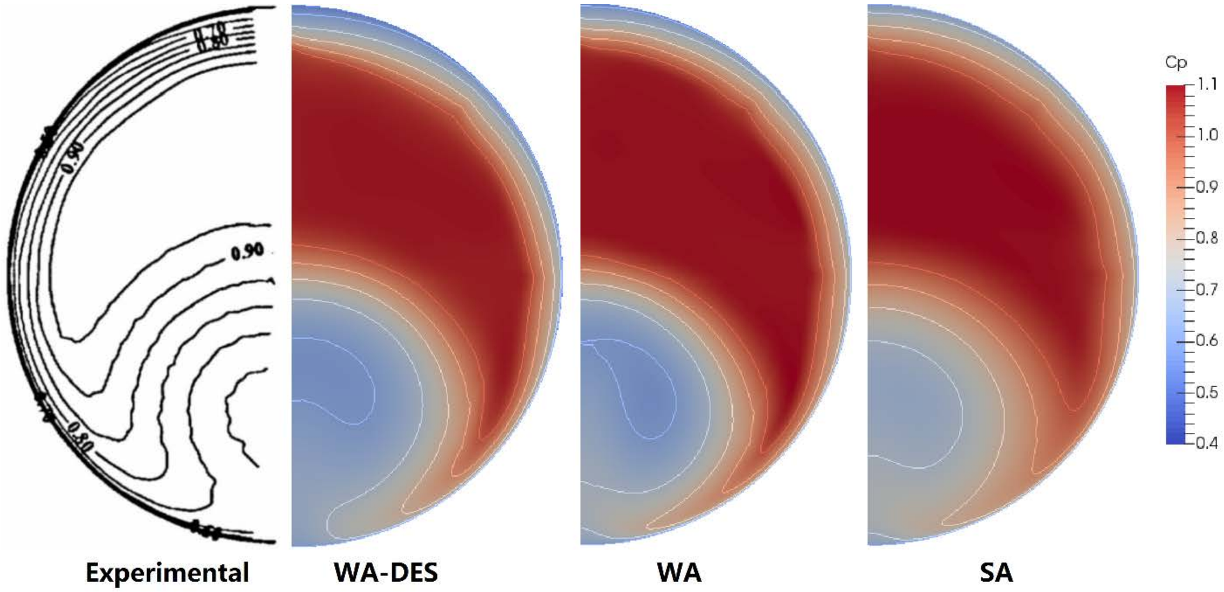

**Experimental** **WA-DES** **WA** **SA**

**Figure 4.44: Comparison of total pressure coefficient contours at AIP.**

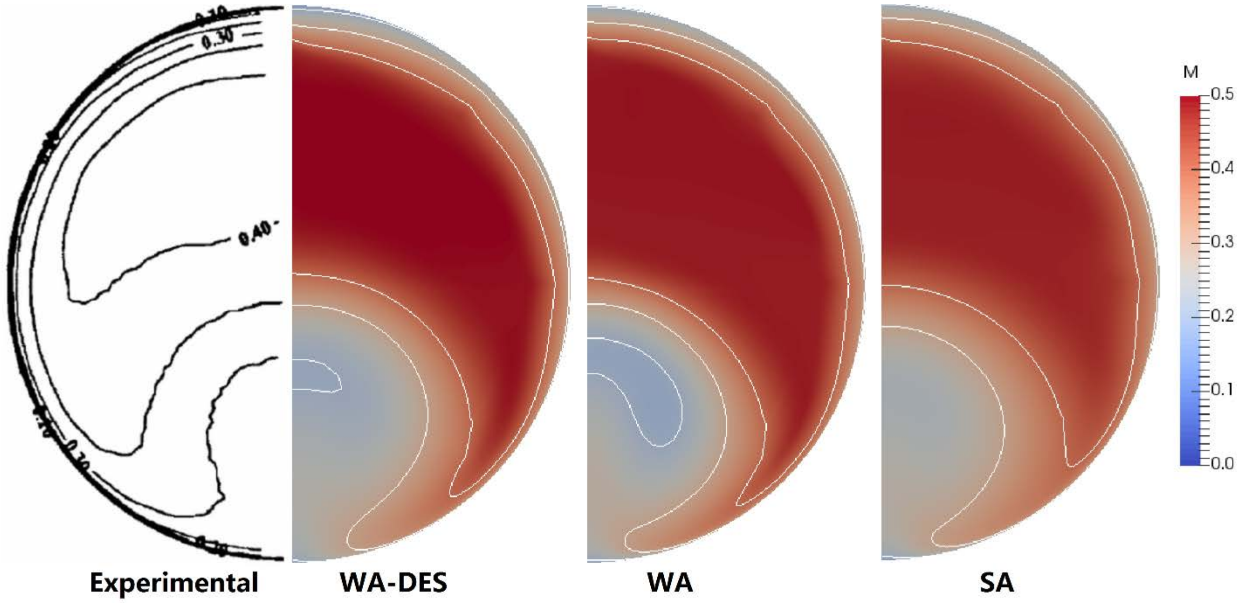

Experimental WA-DES WA SA

Figure 4.45: Comparison of Mach Number contours at AIP.

# Chapter 5: The WA-IDDES Model

## 5.1 Introduction

### 5.1.1 Delayed Detached-Eddy Simulation

DES is a promising method developed in past two decades for computing turbulent flows efficiently with acceptable accuracy for many flows characterized by large mixing regions and massive separation. It takes advantages of the good properties of LES and RANS while overcoming their weaknesses. However, due to the introduction of grid spacing and length scale switch, DES model can be highly grid-sensitive. By making use of this feature, CFD researchers can control the LES/RANS regions by changing the local grid size. However, it also causes numerical problems. One of the biggest issues arises due to the grid-sensitivity known as the modeled-stress depletion (MSD). MSD happens in the 'ambiguous' grid region in the boundary layer. It implies that the DES length scale switches to the LES length scale, but the grid is not fine enough to support the LES calculation to resolve the velocity fluctuation inside the boundary layer. Thus, the eddy viscosity is artificially reduced and may lead to grid-induced separation (GIS). It often happens when the grid is gradually refined from a coarse region. Figure 5.1 is an example of GIS happening in an airfoil simulation [31]. The RANS model accurately predicted the separation point but the separation predicted by DES occurs much earlier.

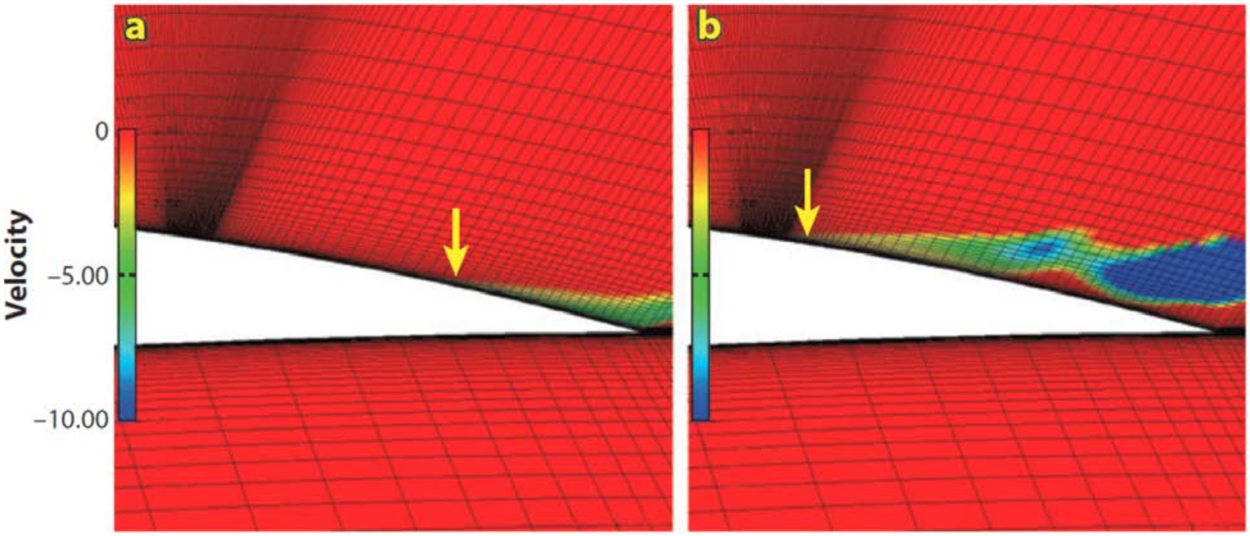

**Figure 5.1: Grid Induced Separation by SA-DES model on an airfoil [31].**

Menter et al. proposed a solution to the SST-DES model called shielding to prevent MSD and GIS [31]. By making use of the $F_2$ function in SST $k$-$\omega$ model, DES length scale is enforced to switch to RANS mode near the wall. Spalart et al. introduced DDES idea in 2006 which is applicable to most turbulence models [32]. Both shielding techniques successfully prevent the GIS and MSD.

### 5.1.2 Improved Delayed Detached-Eddy Simulation

Based on DDES approach, IDDES is another improved refinement to DES modeling which combines the RANS model with a version of LES known as the wall-modeled LES (WMLES). In DES and DDES, excessive reduction of Reynolds stress may occur near the RANS and LES interface, which may result in the problem called the Log-Layer Mismatch (LLM). According to the original development of SA-IDDES, this new model responds differently depending on whether the simulation does or does not have inflow turbulence content, and addresses the LLM problem in DES and DDES [33]. IDDES has also been developed for the SST $k$-$\omega$ model, it shows the potential of simplifications by setting the elevating function to zero [34].

## 5.2 Derivation of WA-DDES/IDDES Model

### 5.2.1 Derivation of WA-DDES Model

In DDES models, the general shielding function is defined as in Eq. (25) below.

$$f_d = 1 - tanh([C_{d1} r_d]^{C_{d2}})$$
$$r_d = \frac{\nu_t + \nu}{\sqrt{u_{ij} u_{ij}} \kappa^2 d^2} \tag{25}$$

This shielding function is used to interpolate the length scales as given in Eqs. (21, 22). Inside the boundary layer, DES always uses RANS length scale regardless of the local grid spacing; and it changes to the original DES definition outside the boundary layer.

$$l_{DDES} = l_{RANS} - f_d max(l_{RANS} - l_{LES}, 0) \tag{26}$$

There are two constants $C_{d1}$ and $C_{d2}$ to specify in the general DDES shielding function. They can be calibrated by the skin friction coefficient on a flat plate [32]. Gritskevich et al. calibrated the constants for SST-DES on a flat plate mesh with excessive refinement [34]. The grid spacing equals the boundary layer thickness δ at $Re_x$ = 1e7 and reduces to 0.1 δ at Rex = 5e6. Figure 5.2 shows the result of SST-DDES calibration. The best $C_{d1}$ value for SST-DDES is 20 compares to 8 in SA-DDES model. The $F_1$ function originally implemented in SST *k-ω* model to switch between *k-ω* and *k-ε* is also tested as the shielding function. But its predicted shear stress is much lower than the experimental value after the refinement point. Even though the result is better than the original SST-DES model, shielding is not sufficiently provided compared to the general shielding function.

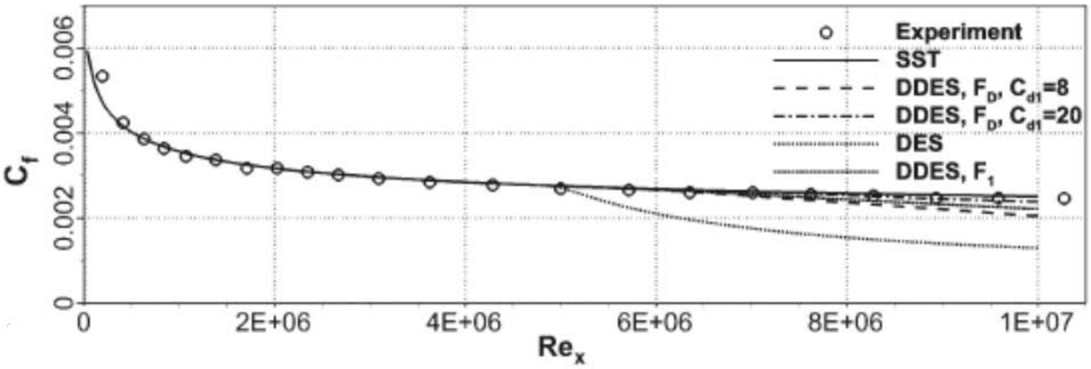

**Figure 5.2: Calibration of the SST-DDES constant on a flat plate with excessive refinement [34].**

Based on the above observation, in WA-DES model is implemented with the general shielding function in Eq. (25) via $F_{DDES}$ function to develop the corresponding WA-DDES model as shown in Eq. (27) below.

$$\frac{\partial R}{\partial t}+\frac{\partial u_j R}{\partial x_j}=\frac{\partial}{\partial x_j}\left[(\sigma_R R+\nu)\frac{\partial R}{\partial x_j}\right]+C_1 RS+f_1 C_{2k\omega}\frac{R}{F_{DDES}^2 S}\frac{\partial R}{\partial x_j}\frac{\partial S}{\partial x_j} \\ -(1-f_1)C_{2k\varepsilon}\frac{R^2}{F_{DDES}^2}\left(\frac{\frac{\partial S}{\partial x_j}\frac{\partial S}{\partial x_j}}{S^2}\right) \tag{27}$$

In Eq. (27) the $F_{DDES}$ is the DDES characteristic length scale ratio.

$$F_{DDES}=\max\left(\frac{l_{RANS}}{l_{DDES}},1\right) \tag{28}$$

The new constants are calibrated by the same flat plate case mentioned above. The general principle in this calibration is to keep the value of constant $C_{d1}$, which is proportional to the shielding thickness, as low as possible to guard the original LES region, but still big enough to prevent the GIS. Finally, the $C_{d1}$ and $C_{d2}$ constants are set to 4 and 3, respectively.

$$C_{d1}=4, \quad C_{d2}=3 \tag{29}$$

The calibration is shown in the Figure 5.3 below.

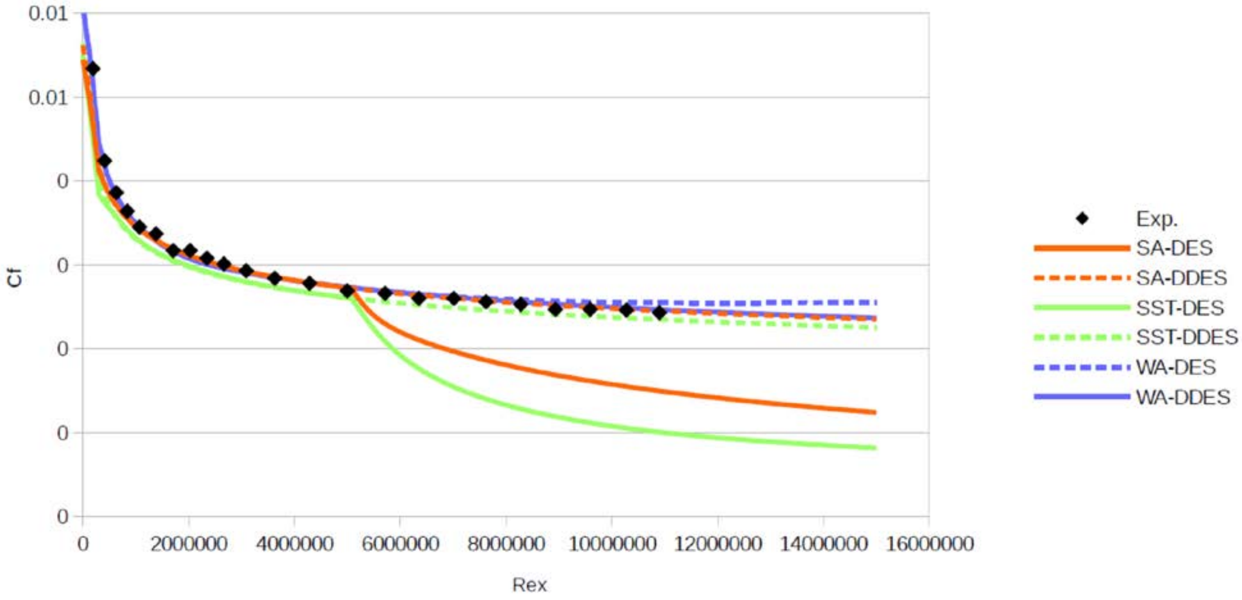

**Figure 5.3: Calibration of the WA-DDES constant on a flat plate with excessive refinement.**

### 5.2.2 Derivation of WA-IDDES Model

The WA-IDDES model redefines the characteristic length scale ratio $F_{DDES}$ in WA-DDES model as $F_{IDDES}$. The IDDES equations and constants are the same as in the SA-IDDES and SST-IDDES models [14, 17], except that the DDES constant $C_{d1}$ is set to be 4 based on the calibration of WA-DDES model mentioned above.

$$\frac{\partial R}{\partial t}+\frac{\partial u_j R}{\partial x_j}=\frac{\partial}{\partial x_j}\left[(\sigma_R R+\nu)\frac{\partial R}{\partial x_j}\right]+C_1 RS+f_1 C_{2k\omega}\frac{R}{F_{IDDES}^2 S}\frac{\partial R}{\partial x_j}\frac{\partial S}{\partial x_j} -(1-f_1)C_{2k\varepsilon}\frac{R^2}{F_{IDDES}^2}\left(\frac{\frac{\partial S}{\partial x_j}\frac{\partial S}{\partial x_j}}{S^2}\right) \tag{30}$$

The $F_{IDDES}$ is define by the equations and constants below:

$$F_{IDDES}=\max\left(\frac{l_{RANS}}{l_{HYB}},1\right) \tag{31}$$

$$l_{HYB}=\tilde{f}_d(1+f_e)l_{RANS}+\left(1-\tilde{f}_d\right)l_{LES} \tag{32}$$

$$\begin{gathered} l_{LES}=C_{DES}\Delta_{IDDES} \\ \Delta_{IDDES}= min\{max[C_w d, C_w\Delta_{DES},\Delta_{WN}],\Delta_{DES}\} \end{gathered} \tag{33}$$

$\Delta_{WN}$ is wall normal grid spacing

$$\begin{gathered} \tilde{f}_d = max(1 - f_{dt}, f_B) \\ f_{dt} = 1 - tanh[(C_{d1} r_{dt})^3] \\ f_B = \min\left(2e^{-9\alpha^2}, 1\right) \\ \alpha = 0.25 - d/max\left(\Delta_x, \Delta_y, \Delta_z\right) \end{gathered} \tag{34}$$

$$\begin{gathered} f_e = \max(f_{e1} - 1, 0) f_{e2} \\ f_{e1} = \begin{cases} 2e^{-11.09\alpha^2} & if\ \alpha \geq 0 \\ 2e^{-9.0\alpha^2} & if\ \alpha < 0 \end{cases} \\ f_{e2} = 1.0 - max(f_t, f_l) \\ \begin{cases} f_t = tanh[({c_t}^2 r_{dt})^3] \\ f_l = tanh[({c_l}^2 r_{dl})^{10}] \end{cases} \end{gathered} \tag{35}$$

$$\begin{gathered} \begin{cases} r_{dt} = \dfrac{\nu_t}{\kappa^2 d^2 max\left\{\left[\sum_{i,j}\left(\dfrac{\partial u_i}{\partial x_j}\right)^2\right]^{1/2}, 10^{-10}\right\}} \\ r_{dl} = \dfrac{\nu}{\kappa^2 d^2 max\left\{\left[\sum_{i,j}\left(\dfrac{\partial u_i}{\partial x_j}\right)^2\right]^{1/2}, 10^{-10}\right\}} \end{cases} \\ r_{dt} = tanh[({c_t}^2 r_{dt})^3] \\ f_t = tanh[({c_t}^2 r_{dt})^3] \end{gathered} \tag{36}$$

$$\begin{gathered} C_w = 0.15\ C_{d1} = 4.0 \\ c_t = 1.63 \quad c_l = 3.55 \end{gathered} \tag{37}$$

## 5.3 Discussion of WA-DDES Model

From the calibration result in Figure 5.3, one can see that the GIS of WA-DES model is much smaller than the other two models. Figure 5.4 shows the comparison of RANS and LES length scales of different DES models inside the flat plate boundary layer in the fine grid region ($Re_x$ = 1e7). From this figure, one can note that the LES contents of the three models are all activated ($l_{LES} < l_{RANS}$). However, in the WA model, the LES length scale is much closer to the RANS one ($l_{LES} \approx l_{RANS}$) and thus has less influence on the turbulent equation(s).

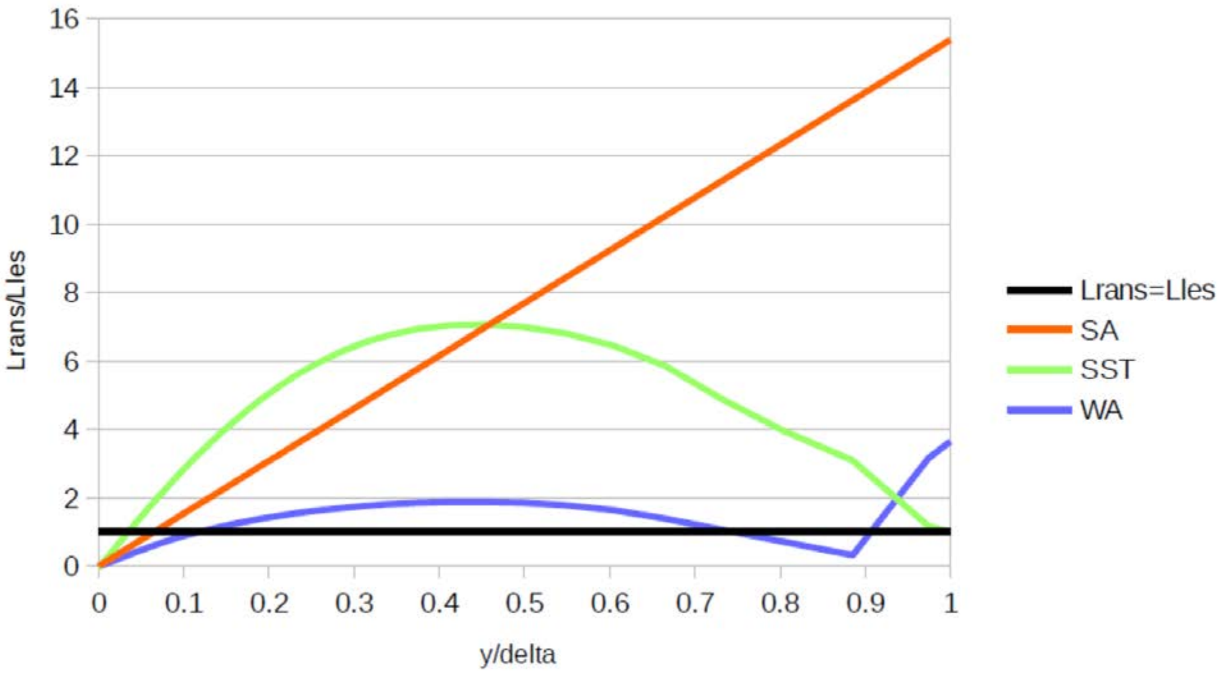

**Figure 5.4: Comparison of RANS and LES length scales of different DES models inside the flat plate boundary layer.**

Considering that the general shielding function in Eq. (25) can not perfectly predict the boundary layer, especially for the shallow separation regions, pure DDES approach may not be very beneficial for the WA-DES model. For example, the RANS region is likely to be active in separation region, which is more desirable for the LES content [35]. Due to the above reasons, IDDES is chosen as a more advanced and correct approach for refinement of the WA-DES model.

## 5.4 Validation Cases

### 5.4.1 Flow past a NASA Wall-Mounted Hump

The flow past a NASA wall-mounted hump mentioned in section 4.5.3 is calculated by WA-IDDES model. Figure 5.5 shows the comparison of computed pressure distribution obtained using the WA-IDDES model, WA-DES model, WA model and SA model with the experimental data. Figure 5.6 shows the comparison of computed skin-friction distribution obtained using the same models and experimental data. It can be noted that both the WA-IDDES and WA-DES models show improved accuracy compared to WA model in predicting the pressure distribution and skin friction in most regions of the flow field. From the skin friction distribution plot, it can be noted that the predicted value by WA-DES model best matches the experimental data.

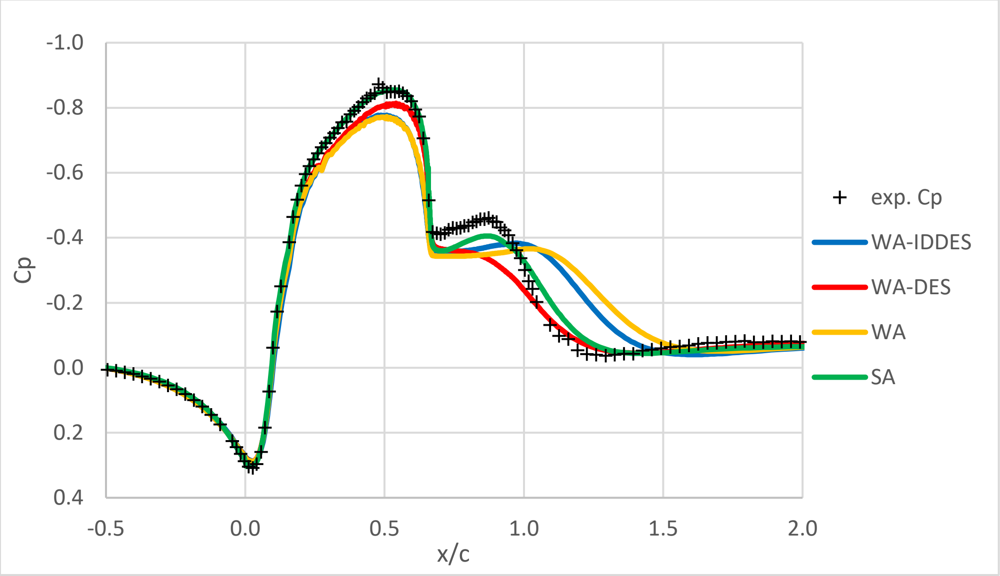

Figure 5.5: Comparison of pressure distribution on the surface of the hump.

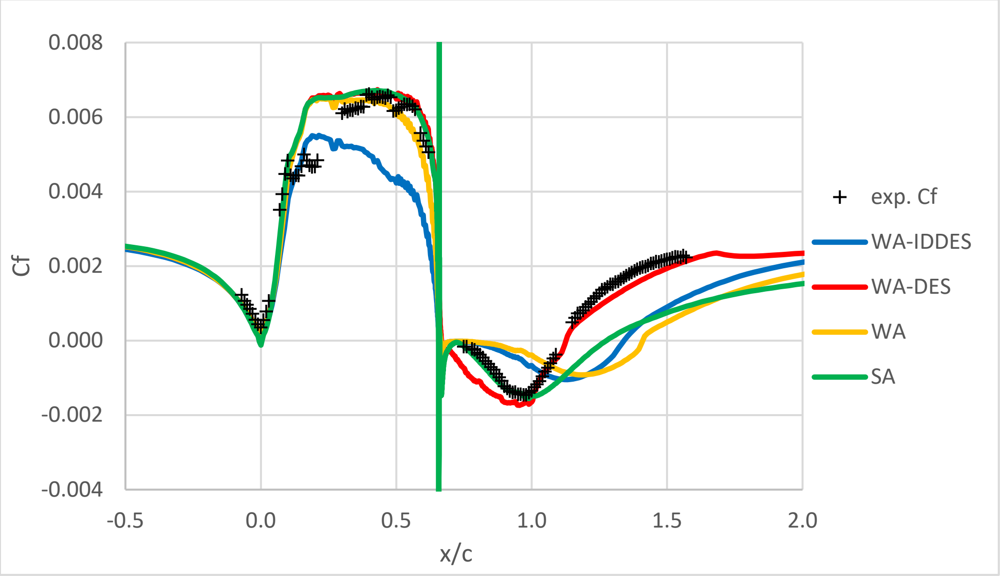

Figure 5.6: Comparison of Skin-Friction distribution on the surface of the hump.

Comparisons of the predicted velocity profiles from WA-IDDES and experimental data are shown in Figure 5.7, respectively. Comparing to the velocity profiles from WA-DES, WA and SA models in Figure 4.8, 4.9 and 4.10, it can be seen that the velocity profiles predicted by the WA-DES model agree quite well with the experimental data before and through the separation region. The WA-IDDES model shows better predictions compared to the original WA model, but the improvement is not significant.

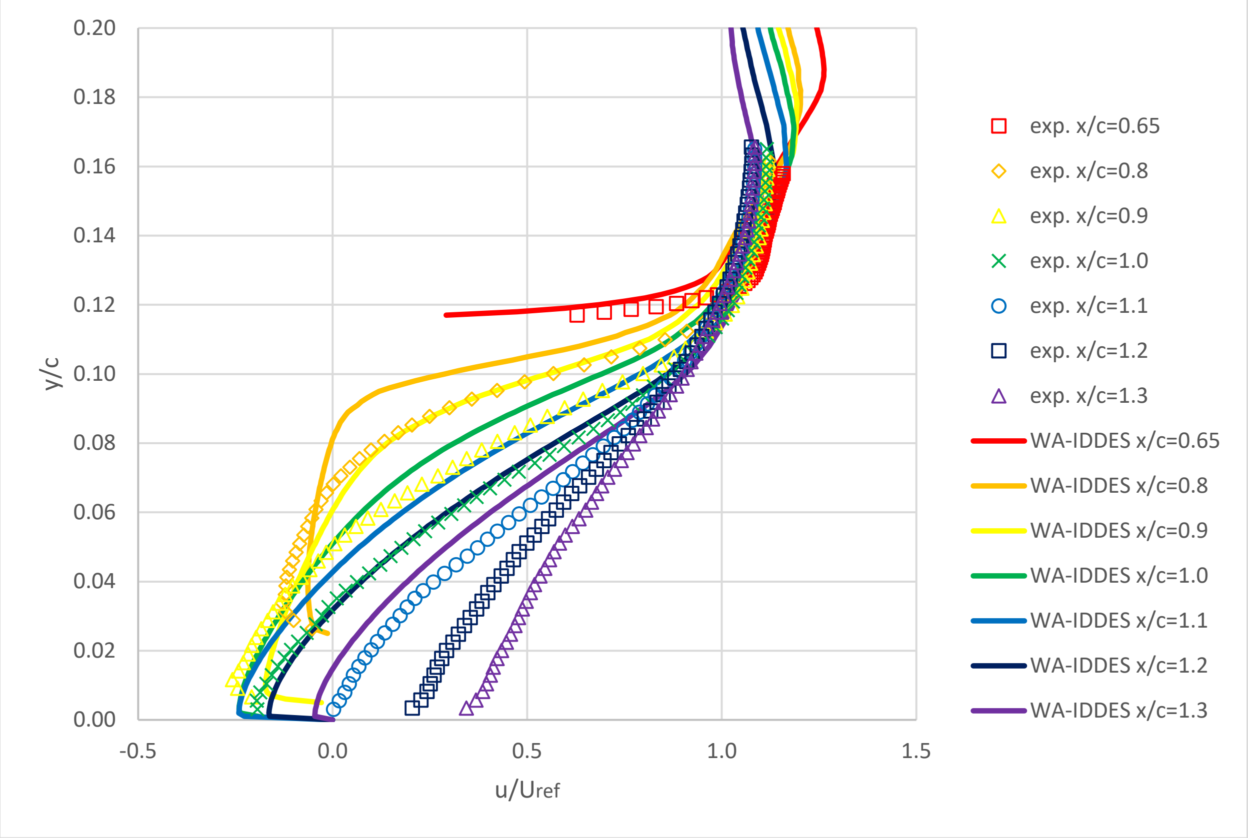

**Figure 5.7: Comparison of velocity profiles from WA-IDDES model and experimental values at various locations on the hump.**

### 5.4.2 Flow in an Asymmetric Plane Diffuser

The asymmetric plane diffuser mentioned in section 4.5.5 is computed by WA-IDDES model. Results from WA-IDDES and WA-DES models are compared to the RANS results with WA and SA models and the experimental data for both the pressure coefficient and the skin friction distribution on the bottom wall and the top wall of the diffuser. Figures 5.8 and 5.9 show the comparison of pressure distribution on the top and bottom wall of the diffuser respectively. Results of WA-IDDES model best match the experimental data. The computations from SA model have the poorest agreement with the experimental data among the three models. Figures 5.10 and 5.11 show the comparison of skin-friction distribution on the top and bottom wall of the diffuser respectively. As shown in Figure 5.11, WA-IDDES and WA models have better agreement with the experimental data for skin-friction on the bottom wall of the diffuser while the SA model shows the poorest agreement.

According to the experiment, the separation point occurs at x/H $\approx$ 6.6 and the flow reattaches at x/H $\approx$ 27.5 on the top wall. In Fig. 5.11, WA-IDDES model predicted a separation region from 5.65 to 29.77. WA-DES model predicted separation region on the bottom wall begins at x/H = 7.31 and ends at x/H = 26.13. This result is closer to the experimental value compared to that obtained using the WA and SA models, which predict the separation region on the bottom wall from x/H = 7.03 to 30.97 and x/H = 4.26 to 31.29, respectively.

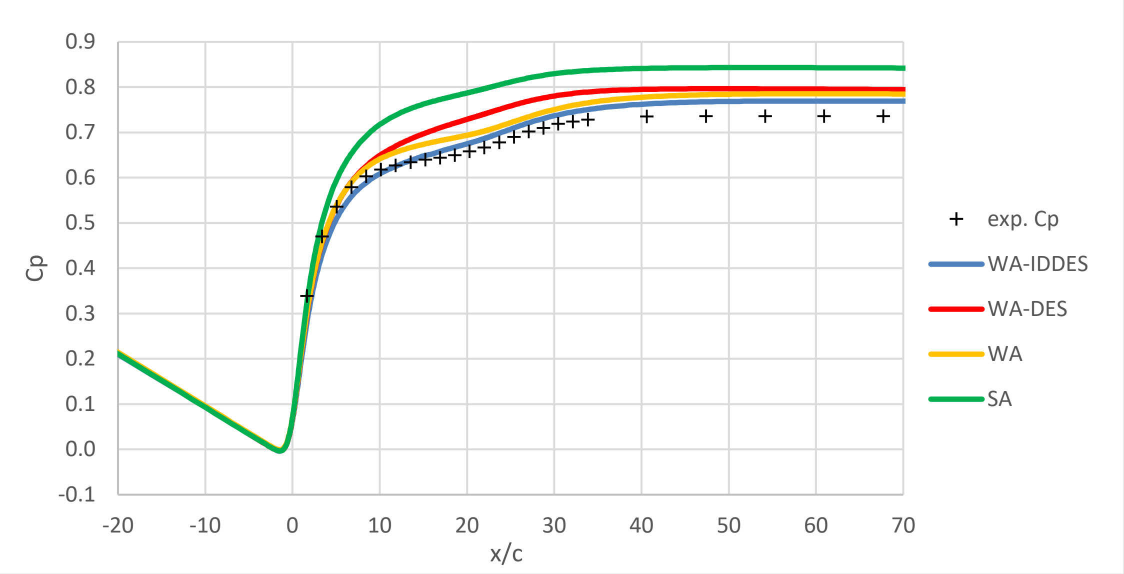

**Figure 5.8: Comparison of pressure distribution on the top wall of the diffuser.**

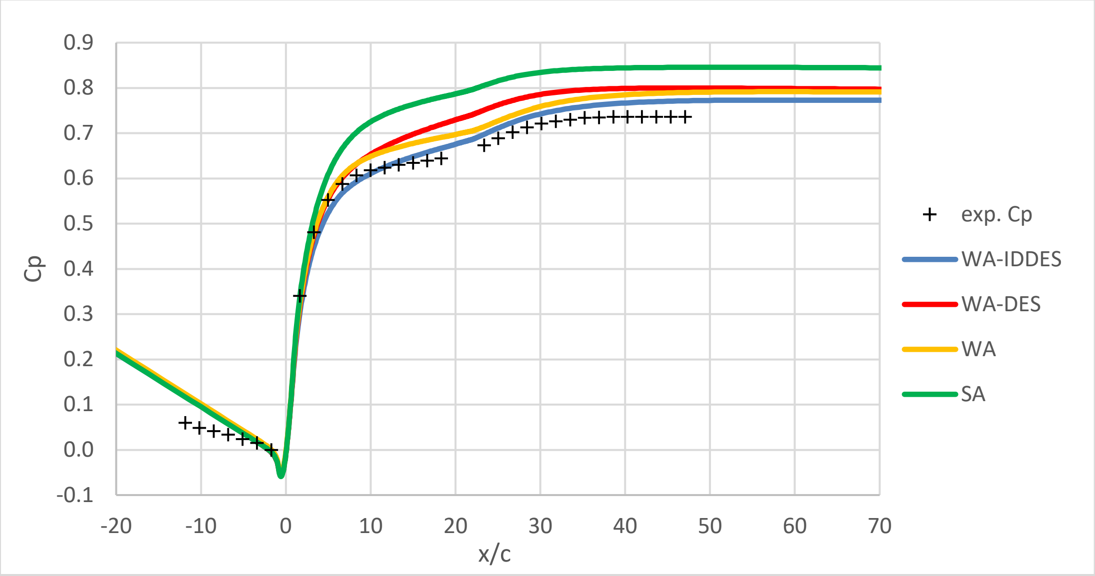

Figure 5.9: Comparison of pressure distribution on the bottom wall of the diffuser.

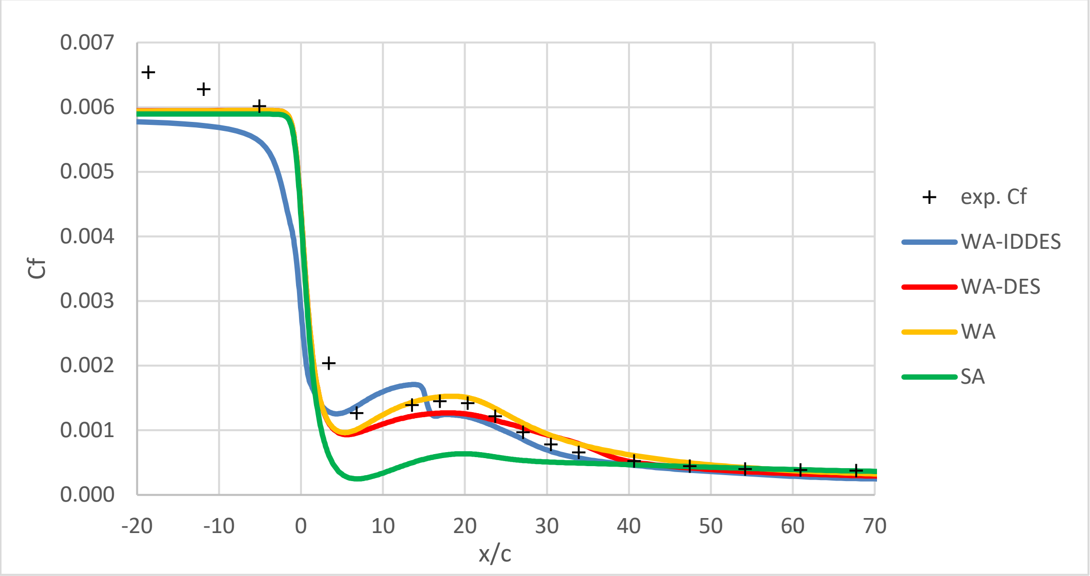

Figure 5.10: Comparison of Skin-Friction distribution on the top wall of the diffuser.

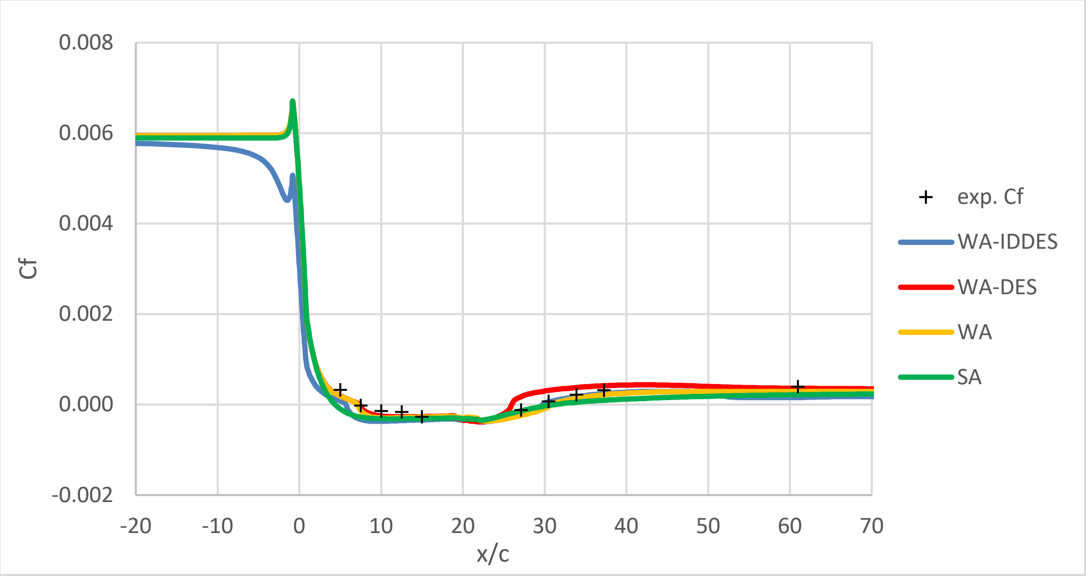

**Figure 5.11: Comparison of Skin-Friction distribution on the bottom wall of the diffuser.**

### 5.4.3 Flow over a Periodic Hill

Flow over a periodic hill is also re-calculated. Simulation results from WA-IDDES model are compared to the LES results mentioned in section 4.5.7. Figure 5.12 compares the skin friction distribution on the hill. None of the models match the LES solution very well. However, in Figures 5.13 and 5.14, the comparison of pressure coefficients on the hill and top wall show the improved results obtained by the WA-IDDES model. SA model shows the largest discrepancy in the computed pressure coefficient compared to the experimental data. Velocity profiles at ten different locations upon the hill are compared in Figure 5.15, in which the profiles computed by SA model show slightly better agreement with the experimental data than those computed by the other three models. In the beginning of separation region, at $x/h = 1$ and 2, a noticeable improvement can be seen by the WA-IDDES model compared to the WA and WA-DES models.

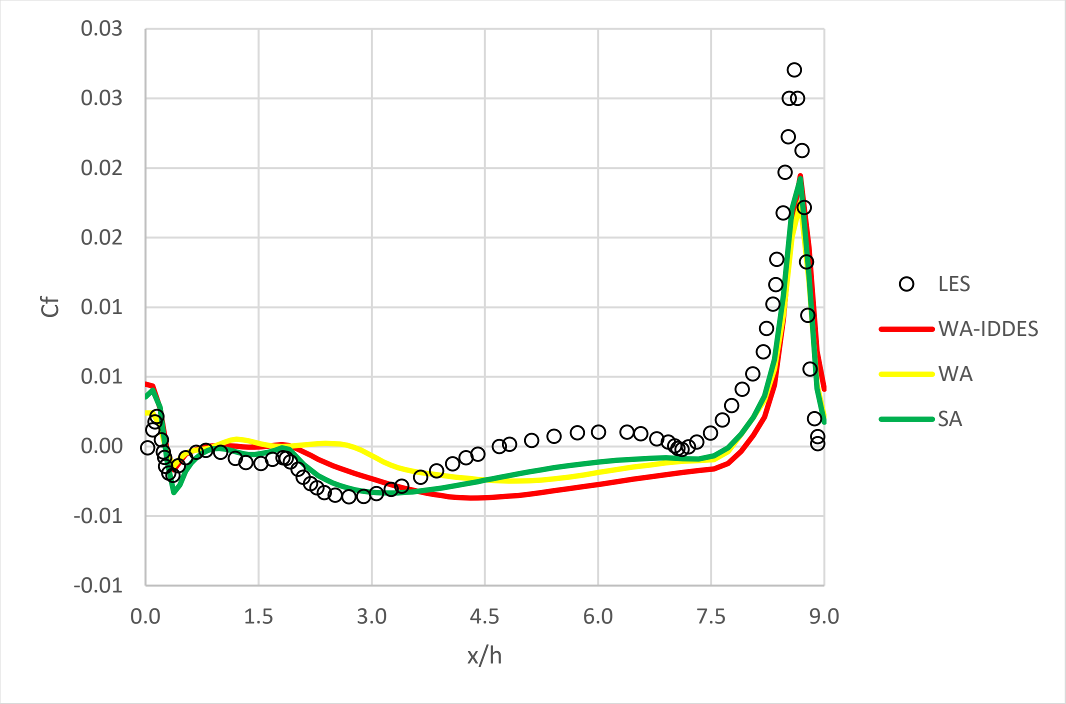

Figure 5.12: Comparison of skin friction coefficient distribution on the period hill.

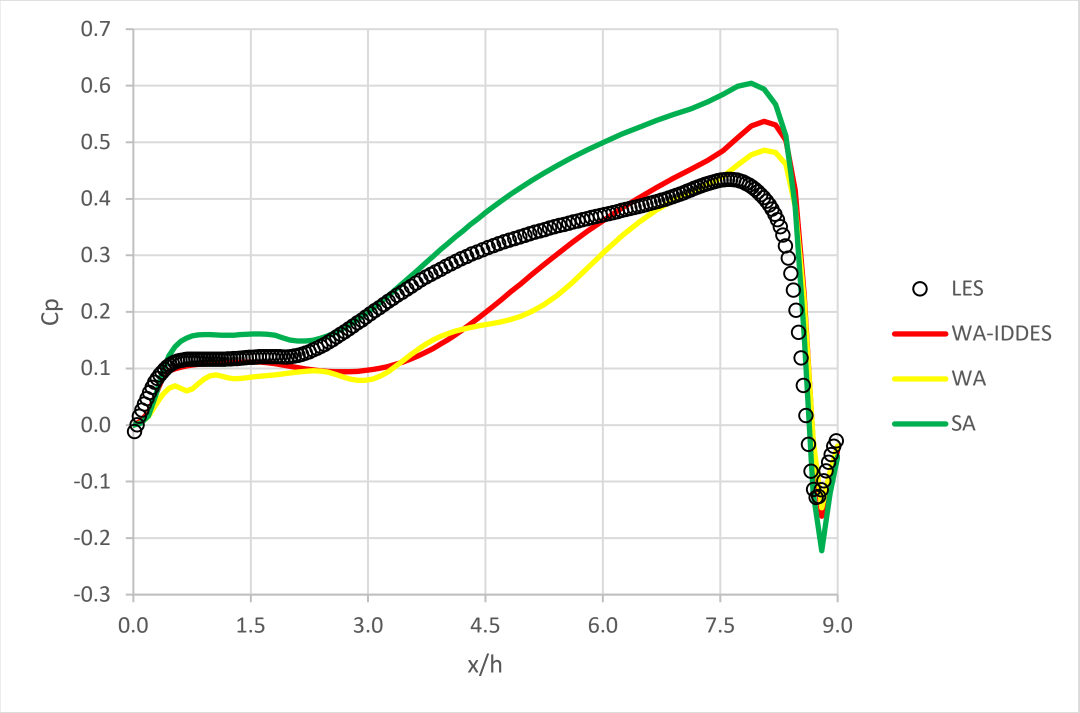

Figure 5.13: Comparison of pressure coefficient distribution on the period hill.

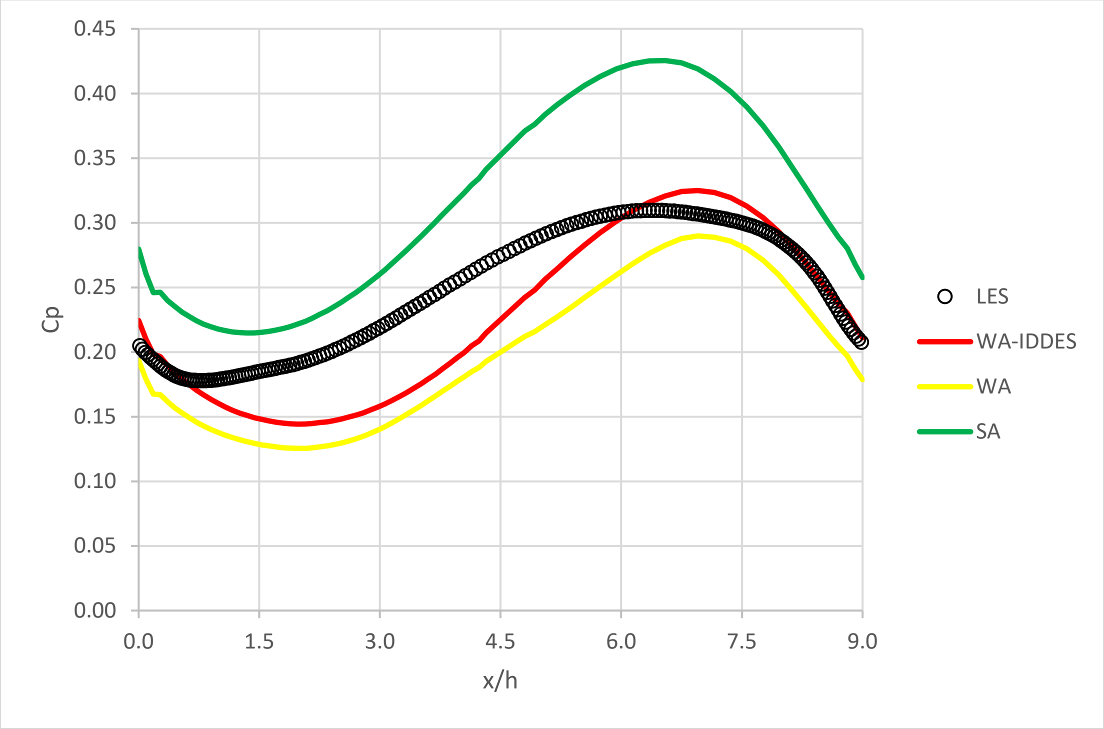

**Figure 5.14: Comparison of pressure coefficient distribution on the top wall.**

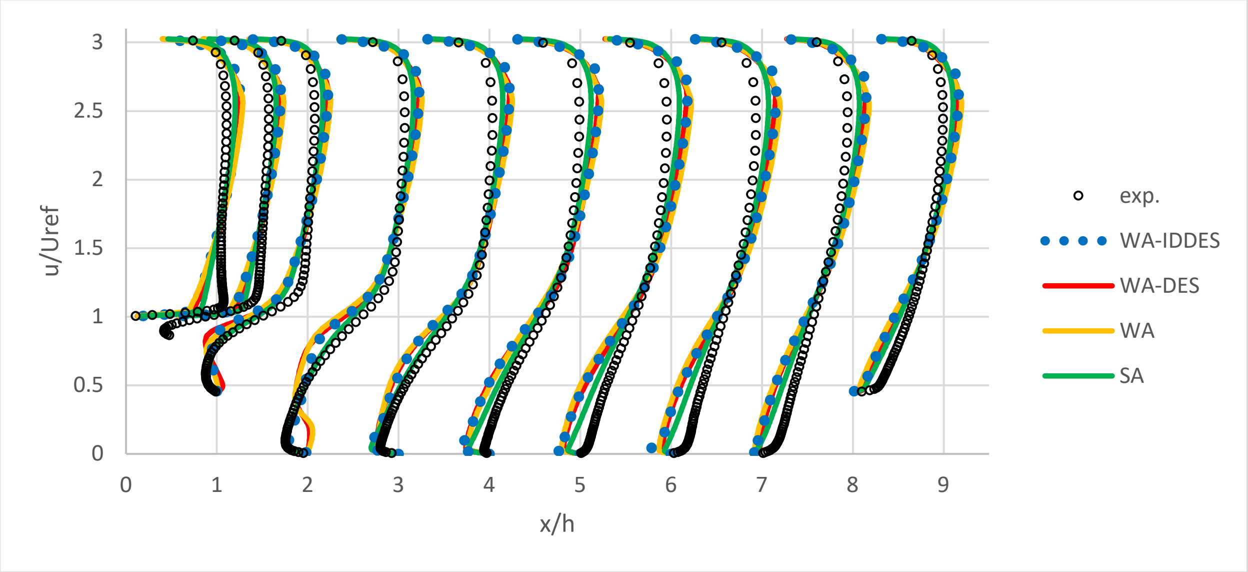

**Figure 5.15: Comparison of velocity profiles on the periodic hill.**

### 5.4.4 Flow over a Backward Facing Step

This case performed by WA-IDDES model is the backward facing step shown in section 4.5.4.

Figures 5.16 and 5.17 show the pressure distribution and skin friction coefficient respectively computed by the WA-IDDES, WA-DES, WA and SA models and their comparison with the experimental data. The computed reattachment point predicted by WA-IDDES and WA-DES is at x/H = 6.24 compared to the experimental location ranges from 6.16 to 6.36. Pressure distribution and skin friction coefficient predicted by the WA-IDDES and WA-DES models best match the experimental data. Figures 5.18 shows the comparison of computed velocity profiles obtained using the WA-IDDES models with the experimental data. Velocity profiles from WA-IDDES at x/H = 4 is closer to the experimental results compared to the other models, but the discrepancy between the computations and experimental data becomes larger when the flow approaches and moves beyond the reattachment point (e.g. at x/H = 6 and 10). All the WA models generally give the same results, which show better agreement with the experimental data compare to the result of SA model.

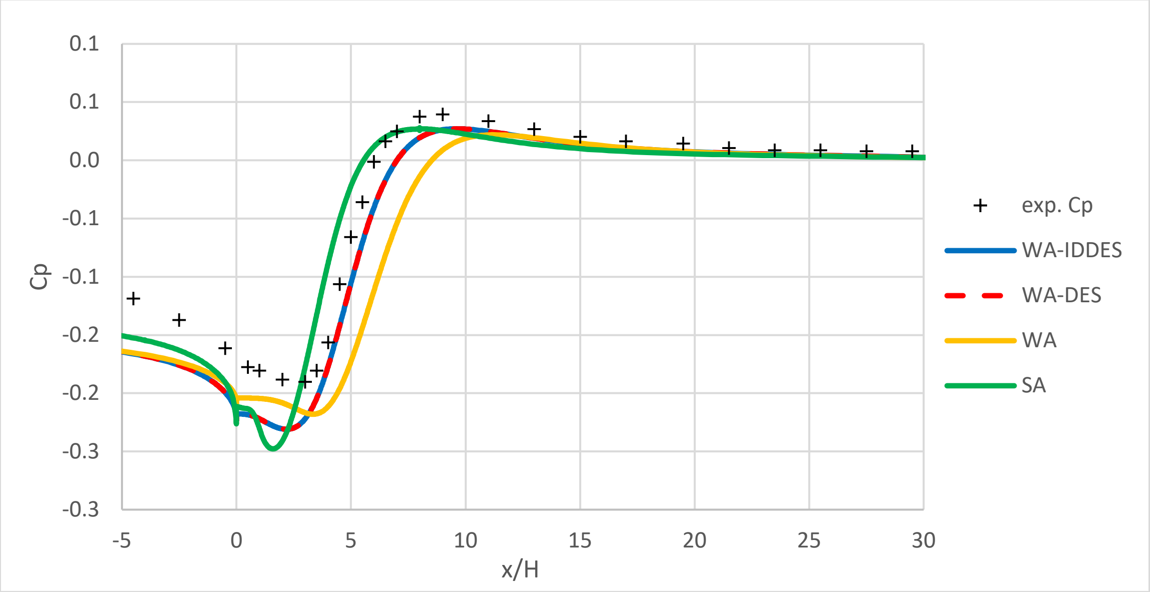

**Figure 5.16: Comparison of pressure distribution on the surface of the backward facing step.**

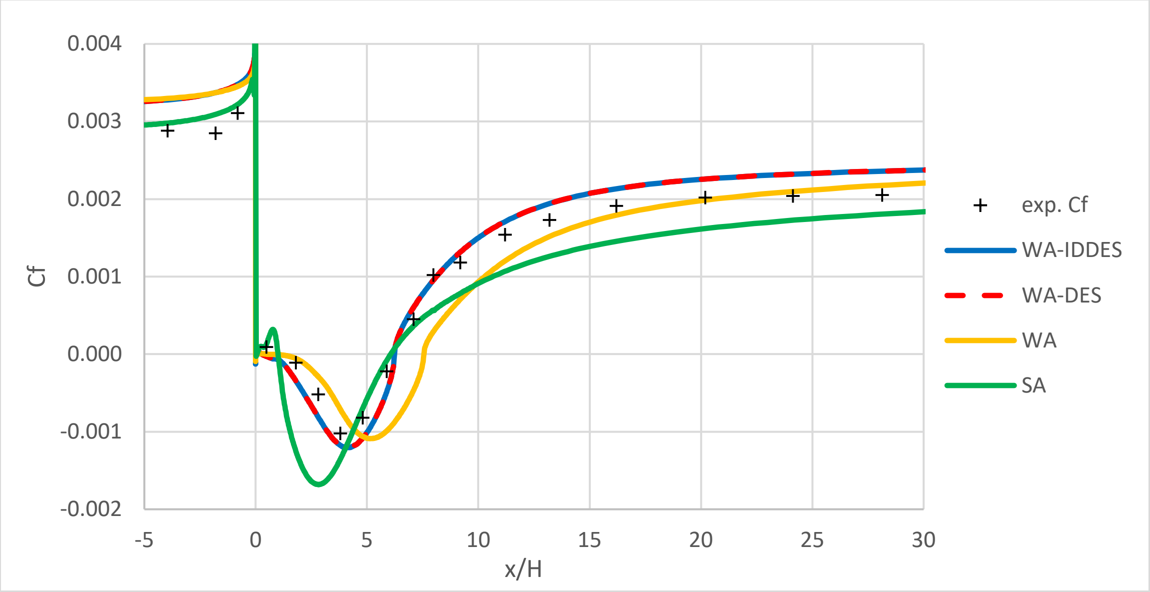

Figure 5.17:Comparison of pressure distribution on the surface of the backward facing step.

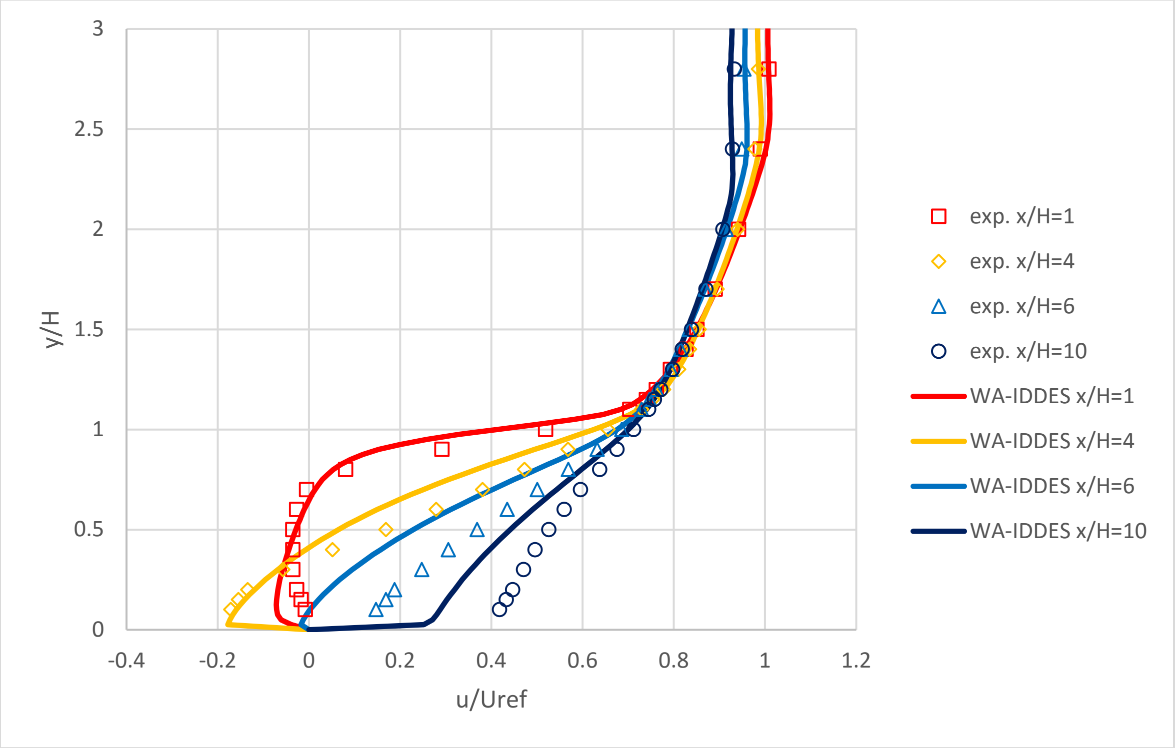

Figure 5.18:Comparison of velocity profiles computed from WA-IDDES model and experimental values at various locations on the backward facing step.

## 5.4.5 Flow over a Curved Backward Facing Step

The flow past a curved backward facing step has been investigated by Bentaleb et. al. using LES [36]. The Reynolds number based on step height H and inlet velocity Uin is 13,700. The averaged LES result on fine grid indicates that the flow separates at x/H = 0.83, and reattaches at x/H = 4.36. Calculations by Lardeau and Billard [37] show a huge discrepancy between the SST *k*-*ω* model and LES results. As a result, SST *k*-*ω* model is also need to compute this case for comparison. Comparison of pressure coefficient is shown in Figure 5.19 below. In the separation region, WA-IDDES has the best agreement with LES followed by the results from WA-DES and WA model, respectively. SA model and SST *k*-*ω* model predict a much higher and low pressure compared to the LES result. For skin friction coefficient shown in Figure 5.20, SST *k*-*ω* model predicts the separation point precisely, but is not able to accurately predict the reattachment point. Other models have better predictions near the reattachment point.

The velocity profiles at 8 different locations on this curved step are compared in Figure 5.21 and 5.22 for hybrid models and the RANS models, respectively. All the WA models show similar results for velocity profiles, and all the models have close prediction at the beginning of the step (x/H = 0.5 ~ 1.0). However, the predictions by SA and SST *k*-*ω* models show a larger mismatch with LES result in the following regions.

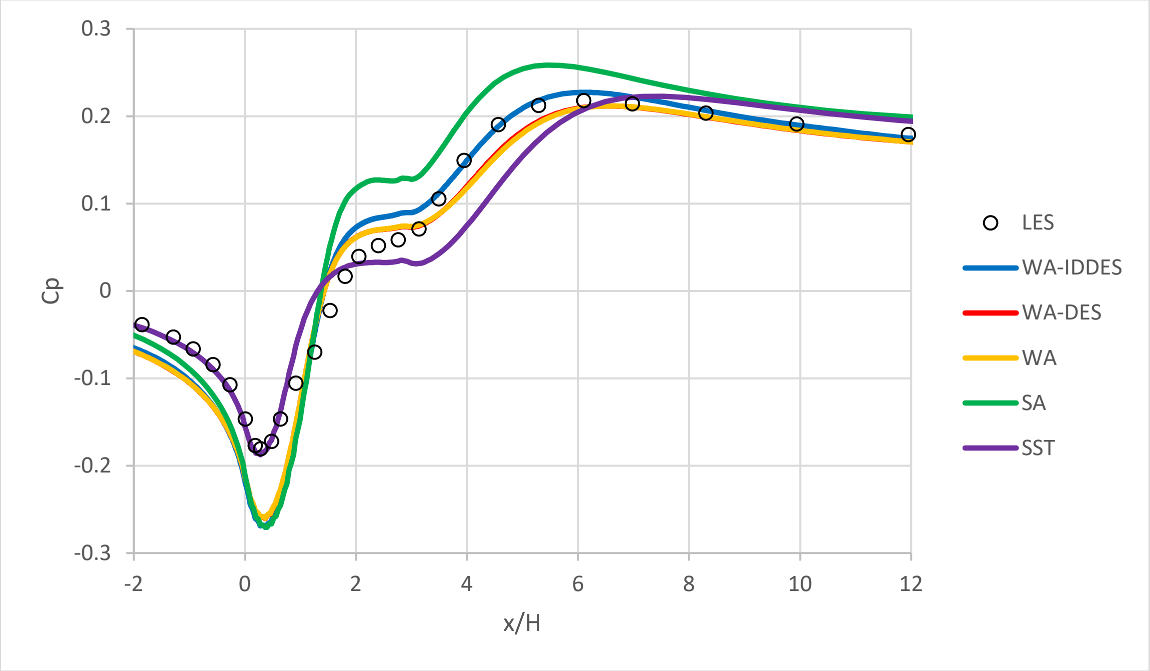

**Figure 5.19: Comparison of pressure distribution on the surface of the curved backward facing step.**

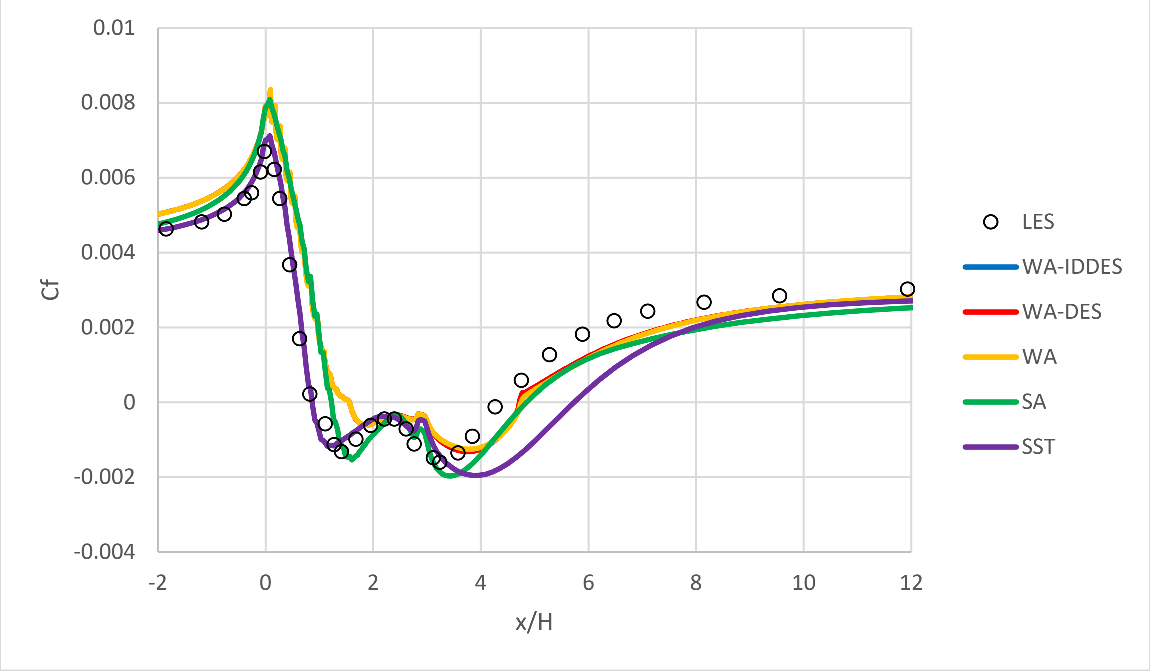

**Figure 5.20:Comparison of skin-friction distribution on the surface of the curved backward facing step.**

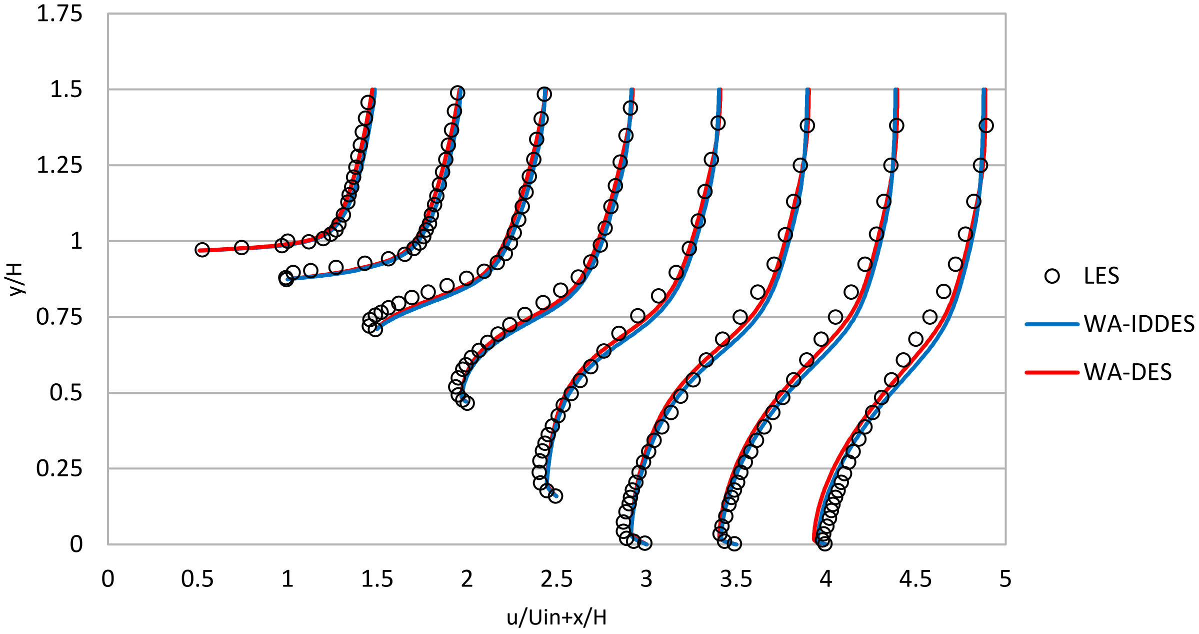

Figure 5.21: Comparison of vertical velocity profiles computed from hybrid models and LES at various locations on the backward facing step.

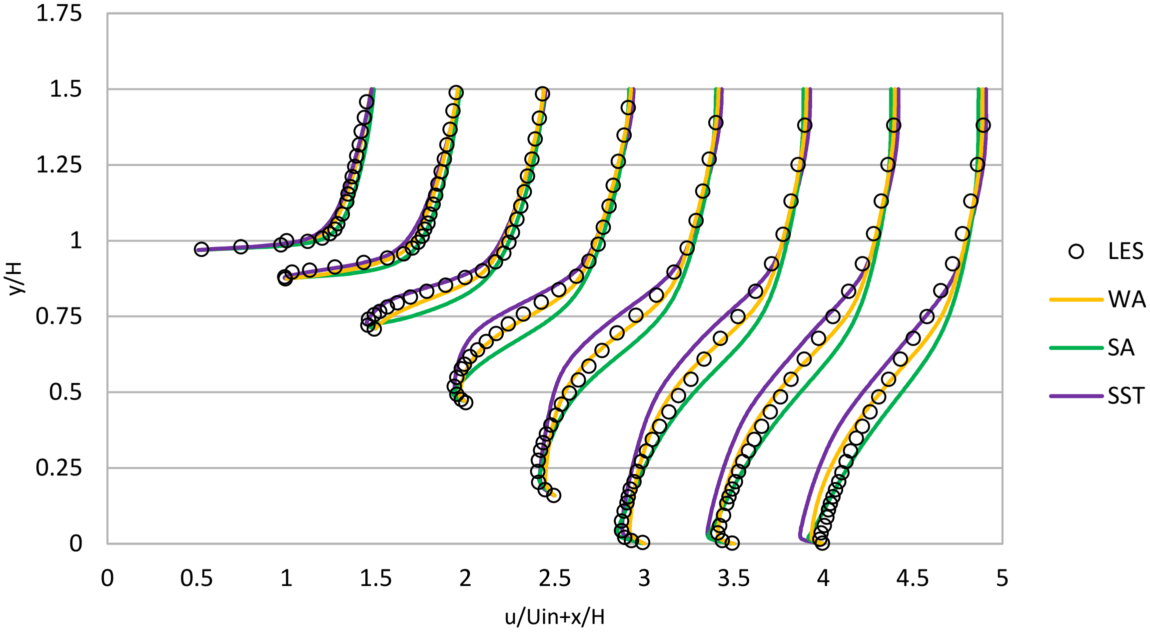

Figure 5.22: Comparison of vertical velocity profiles computed from RANS models and LES at various locations on the backward facing step.

### 5.4.6 Transonic Flow over an Axisymmetric Bump

The last case performed by WA-IDDES model is the axisymmetric bump shown in section 4.5.8. The predicted pressure coefficients along the bump surface are compared to the experimental data in Figure 5.23. Followed by WA-IDDES model, WA-DES model matches the experimental data more closely than the WA and SA model, in particular the WA-DES model improves the result of WA model in the near shock region as well as in the separation region. In a small region after the reattachment (x/c = 1.1 to 1.3), the result of WA model is better than the other three models. Predicted separation and reattachment points are compared to the experimental data in Table 5.1. WA model has a relatively large error in predicting the separation point, which is improved by the WA-IDDES and WA-DES model.

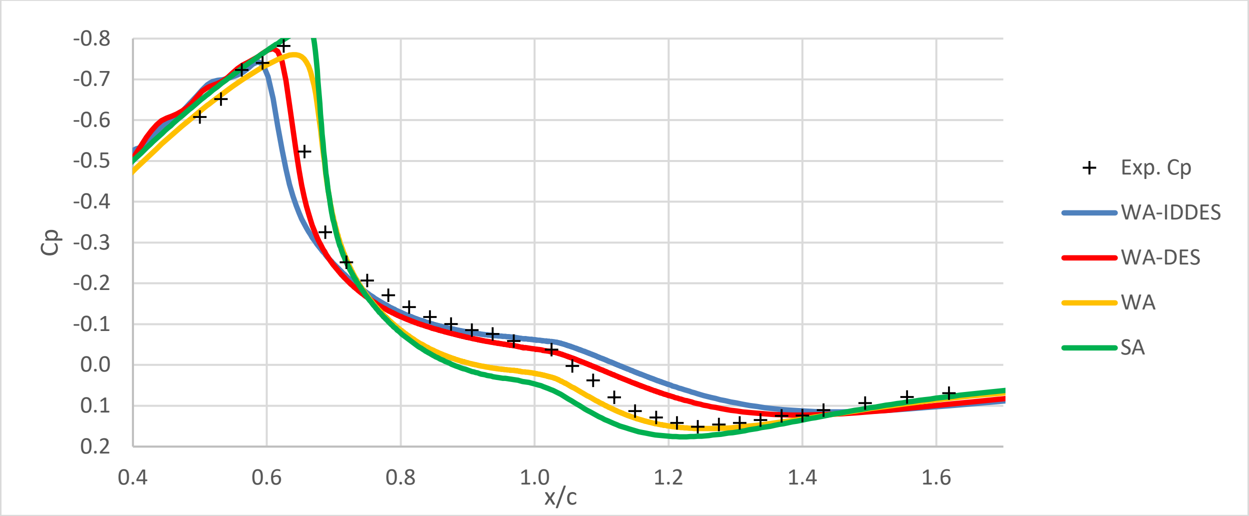

**Figure 5.23: Comparison of pressure coefficient distribution on the surface of the axisymmetric bump.**

**Table 5.1: Comparison of flow separation and reattachment points of the axisymmetric bump.**

| | Experiment | WA-IDDES | %Error | WA-DES | % Error | WA | % Error | SA | % Error |
|---|---|---|---|---|---|---|---|---|---|
| Separation | 0.7 | 0.66 | 5.71 | 0.70 | 0.57 | 0.82 | 16.71 | 0.69 | 1.71 |
| Reattachment | 1.1 | 1.22 | 10.91 | 1.17 | 6.00 | 1.12 | 2.09 | 1.16 | 5.46 |

The comparisons of velocity profiles between the experimental data and the computed results from the WA-IDDES model are presented in Figure 5.24. Results from WA-DES, WA and SA model have been presented in chapter 4 in Figure 4.36, 4.37 and 4.38, respectively. Before the separation region (x/c = -0.25 and 0.688), WA-DES and WA model better predict the experimental velocities. In the separation region (x/c = 0.813 and 1), WA-IDDES model has a better match with experimental velocities compared to WA model, and WA-DES model has the best result. After the separation (x/c = 1.125 and 1.375), the velocity profiles from SA model are closest to the experimental values. However, all the WA based models are not significantly worse than the SA model in this region.

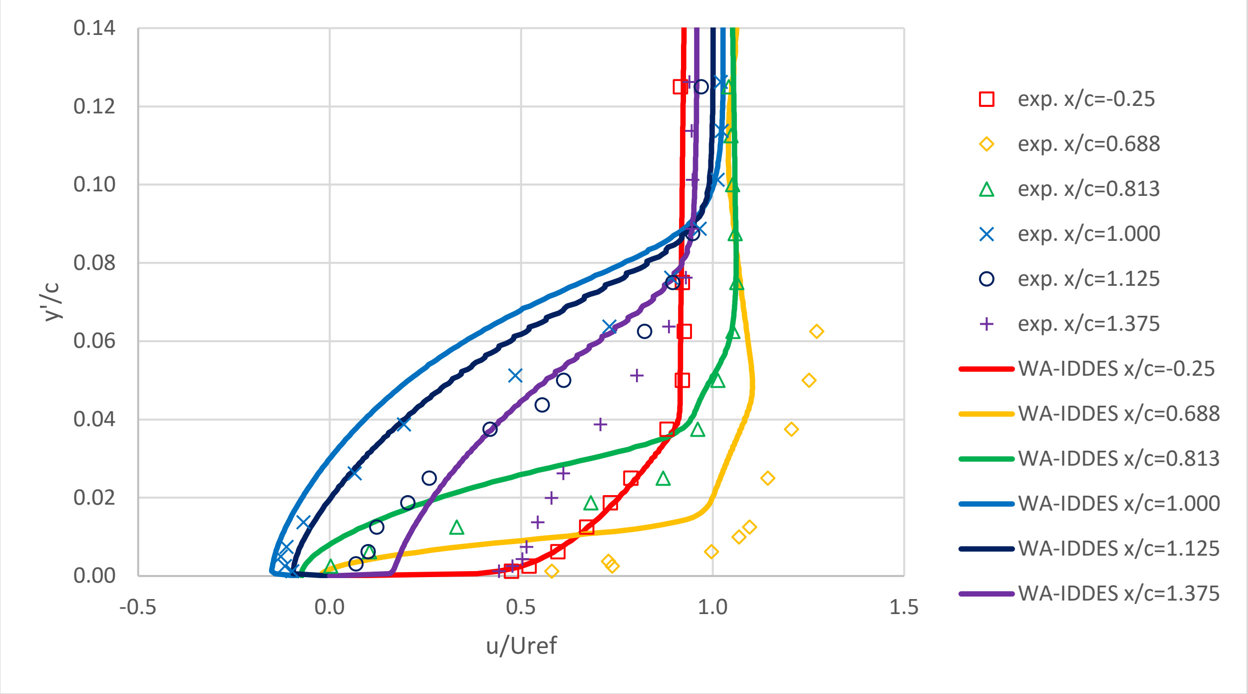

**Figure 5.24: Comparison of vertical velocity profiles computed from WA-IDDES model and experimental values at various locations on the axisymmetric bump.**

# Chapter 6: The Wall Distance Free Approach and Elliptic Blending

## 6.1 Introduction

The following three modifications to the original WA model (WA2017) are made to improve its accuracy in WA2017 model.

### 6.1.1 Zero Strain-Rate Correction

Under the condition of zero-strain rate *S* which may occur locally in the flow field, the last two terms in Eq. (11) can become singular. Even bounding *S* by a very small value may not be sufficient for obtaining accurate solutions. It has been observed that in the region of zero or very low strain rates, the turbulent viscosity ratio computed by these types of models exhibits a very sudden decrease which results in overestimation of local velocity. The turbulent flow in a channel is a typical example of this behavior. While approaching the central region, turbulence viscosity ratio computed by the Wray-Agarwal (WA2017) model drops rapidly, which results in an overestimation in local velocity. Thus, a kink is produced in the computed velocity field at the center of the channel. To compensate for the turbulent viscosity decrease in the central essentially uniform flow region of the channel, WA2017 model is modified. This modification is described in section 6.2.1.

### 6.1.2 Wall Distance Free Approach

Wall distance is an important parameter in many turbulence models, including most widely used Spalart-Allmaras model, $k$-$\varepsilon$ model and SST $k$-$\omega$ model. However, it is also known to introduce inaccuracies near the curved boundaries which are also present in flow with complex geometries. Furthermore, the presence of wall distance parameter also significantly increases the computational cost in applications with dynamic boundary which may require frequent mesh regeneration. Rahman et al. developed a wall distance free modified Spalart-Allmaras Model that can be easily applied to arbitrary complex computational domains with structured or unstructured grids [38]. This model is also claimed to have better performance in predicting flow separation, as well as is less sensitive to inflow turbulent intensity. Goldberg et al. applied the wall distance free approach to $k$-$\varepsilon$ and SST $k$-$\omega$ model [39, 40]. These wall distance free versions also show their ability to better capture the reverse flow behavior in flow separation region, ability to calculate applications with arbitrary topologies and moving surface on both structured and unstructured grids, and are even more robust in numerical stability [39, 40].

### 6.1.2 Elliptic Blending

Elliptic blending introduces near wall anisotropy in turbulence model via an elliptic equation. In elliptic blending, the wall blocking is governed by an elliptic partial differential equation (a Helmholtz-type equation) which accounts for nonlocal near-wall effects. Elliptic blending can successfully address the problem of log-layer mismatch in the turbulent boundary layer. Thus, it provides a cheaper alternative for one-equation models compared to two-equation turbulence models while retaining some of the near-wall properties of two-equation models. Durbin et al. [41], Rahman et al. [42, 43] and Elkhoury [44] have employed a Helmholtz-type relaxation equation along with a one-equation model to account for the wall-blocking effect.

## 6.2 Derivations of Various Modifications to WA2017 Model

### 6.2.1 Derivation of Zero Strain-Rate Correction to Wray-Agarwal Model

In simulating the turbulent flow in a 2D channel using the WA2017 model, a kink is observed in the velocity profile at the center of the channel. The source of the turbulence was disappeared due to strain rate $S \rightarrow 0$ in the transport Eq. (11) of WA model. $S$ is used to imitate specific turbulence dissipation rate $\omega$ in $k$-$\omega$ closure, which is defined by the velocity gradient. After combine the $k$ and $\omega$ equations of SST $k$-$\omega$ model, $S$ becomes dominant of the two destruction terms. At the center of channel, $S \rightarrow 0$ due to zero velocity gradient. In the CFD code, $S$ can be bounded by a very small value (usually the precision limit of the computer) to avoid the division zero error in the central region of the channel. However, this fix still results in a relatively very large destruction term, which leads to reduce the transport variable $R$ to a very small value. Since the WA model defines the turbulent viscosity to be proportional to $R$, the turbulent viscosity is artificially reduced to a very small value.

This problem is rectified by bounding the last term in Eq. (11). This type of bound has also been proposed by Menter [45] in his formulation of an eddy viscosity transport equation based on the $k$-$\epsilon$ closure. Such a behavior has also been observed in the $k$-$kL$ model [46] which was fixed by $k$-$kL$ MEAH model [47] by providing a bound on the turbulent kinetic energy production term. Similar bound is added to the WA2018-EB model to address this problem. The last term in Eq. (11) is modified as:

$$-(1-f_1)min\left[C_{2k\varepsilon}R^2\left(\frac{\frac{\partial S}{\partial x_j}\frac{\partial S}{\partial x_j}}{S^2}\right), C_m\frac{\partial R}{\partial x_j}\frac{\partial R}{\partial x_j}\right] \qquad (38)$$

### 6.2.2 Derivation of Wall Distance Free Wray-Agarwal Model

Rahman et al. derived a wall distance free version of Wray-Agarwal model, by following the work of the wall distance free Spalart-Allmaras (SA) model [38]. Unlike the SA model, which uses wall distance directly in its transport equation as a turbulence length scale, Wray-Agarwal model relies on wall distance only to switch between the term associated with $k$-$\varepsilon$ and $k$-$\omega$ behavior if the model. A different switching function $f_1$ is therefore derived to formulate the wall distance free WA model. In a private communication, two different approaches have been suggested by Rahman to construct a new switching function for the wall distance free WA model. Both approaches preserve the characteristics of the original Wray-Agarwal model. In the original WA model, the switching function is given by:

$$f_1 = tanh(arg_1^4) \tag{39}$$

where $arg_1$ is a function of the wall distance as described by Eq. (16).

**The First Approach**

In this formulation, we begin with the turbulence length-scale in $k$-$\varepsilon$ closure:

$$d_t = \frac{\tilde{C}_\mu^{\frac{3}{4}}}{\kappa}\frac{k^{\frac{3}{2}}}{\varepsilon} = \frac{\tilde{C}_\mu^{\frac{3}{4}}}{\kappa}\frac{\sqrt{k}}{C_\mu \omega} \tag{40}$$

In Eq. (40), $k$ and $\omega$ are determined by the Bradshaw-relation.

$$\begin{gathered} k = \frac{\nu_T S}{\sqrt{C_\mu}} \\ \omega = \frac{S}{\sqrt{C_\mu}} \end{gathered} \tag{41}$$

and $\tilde{C}_\mu$ is determined by:

$$\begin{gathered} \tilde{C}_\mu = \frac{1}{2\left(1 + T_t S\sqrt{1 + \Re^2}\right)} \\ T_t = \frac{k}{\varepsilon} = \frac{1}{C_\mu \omega} \\ \Re = \left|\frac{W}{S}\right| \\ W = \sqrt{2W_{ij}W_{ij}}\,, \qquad W_{ij} = \frac{1}{2}\left(\frac{\partial u_i}{\partial x_j} - \frac{\partial u_j}{\partial x_i}\right) \\ C_\mu = 0.09\,, \qquad \kappa = 0.41 \end{gathered} \tag{42}$$

The $arg_1$ in Eq. (40) is defined as:

$$arg_1 = 5\tilde{C}_\mu \frac{\nu + R}{S\kappa^2 {d_t}^2} \tag{43}$$

**The Second Approach**

In this formulation, $\varepsilon$ is related to $\omega$ by using the relationship between the near-wall dissipation rate and viscous-diffusion rate [48]:

$$\begin{gathered} \varepsilon = C_\mu k\omega \sim \nu\eta^2 \\ \eta = S\, max\left(1, \left|\frac{W}{S}\right|\right) \end{gathered} \tag{44}$$

The $arg_1$ function is defined as:

$$arg_1 = \frac{\nu + R}{2} \frac{\eta^2}{C_\mu k\omega} \tag{45}$$

In the WA2018-EB model, the second approach is chosen due to its simplicity and robustness.

### 6.2.3 Derivation of Elliptic Blending for Wray-Agarwal Model

It has been shown by several investigators [41-44] that by including an elliptic blending model with a turbulence model, the anisotropic low Reynolds number near wall effects can be more accurately captured. The model equation for elliptic blending is generally expressed as:

$$-{L_R}^2 \nabla^2 P_R + P_R = -C_{3k\omega} R \frac{\partial^2 R}{\partial {x_j}^2} + RS \tag{46}$$

where $P_R$ is a production term which couples Eq. (46) with a modified model Eq. (47) given below. In Eq. (46), the diffusion/destruction term $C_{3k\omega} R \frac{\partial^2 R}{\partial {x_j}^2}$ can be neglected in most cases without affecting the accuracy. The coupled WA model equations with elliptic blending take the form:

$$\frac{\partial R}{\partial t}+\frac{\partial u_j R}{\partial x_j}=\frac{\partial}{\partial x_j}\left[(\sigma_R R+\nu)\frac{\partial R}{\partial x_j}\right]+RS(C_1-1)+P_R+f_1 C_{2k\omega}\frac{R}{S}\frac{\partial R}{\partial x_j}\frac{\partial S}{\partial x_j}$$
$$-(1-f_1)min\left[C_{2k\varepsilon}R^2\left(\frac{\frac{\partial S}{\partial x_j}\frac{\partial S}{\partial x_j}}{S^2}\right),C_m\frac{\partial R}{\partial x_j}\frac{\partial R}{\partial x_j}\right] \tag{47}$$
$$-{L_R}^2\nabla^2 P_R+P_R=RS$$

It should be noted that the near-wall turbulence eddies follow the Kolmogorov scaling (i.e. the turbulence fluctuations depend on the laminar viscosity). Therefore, $\nu/S$ can be used for the viscous scaling serving as a lower bound on the turbulent length scale $L_R$. In Eq. (48) for $L_R$, $C_l$ term is included for the same reason as $C_m$ in Eq. (38) to correct for the free stream behavior of $L_R$. In Eq. (48), $L_{ref}$ is the reference length scale:

$$ {L_R}^2=\frac{max(C_{3k\omega}R,C_l\nu)}{S+\frac{C_l\nu}{{L_{ref}}^2}} \tag{48}$$

The WA model given by Eqs. (47) and (48) is designated as WA2018-EB. It is a wall distance free model; therefore $f_1$ function in this model is the same as that given in Eqs. (39), (44) and (45). The values of the changed and new constants in WA2018-EB model are listed below. It should be noted that some of these constants are different from those given in Eq. (17) for the original WA2017 model, and there are three additional constants given in Eq. (49).

$$\begin{gathered}C_{1k\omega}=0.2 \quad C_{1k\varepsilon}=0.094\\ C_{2k\omega}=2.63 \quad C_{2k\varepsilon}=1.24\\ C_w=5.97\\ C_l=4.0+\sqrt{\chi}\\ C_{3k\omega}=0.171\end{gathered} \tag{49}$$

Eq. (47) represents two coupled equations for $R$ and $P_R$; they require boundary conditions to be solved numerically. The boundary conditions are:

$$
\begin{gathered}
R_{farfield} = 3\nu_{\infty}\ to\ 5\nu_{\infty} \\
R_{wall} = 0 \\
P_{R_{initialfield}} = 0\ to\ RS \\
P_{R_{wall}} = 0
\end{gathered}
\tag{50}
$$

## 6.3 Validation Cases

### 6.3.1 Fully Developed Channel Flow for Wide Range of Reynolds Numbers

Fully developed turbulent channel flow is a basic verification/validation case for any turbulence model. Channel flows at five different friction Reynolds numbers ranging from 182 to 5200 are calculated by WA2017 and WA2108-EB models; the results for velocity profiles are compared to the DNS data by Lee and Moser [49].

From Figures 6.1-6.5, it can be seen that the original WA2017 model predicts the velocity in the near wall region and outer layer region very well. However, there is a mismatch at beginning of the log layer (y+ $\approx$ 20) between the WA2017 computations and DNS data in all cases; however, the WA2018-EB model substantially improves the velocity profiles in the log region and agrees with the DNS data in all regions of the turbulent boundary layer.

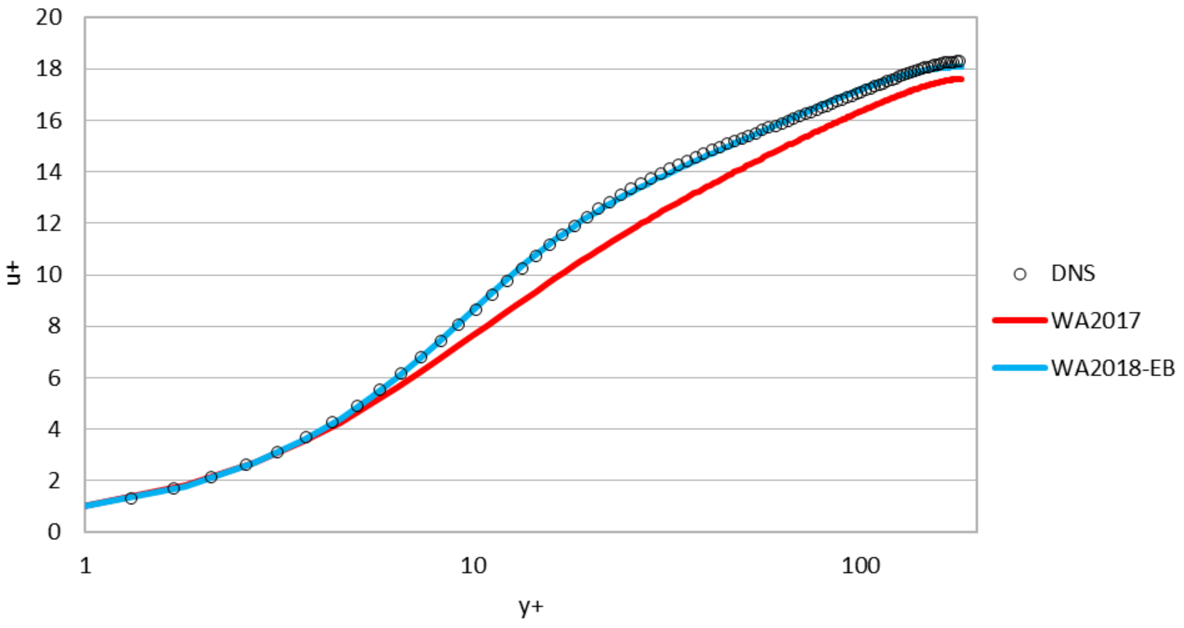

Figure 6.1: Comparison of velocity profile in the channel at $Re_\tau$ = 182.

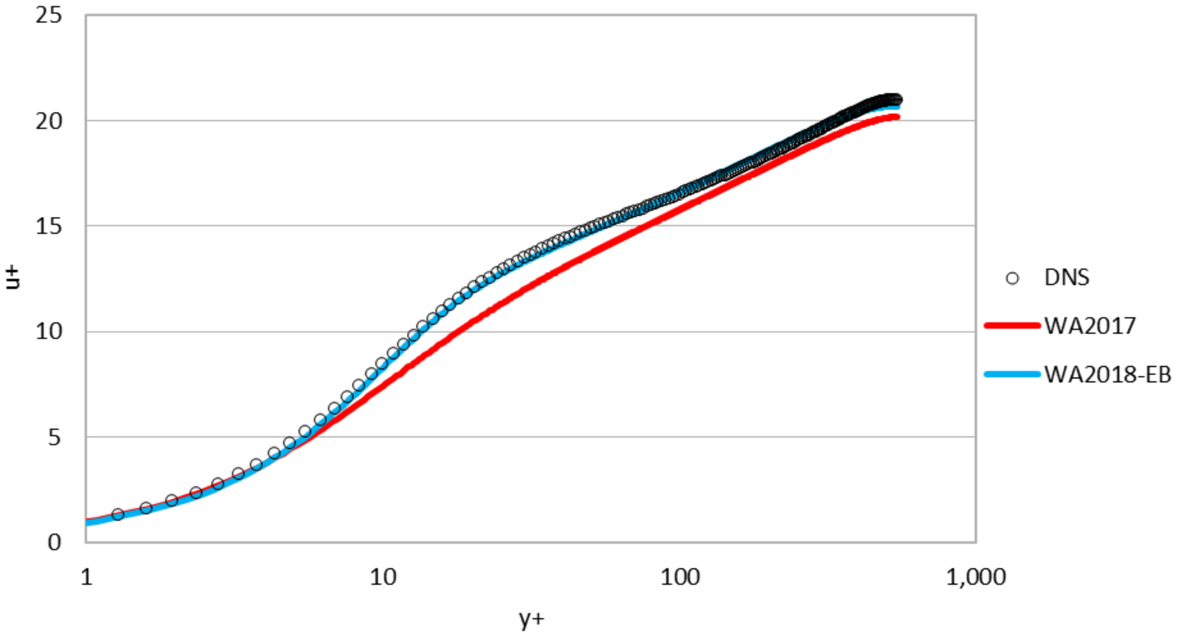

Figure 6.2: Comparison of velocity profile in the channel at $Re_\tau$ = 550.

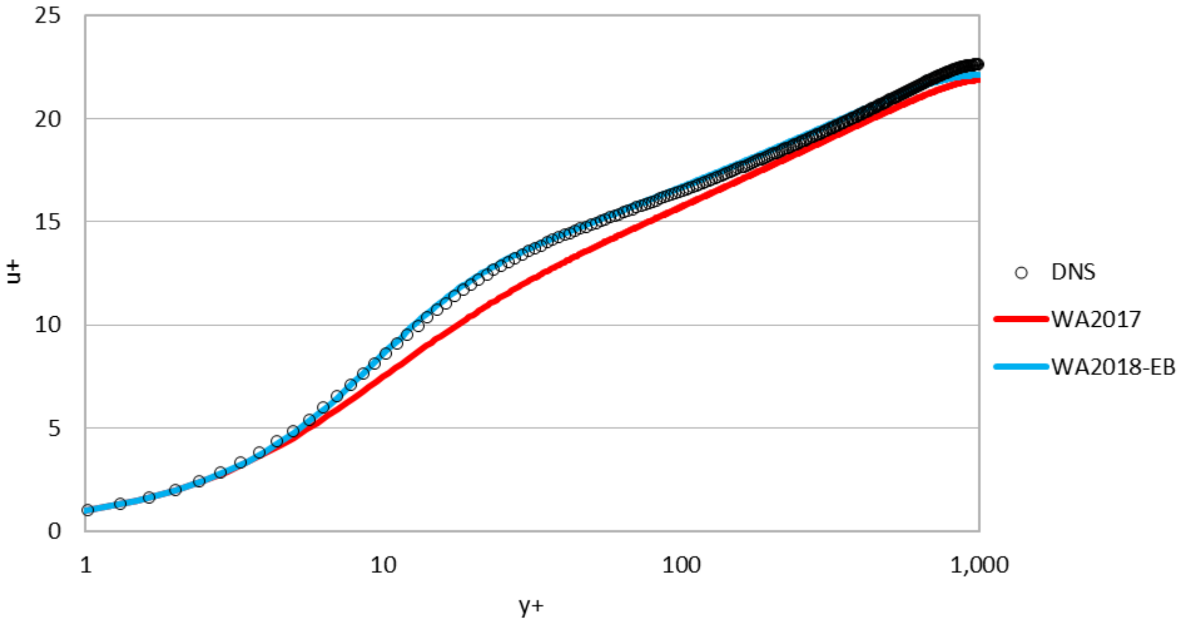

Figure 6.3: Comparison of velocity profile in the channel at $Re_\tau = 1000$.

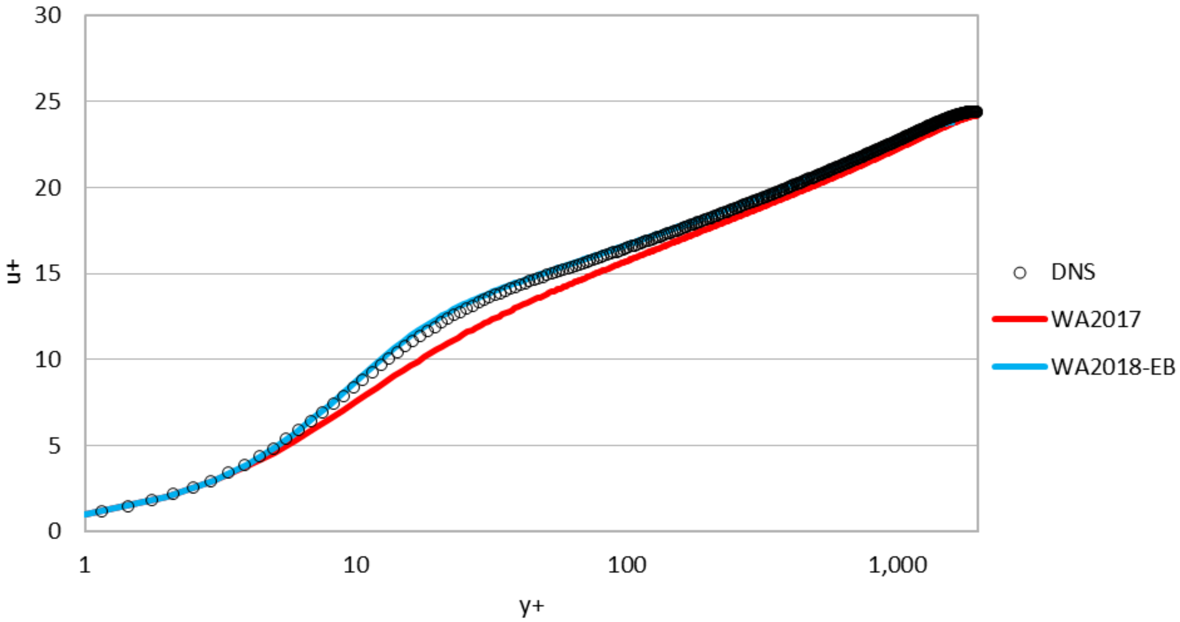

Figure 6.4: Comparison of velocity profile in the channel at $Re_\tau = 2000$.

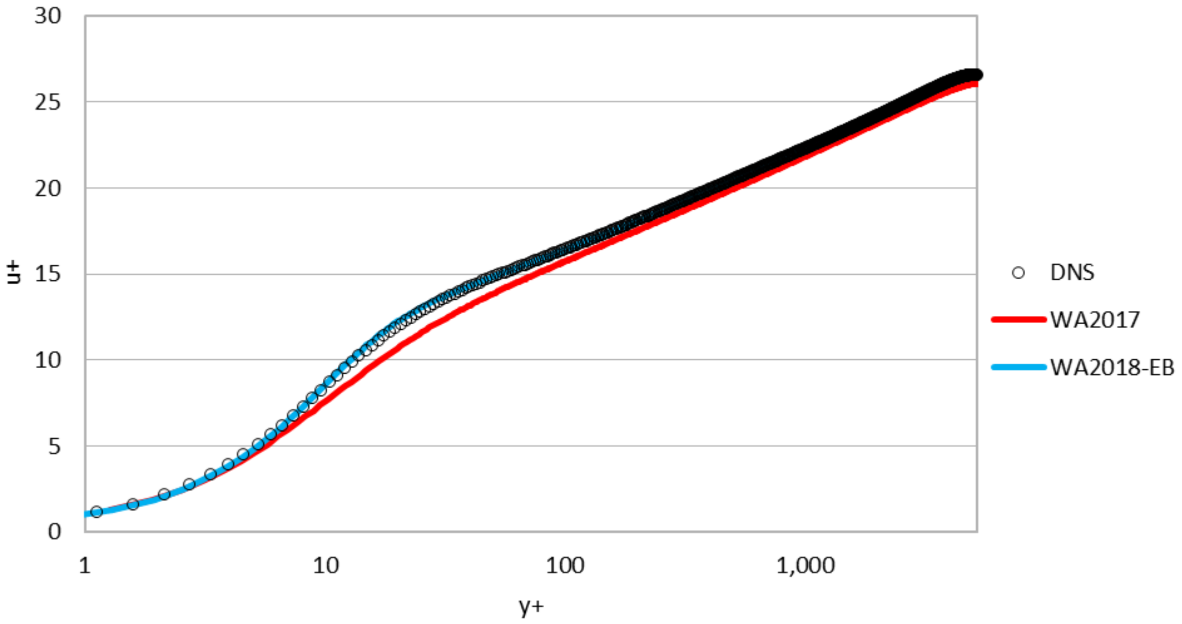

**Figure 6.5: Comparison of velocity profile in the channel at $Re_\tau$ = 5200.**

Channel flow at very high Reynolds number from NASA TMR [20] is also considered to test the capability of the WA2018-EB model. For this case, the inflow Mach number is 0.2 and the Reynolds number based on the channel height is 80 million. The velocity and turbulent viscosity profile at location x = 500 are compared using the SA, SST *k-ω*, WA2017 and WA2018-EB models.

From Figure 6.6, it can be noted that the velocity profile computed with WA2017 model has a “kink” in the middle of the channel due to the large decrease in turbulent viscosity ratio as shown in Figure 6.7. The modification of the last term in Eq. (47) which bounds the destruction term in WA2018-EB model prevents the decrease in turbulent viscosity, and therefore velocity profile computed from WA2018-EB model perfectly matches the velocity profile from SA and SST *k-ω* model.

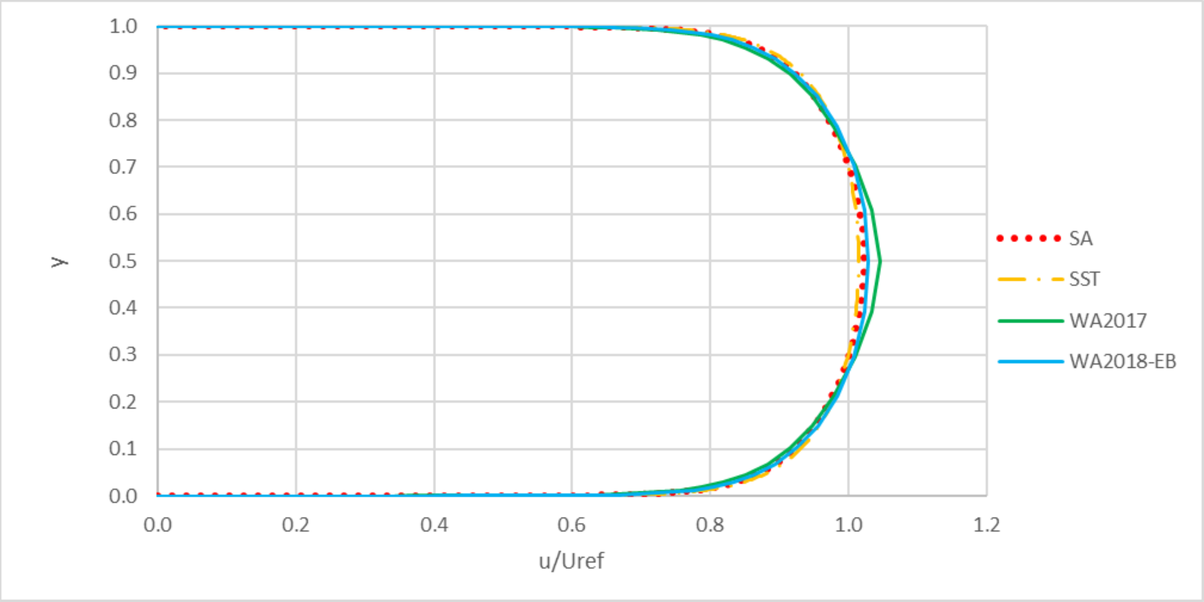

**Figure 6.6: Comparison of velocity profile in turbulent channel at $Re_h = 80x10^6$ at x=500.**

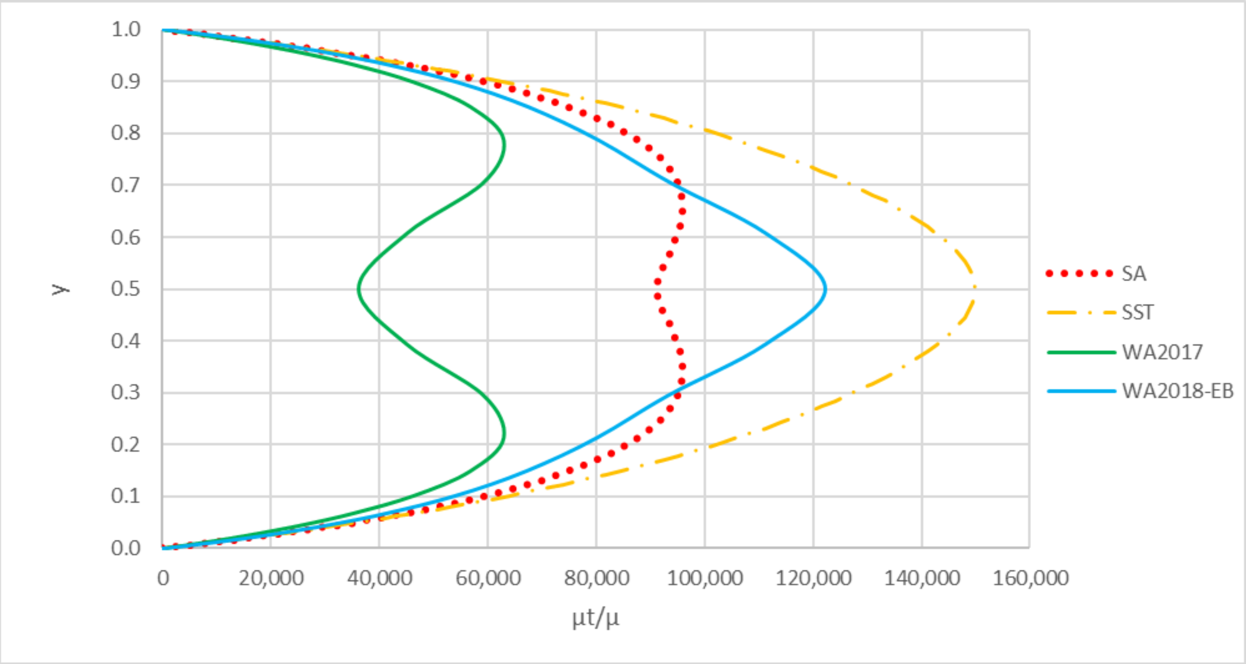

**Figure 6.7: Comparison of turbulent viscosity ratio in channel at $Re_h = 80x10^6$ at x=500.**

### 6.3.2 Flow over a Backward Facing Step

Flow over a backward facing step described in section 4.5.4 is recomputed. Pressure distribution and skin friction coefficient are computed by the WA2018-EB model. The comparison with the WA2017 and SA models, and the experimental data is shown in Figures 6.8 and 6.9. The computed reattachment point is at x/H = 6.88 using the WA2018-EB model compared to the experimental location which ranges from 6.16 to 6.36. Pressure distribution and skin friction coefficient predicted by the WA2018-EB model show better agreement with the experimental data. Figures 6.10, 4.14, 4.15 and 4.16 show the comparison of computed velocity profiles obtained using the WA2018-EB, WA2017 and SA model with the experimental data, respectively. Velocity profiles from WA2018-EB and WA2017 models at x/H = 1 and x/H = 4 are closer to the experimental results compared to the SA model, but the discrepancy between the computations and experimental data becomes larger when the flow approaches and moves beyond the reattachment point (e.g. at x/H = 6 and 10). In the region closer to the step, the WA2018-EB model has better prediction compared to WA2017 model. Overall, all the models show reasonable agreement with the experimental data.

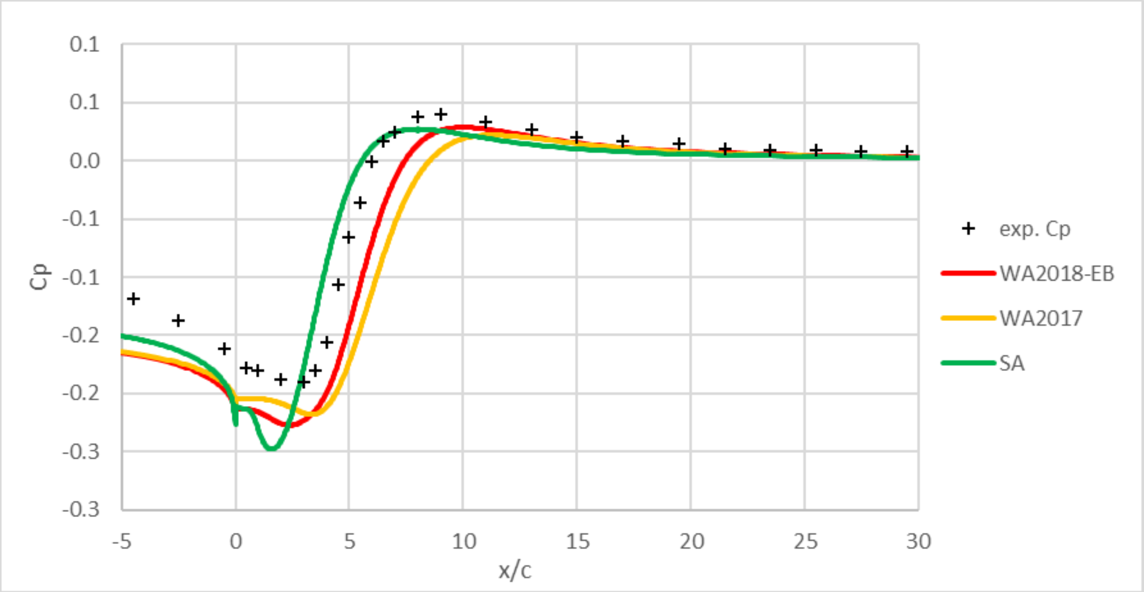

**Figure 6.8: Comparison of pressure distribution on the surface of the backward facing step.**

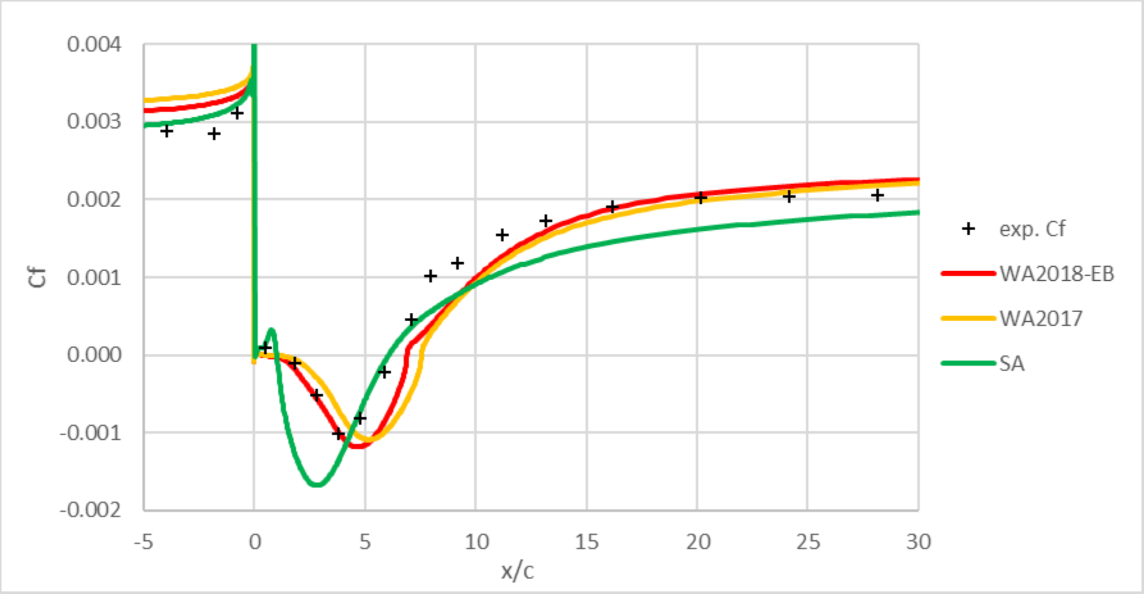

**Figure 6.9: Comparison of Skin-Friction distribution on the surface of the backward facing step.**

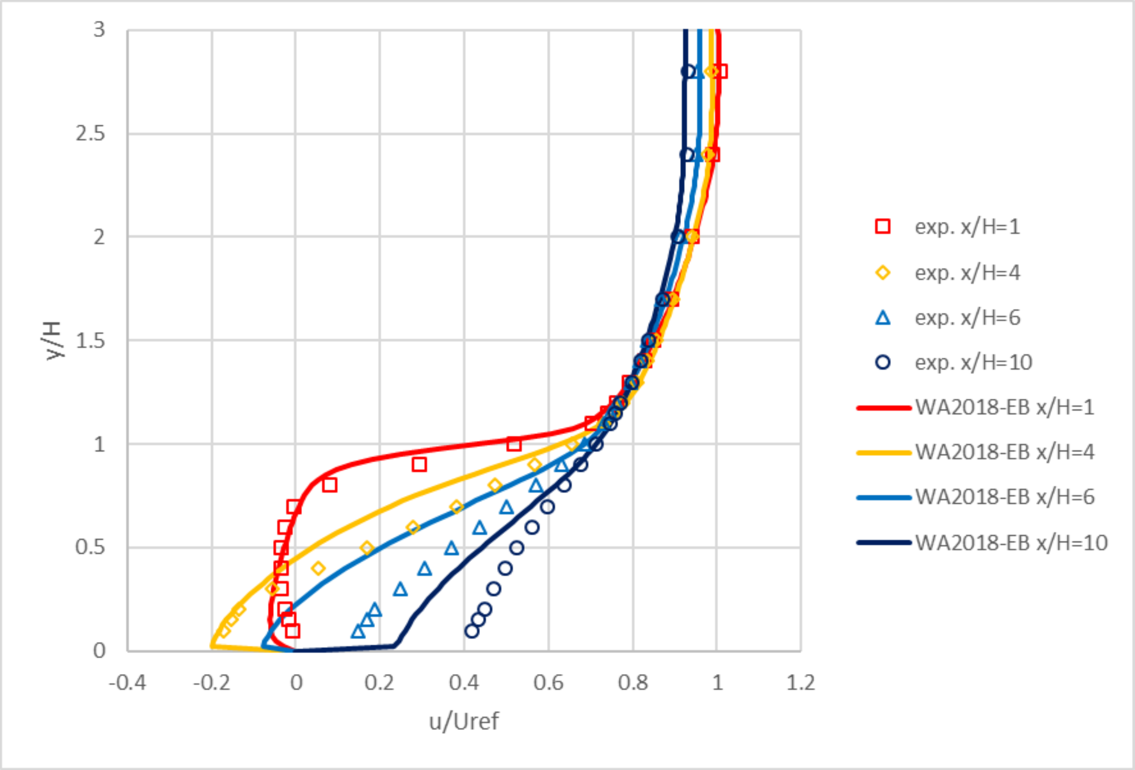

**Figure 6.10: Comparison of velocity profiles from WA2018-EB model and experimental data at various locations on the step.**

### 6.3.3 Flow over a Periodic Hill

The flow over a periodic hill is also chosen to test the capability of the WA2018-EB model.

Figure 6.11 compares the skin friction distribution on the hill. SA model has the best agreement, but WA2018-EB model still gives better result compare to the original WA2017 model, especially in the separation region where the skin friction is below zero. In Figures 6.12 and 6.13, the comparison of pressure coefficients on the hill and top wall respectively show the improved results obtained by the WA2018-EB model. SA model shows the largest discrepancy in the computed pressure coefficient compared to the experimental data. Velocity profiles at ten different locations upon the hill are compared in Figure 6.14, in which the profiles computed by SA model show slightly better agreement with the experimental data than those computed by WA2017 and WA2018-EB models. However, the irregularity in the velocity profile in the near wall region produced by WA2017 model does not exist in the WA2018-EB model.

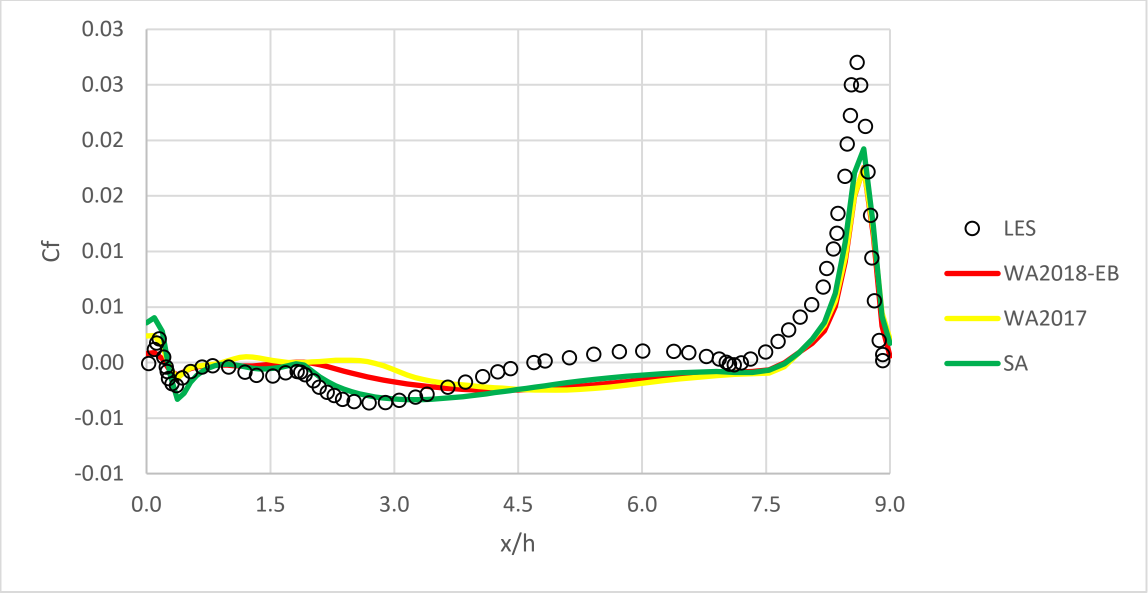

**Figure 6.11: Comparison of Skin-Friction distribution on the bottom surface of the periodic hill.**

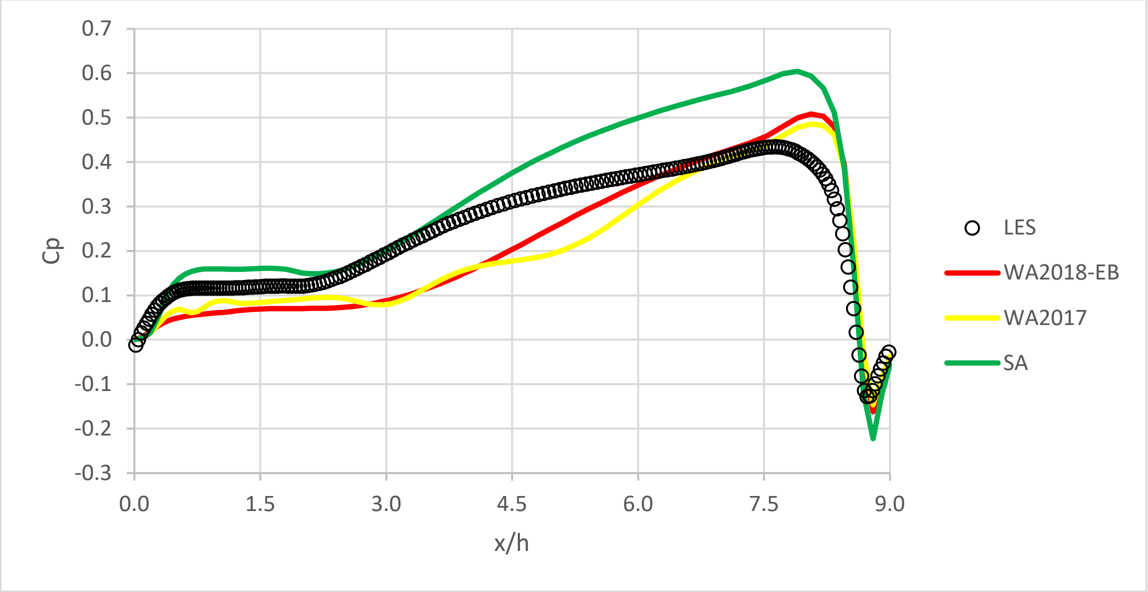

Figure 6.12: Comparison of pressure coefficient distribution on the bottom surface of the periodic hill.

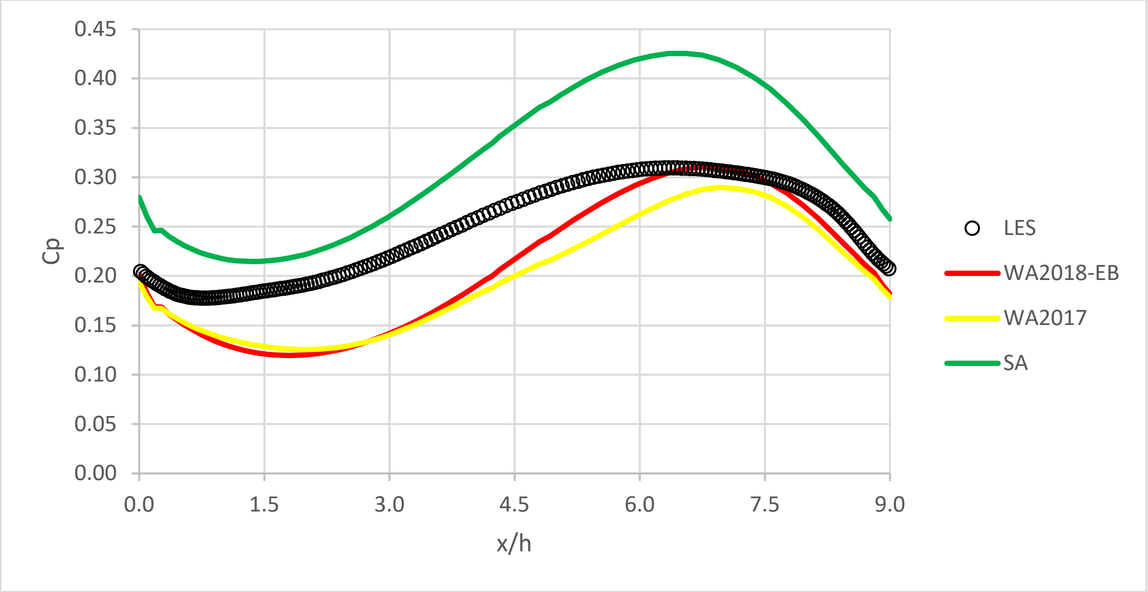

Figure 6.13: Comparison of pressure coefficient distribution on the top surface of the periodic hill.

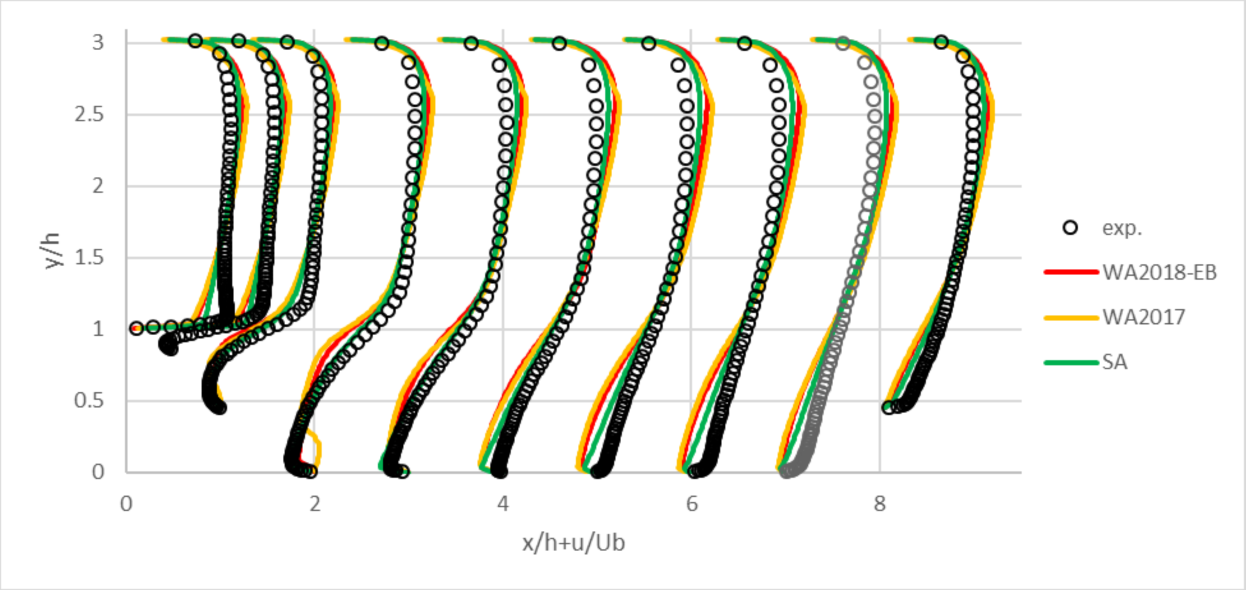

**Figure 6.14: Comparison of computed velocity profiles and experimental data at various locations on the hill.**

### 6.3.4 Transonic Flow over an Axisymmetric Bump

Axisymmetric bump shown in section 4.5.8 is also considered for testing the capability of WA2018-EB model. The predicted pressure coefficients along the bump surface are compared to the experimental data in Figure 6.15. The WA2018-EB model matches the experimental data more closely than the original WA2017 model in the separation region. Predicted separation and reattachment points are compared to the experimental data in Table 6.1. WA2018-EB model has an overall smaller error in predicting the separation and reattachment points compare to the original WA2017 model.

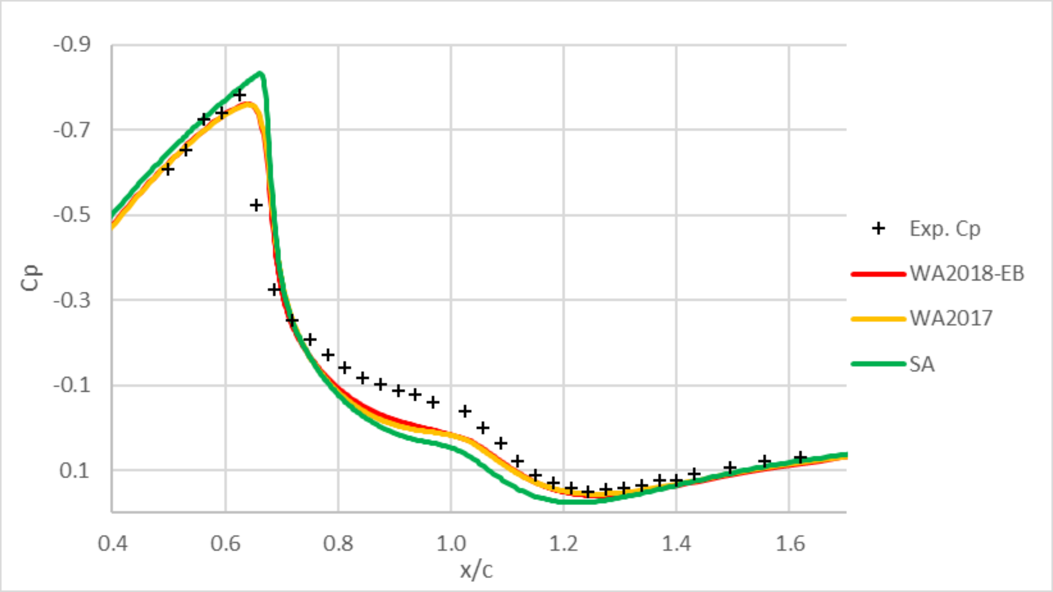

**Figure 6.15: Comparison of pressure coefficient distribution on the surface of the axisymmetric bump.**

**Table 6.1: Comparison of flow separation and reattachment points of the axisymmetric bump.**

| | Experiment | WA2018-EB | % Error | WA2017 | % Error | SA | % Error |
|---|---|---|---|---|---|---|---|
| Separation | 0.7 | 0.727 | 3.857 | 0.817 | 16.71 | 0.688 | 1.71 |
| Reattachment | 1.1 | 1.134 | 3.091 | 1.123 | 2.09 | 1.16 | 5.46 |

The comparisons of velocity profiles between the experimental data and the computed results from the three turbulence models are presented in Figures 6.16, 4.37 and 4.38. WA2018-EB model has a slightly better prediction compared to the WA2017 model. Both models show better agreement with the experimental data compared to the result from SA model.

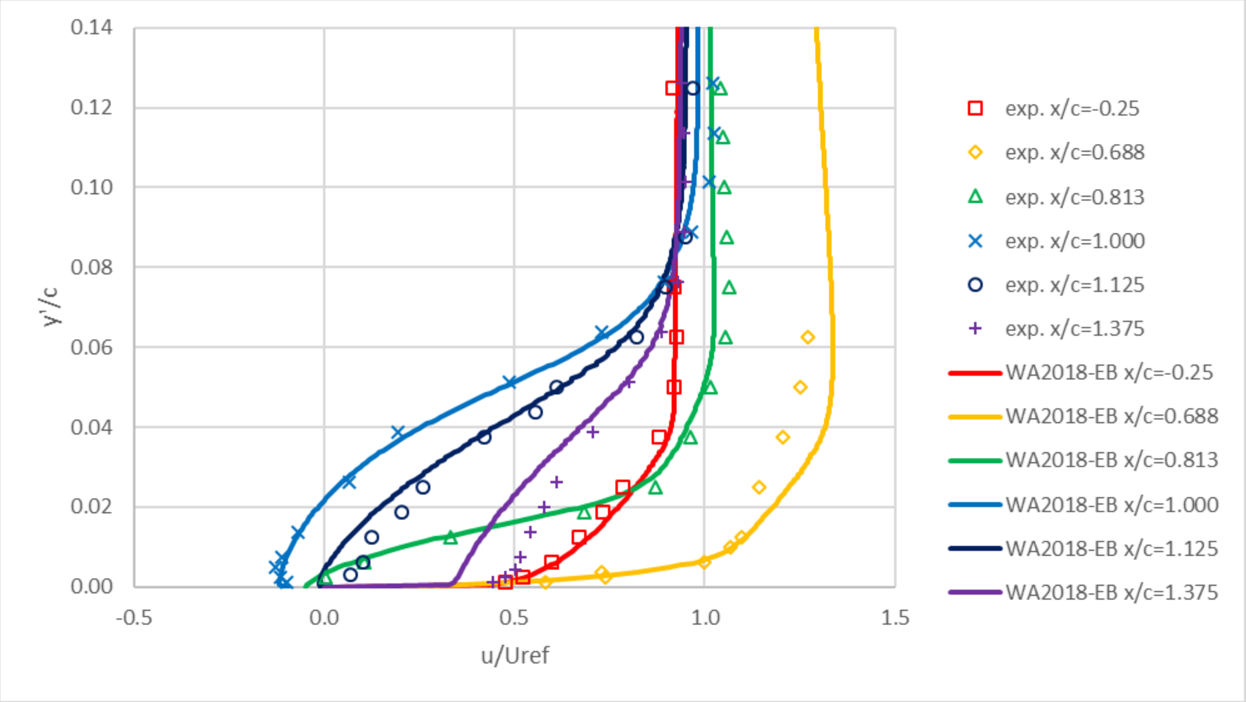

**Figure 6.16: Comparison of vertical velocity profiles computed from WA2018-EB model and experimental data at various locations on the axisymmetric bump.**

# Chapter 7: Summary and Future Work

## 7.1 Summary

The recently developed WA turbulence model has shown improved accuracy over the SA model and has been found to be competitive with SST *k-ω* model for a wide variety of wall-bounded and free shear layer flows [16]. A DES version of the WA model (designated as WA-DES model) has been developed in this dissertation and applied to several test cases, which include incompressible and compressible flows, two-dimensional and three-dimensional geometries, and a wide range of Reynolds numbers. WA-DES model is a hybrid model which combines the WA RANS model with LES; it improves the accuracy of simulation without significantly increasing the computational cost compare to the original WA RANS model. The computational results using WA-DES model show its potential for improved accuracy over the conventional eddy-viscosity RANS models without a substantial increase in the computational cost.

Following the development and validation of WA-DES model, WA-IDDES model is developed to further improve its accuracy and robustness. The WA-IDDES model generally improves the accuracy of the results compare to the WA model. However, the improvement is not always as much as the one obtained by the WA-DES model, especially when considering the prediction of skin friction distribution. However, WA-IDDES model has an advantage over the WA-DES model in getting rid of the grid-dependency of the computed solution. While DES models usually require multiple grid adjustments to make sure that both the RANS and LES parts of the simulation reside in proper regions, the IDDES model can easily run on a complex mesh with less attention required to determine the proper regions for refinement (RANS or LES). The robustness and reduction in development time makes the IDDES model more attractive especially for geometrically complex industrial applications. However, IDDES model loses simplicity compared to DES model by including several extra equations, which makes it harder to debug when problems occur in obtaining a solution. Overall, the WA-IDDES model offers a good alternative for accurate computation of wall-bounded separated turbulent flows compared to the eddy viscosity WA model, and overcomes several problems in WA-DES model.

A new version of the wall distance free Wray-Agarwal turbulence model with elliptic blending, designated as WA2018-EB has been developed by including zero strain-rate correction, wall distance free approach and elliptic blending. The model has been applied to compute a number of benchmark test cases from NASA TMR [20]. The results from WA2018-EB model are compared with the original WA model (WA2017) [16]. WA2018-EB is able to accurately calculate the log layer at all Reynolds number for flow in a channel showing excellent agreement with DNS data. In flows with wall bounded separation and reattachment, the predicted flow fields using the WA2018-EB model show closer agreement with the experimental data for pressure distribution, skin friction distribution, separation and reattachment points, and velocity profiles in the near wall region compared to the original WA2017 model.

## 7.2 Future Work: Density Variance Correction

### 7.2.1 Background and Motivation

High-speed compressible flows present a range of new problems to turbulence modeling. Generally, one and two-equation eddy-viscosity models are developed first for incompressible flows (subsonic free-shear flows and incompressible boundary layers), then an additional correction is applied to extend their use to compressible flows. These extensions are often derived from Morkovin's hypothesis, which states that compressibility affects the turbulence through variations in mean density, and that the density fluctuations $\rho'$ have little effect on turbulence. Experimental and numerical simulations have largely confirmed this hypothesis for moderate Mach numbers [50]. However, freestream flows with M > 3 and wall bounded flows with M > 4.5 have been shown to be clearly outside the range of this hypothesis. Therefore, turbulence model closures applied to hypersonic flows must account for the compressibility of turbulence through more than just mean density variations. The objective of density variance correction is to develop a transport equation that models the density variance ($\overline{\rho'^2}$), and pairing it with standard eddy-viscosity models to improve their accuracy across a wide range of Mach numbers especially for hypersonic flows for which standard compressibility corrections are not well-suited.

The goal of the future work is to pair the new density variance transport equation with newly developed WA model (designated as WA-DV) and test it on a variety of hypersonic flows.

### 7.2.2 Formulation of Density Variance Equation

The exact density variance equation can be derived from either the Reynolds or Favre equations. Favre averaged density variance equation is given in Eq. (51).

$$\frac{\partial \overline{\rho'^2}}{\partial t} + \frac{\partial \overline{\rho'^2} u_j}{\partial x_j} = -\overline{\rho'^2}\frac{\partial u_j}{\partial x_j} - 2\overline{\rho' u_j''}\frac{\partial \bar{\rho}}{\partial x_j} - \frac{\partial \overline{\rho'^2 u_j''}}{\partial x_j} - 2\bar{\rho}\overline{\rho'\frac{\partial u_j''}{\partial x_j}} + \overline{\rho'^2\frac{\partial u_j''}{\partial x_j}} \tag{51}$$

The second and third term on the right-hand side of Eq. (51) act as gradient transport. Both are modeled by the gradient hypothesis like the standard derivation of the modeled turbulent kinetic energy equation [51].

$$-2\overline{\rho' u_j''}\frac{\partial \bar{\rho}}{\partial x_j} = 2C_{\rho 1}\nu_t\frac{\partial \bar{\rho}}{\partial x_j}\frac{\partial \bar{\rho}}{\partial x_j} \tag{52}$$

$$-\frac{\partial \overline{\rho'^2 u_j''}}{\partial x_j} = \frac{\partial}{\partial x}\left[\left(\nu + \sigma_\rho \nu_t\right)\frac{\partial \overline{\rho'^2}}{\partial x_j}\right] \tag{53}$$

The last two terms act as destruction and involve density and dilatation fluctuations. They can be represented by a time scale defined as the ratio of turbulent kinetic energy *k* and turbulent dissipation $\epsilon$ [52]. According to assumptions in derivation of WA model [18], it can be further reduced to be represented by strain rate magnitude *S* as in Eq. (54).

$$-2\bar{\rho}\overline{\rho'\frac{\partial u_j''}{\partial x}}+\overline{\rho'^2\frac{\partial u_j''}{\partial x}}\sim-\frac{\epsilon}{k}\overline{\rho'^2}=\ -C_{\rho 2}\overline{\rho'^2}S \tag{54}$$

To account for the compressibility effects, *k*-*ε* equation is re-derived and includes an extra production term $f_{comp,k}$ [52]. WA model includes this term by making use of the original derivation from *k*-*ω* closure, and the new production term $f_{comp,R}$ in its *R*-equation is derived and is given in Eq. (55).

$$\begin{gathered}f_{comp,k}=C_{k1}\bar{\rho}\bar{a}^2\frac{\overline{\rho'^2}}{\bar{\rho}^2}\frac{\partial u_a}{\partial x_a}-C_{k2}\bar{\rho}\frac{\bar{a}^2}{k}\frac{\overline{\rho'^2}}{\bar{\rho}^2}\epsilon\\ f_{comp,R}=\bar{\rho}\left(\frac{\bar{a}}{\bar{\rho}}\right)^2\overline{\rho'^2}\left(C_{r1}\frac{\partial u_j}{\partial x_j}\frac{1}{S}-C_{r2}\right)\end{gathered} \tag{55}$$

The density variance equation and re-derived WA equation are obtained as:

$$\begin{aligned}&\frac{\partial\overline{\rho'^2}}{\partial t}+\frac{\partial\overline{\rho'^2}u_j}{\partial x_j}=\frac{\partial}{\partial x}\left[\left(\nu+\sigma_\rho\nu_t\right)\frac{\partial\overline{\rho'^2}}{\partial x_j}\right]-\overline{\rho'^2}\frac{\partial u}{\partial x}+2C_{\rho 1}\nu_t\frac{\partial\bar{\rho}}{\partial x_j}\frac{\partial\bar{\rho}}{\partial x_j}-C_{\rho 2}\overline{\rho'^2}S\\ &\bar{\rho}\frac{\partial R}{\partial t}+\bar{\rho}\frac{\partial u_jR}{\partial x_j}=\frac{\partial}{\partial x_j}\left[\bar{\rho}(\nu+\sigma_R R)\frac{\partial R}{\partial x_j}\right]+\bar{\rho}C_1RS+\bar{\rho}f_1C_{2k\omega}\frac{R}{S}\frac{\partial R}{\partial x_j}\frac{\partial S}{\partial x_j}\\ &\qquad-\bar{\rho}(1-f_1)C_{2k\varepsilon}R^2\left(\frac{\frac{\partial S}{\partial x_j}\frac{\partial S}{\partial x_j}}{S^2}\right)+\bar{\rho}\left(\frac{\bar{a}}{\bar{\rho}}\right)^2\overline{\rho'^2}\left(C_{r1}\frac{\partial u_j}{\partial x_j}\frac{1}{S}-C_{r2}\right)\end{aligned} \tag{56}$$

### 7.2.3 Calibration of Density Variance Equation

The implementation of density variance equation introduces five new constants. To calibrate them, numerical results are compared to experimental fluctuation measurement in a supersonic turbulent boundary layer [53]. Experimental data including Mach number, Reynolds number based on momentum thickness, momentum thickness, total pressure, total temperature, and boundary layer thickness at measurement locations are presented in Table 7.1 below. Temperature fluctuation profile measured is shown in Figure 7.1.

**Table 7.1: Experimental data of fluctuation measurement experiment [51].**

| Mach Number | Reynolds Number $Re_\theta$ | Momentum Thickness $\theta$ (inch) | Total Pressure $P_0$ (cm Hg) | Total Temperature $T_0$ (K) | Boundary Layer Thickness $\delta$ (inch) |
|---|---|---|---|---|---|
| 1.72 | $4 \times 10^4$ | 0.056 | 150 | 300 | 0.70 |
| 3.56 | $3.3 \times 10^4$ | 0.064 | 300 | 300 | 1.05 |
| 4.67 | $2.88 \times 10^4$ | 0.545 | 480 | 300 | 1.15 |

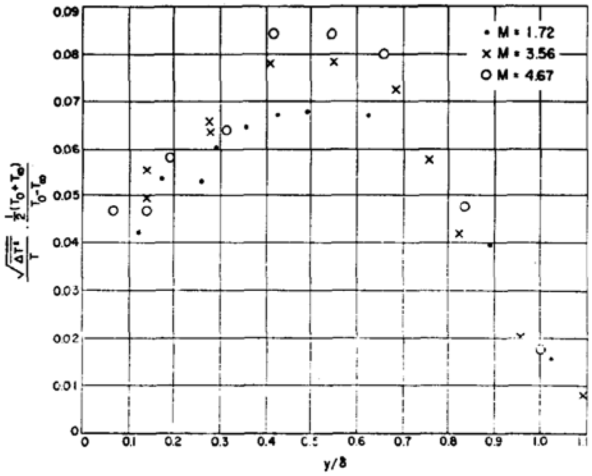

**Figure 7.1: Temperature profile in fluctuation measurement experiment [51].**

Since all the Mach numbers in Table 7.1 and Figure 7.1 are below 5, Morkovin's hypothesis is used to approximate the density fluctuation from temperature fluctuation as shown in Eq. (57).

$$\frac{\overline{\rho'^2}}{\bar{\rho}^2} \approx \left(\frac{T'}{\bar{T}}\right)^2 \tag{57}$$

Numerical results obtained at locations with three different boundary layer thickness should be used to calibrate the model constants of WA-DV model. After the calibration, the WA-DV model should be needed to compute several hypersonic flow test cases, such as the zero gradient high Mach number flat plate flow [20], Mach 7 Axisymmetric Shock Wave Boundary Layer

Interaction [54] and Mach 9 flow in a compression corner [55] to prove its ability in computing high-speed compressible flows.

# References

1. Spalart , P. R., Jou, W.-H., Strelets, M. and Allmaras, S.R., “Comments on the feas1ibility of LES for wings, and on a hybrid RANS/LES approach,” 1st AFOSR Int. Conf. On DNS/LES, Greyden Press, Columbus, OH, Aug 4-8, 1997.

2. Strelets, M., “Detached Eddy Simulation of Massively Separated Flows,” AIAA Paper 2001-0879, 2001.

3. Smagorinsky, J., “General Circulation Experiments with the Primitive Equations,”. Monthly Weather Review, Vol. 91(3), March 1963, pp. 99-164.

4. Germano, M., Piomelli, U., Moin, P., Cabot, W., “A dynamic subgrid-scale eddy viscosity model”. Physics of Fluids A, Vol. 3, No. 7, 1991, pp. 1760-1765.

5. Spalart, P. R., “Strategies for Turbulence Modeling and Simualations,” Int. J. Heat Fluid Flow, Vol. 21, 2000, pp. 252-263.

6. Singh, A. P., Medida, S., and Duraisamy, K., “Machine-Learning-Augmented Predictive Modeling of Turbulent Separated Flows over Airfoils”, AIAA Journal, Vol. 55, No. 7, 2017, pp. 2215-2227.

7. Corrigan, A., Camelli, F., Lohner, R., Wallin, J., “Running Unstructured Grid Based CFD Solvers on Modern Graphics Hardware,” Int. J. for Numerical Methods in Fluids, Vol. 66(2), pp. 221-229

8. Dakota theory manual, https://dakota.sandia.gov/sites/default/files/docs/6.6/Theory-6.6.0.pdf. [retrieved November 2017]

9. Stephanopoulos, K., Witte, I., Wray, T. J., and Agarwal, R. K., “Uncertainty Quantification of Turbulence Model Coefficients in OpenFOAM and Fluent for Mildly Separated Flows,” 46th AIAA Fluid Dynamics Conference, AIAA 2016-4401

10. Center for High Performance Computing website, https://www.mir.wustl.edu/research/research-support-facilities/center-for-high-performance-computing-chpc. [retrieved November 2017]

11. Travin, A., Shur, M., Strelets, M. and Spalart, P.R., “Detached-eddy simulations past a circular cylinder,” Flow Turbul. Combust., Vol. 63, 2000, pp. 293.

12. Jee, S., Shariff, K., “Detached-Eddy Simulation Based on the v2-f Model,” Seventh International conference on Computational Fluid Dynamics (ICCFD7), Big Island, Hawaii, July 9-13, 2012.

13. Spalart, P. R. and Allmaras, S. R, "A One Equation Turbulence Model for Aerodynamic Flows," AIAA Paper 1992-0439, 1992.

14. Menter, F. R., "Two-Equation Eddy-Viscosity Turbulence Models for Engineering Applications," AIAA J., Vol. 32, No. 8, August 1994, pp. 1598-1605.

15. Wray-Agarwal turbulence model, https://turbmodels.larc.nasa.gov/wray_agarwal.html. [retrieved November 2017]

16. Han, X., Wray, T. J., Agarwal, R. K., "Application of a New DES Model Based on Wray-Agarwal Turbulence Model for Simulation of Wall-Bounded Flows with Separation," AIAA Paper 2017-3966, June 2017.

17. Spalart, P., "Detached-Eddy Simulation," Annual Review of Fluid Mechanics, Vol. 41, 2009, pp. 181-202.

18. Wray, T. J., and Agarwal, R. K., "A New Low Reynolds Number One Equation Turbulence Model Based on a k-ω Closure," AIAA Journal, Vol. 53, No. 8, 2015, pp. 2216-2227.

19. Wray, A. A., "Hom02: Decaying isotropic turbulence." In A Selection of Test Cases for the Validation of Large-Eddy Simulations of Turbulent Flows, AGARD Advisory Report No 345, 1997.

20. NASA Langley Research Center Turbulence Modeling Resource, https://turbmodels.larc.nasa.gov. [retrieved November 2017]

21. Weighardt, K., and Tillman, W., "On the Turbulent Friction Layer for Rising Pressure," NACA TM-1314, 1951.

22. Ladson, C. L., Hill, A. S., and Johnson, Jr., W. G., "Pressure Distributions from High Reynolds Number Transonic Tests of an NACA 0012 Airfoil in the Langley 0.3-Meter Transonic Cryogenic Tunnel," NASA TM 100526, December 1987.

23. NPARC Alliance Verification and Validation Archive, https://www.grc.nasa.gov/WWW/wind/valid/whatsnew.html. [retrieved November 2017]

24. Bruice, C., and Eaton, J. K., "Experimental Investigation of Flow through an Asymmetric Plane Diffuser," Stanford Univ. Dept. of Mechanical Engineering, Thermoscience Division Rept. TSD-107, Stanford, CA, 1997.

25. Coles, D. and Wadcock, A. J., "Flying-Hot-Wire Study of Flow Past an NACA 4412 Airfoil at Maximum Lift," AIAA Journal, Vol. 17, No. 4, April 1979, pp. 321-329.

26. European Research Community on Flow, Turbulence and Combustion (ERCOFTAC) Database, http://cfd.mace.manchester.ac.uk/ercoftac. [retrieved November 2017]

27. Frohlich, J., Mellen, C. P., Rodi, W., Temmerman, L. and Leschziner, M. A., “Highly resolved large-eddy simulation of separated flow in a channel with streamwise periodic constrictions,” J. Fluid Mech. Vol. 526, pp. 19-66, 2005

28. Bachalo, W. D., and Johnson, D. A., “An Investigation of Transonic Turbulent Boundary Layer Separation Generated on an Axisymmetric Flow Model,” AIAA Paper 79-1479, 1979.

29. Wellborn, S.R., Reichert, B.A, and Okiishi, T.H., “An Experimental Investigation of the Flow in a Diffusing S-Duct,” AIAA Paper 92-3622, 28th Joint Propulsion Conference and Exhibit, Nashville, TN, 6-8 July 1992.

30. Wellborn, S.R., Okiishi, T.H., and Reichert, B.A, “A Study of Compressible Flow through a Diffusing S-Duct,” NASA Technical Memorandum 106411, December 1993.

31. Menter, F. R., Kuntz, M., “Adaptation of eddy-viscosity turbulence models to unsteady separated flow behind vehicles,” The Aerodynamics of Heavy Vehicles: Trucks, Buses, and Trains, 2002, pp. 339-352.

32. Spalart, P. R., Deck, S., Shur, M. L., Squires K. D., Strelets, M. K. and Travin, A., “A new version of detached-eddy simulation, resistant to ambiguous grid densities,” Theor. Comput. Fluid Dyn., Vol. 20, 2006, pp. 181-195.

33. Shur, M. L., Spalart, P. R., Strelets, M. K., Travin, A. K., “A hybrid RANS-LES approach with delayed-DES and wall-modeled LES capabilities,” Int. J. Heat Fluid Flow, Vol. 29, 2008, pp. 1638–1649.

34. Gritskevich, M. S., Garbaruk, A. V., Schütze J. and Menter, F. R., “Development of DDES and IDDES Formulations for the k-ω Shear Stress Transport Model,” Flow Turbul. Combust., Vol. 88, 2012, pp. 431-449.

35. Spalart, P. R., “Young-Person's Guide to Detached-Eddy Simulation Grids,” NASA Technical Report, NASA/CR-2001-211032, NAS 1.26:211032.

36. Bentaleb, Y., Lardeau, S., and Leschziner, M. A., “Large-eddy simulation of turbulent boundary-layer separation from a rounded step,” Journal of Turbulence, Vol. 13, No. 4, 2011, pp. 1-28.

37. Lardeau, S., and Billard, F., “Development of an elliptic-blending lag model for industrial applications,” 54th AIAA Aerospace Sciences Meeting, San Diego, CA, 2016.

38. M. M. Rahman, R. K. Agarwal, M. J. Lampinen and T. Siikonen, "Wall-Distance-Free Version of Spalart–Allmaras Turbulence Model," AIAA J., Vol. 53, No. 10, 2015, pp. 3016-3027.

39. Goldberg, U., Peroomian O., and Chakravarthy, S., "A Wall-Distance-Free k-ε Model With Enhanced Near-Wall Treatment," J. of Fluids Engineering, Vol. 120, 1998.

40. Goldberg, U., Batten, P., "A wall-distance-free version of the SST turbulence model," Engineering Applications of Computational Fluid Mechanics, Vol. 9(1), 2015, pp. 33-40.

41. Durbin, P. A., Mansour, N. N., and Yang, Z., "Eddy Viscosity Transport Model for Turbulent Flow," Physics of Fluids, Vol. 6(2), 1994, pp. 1007-1015.

42. Rahman, M. M., Siikonen, T., and Agarwal R. K., "Improved Low Re-number One–Equation Turbulence Model," AIAA Journal, Vol. 49, 2011, pp. 735-747.

43. Rahman, M. M., Wallin, S., and Siikonen, T., "Exploring k and ω with R–Equation Model Using Elliptic Relaxation Function," Flow, Turbulence and Combustion, Vol. 89, 2012, pp. 121–148.

44. Elkhoury, M., "On the Eddy Viscosity Transport Models with Elliptic Relaxation," Journal of Turbulence, Vol. 18(3), pp. 2017, pp. 240-259.

45. Menter, F. R., "Eddy Viscosity Transport Equations and Their Relation to the k-ε Model," Journal of Fluids Engineering Vol. 119(4), 1997, pp. 876-884.

46. Menter, F. R. and Egorov, Y., "The Scale-Adaptive Simulation Method for Unsteady Turbulent Flow Predictions. Part 1: Theory and Model Description," Flow, Turbulence, and Combustion, Vol. 85, 2010, pp. 113-138.

47. Abdol-Hamid, K. S., Carlson, J.-R., and Rumsey, C. L., "Verification and Validation of the k-kL Turbulence Model in FUN3D and CFL3D Codes," NASA/TM-2015-218968, November.

48. Patel, V. C., Rodi, W., Scheuerer, G., "Turbulence models for near-wall and low Reynolds number Flow," AIAA J., Vol. 23, No. 9, 1985, pp. 1308-1319.

49. Lee, M., and Moser, R. D., "Direct Numerical Simulation of Turbulent Channel Flow Up to Re_tau = 5200," Journal of Fluid Mechanics, Vol. 774, 2015, pp. 395-415.

50. So, R. M. C., Gatski, T. B., and Sommer, T. P., "Morkovin Hypothesis and the Modeling of Wall-Bounded Compressible Turbulent Flows," AIAA Journal, Vol. 36, No. 9, 1998, pp. 1583-1592.

51. Tennekes H., and Lumley J. L., A First Course in Turbulence, 3rd ed., The MIT Press, Cambridge, Massachusetts, and London, England, Chapter 3, 1974.

52. Taulbee D., and VanOsdol J., “Modeling Turbulent Compressible Flows: The Mass Fluctuating Velocity and Squared Density,” AIAA Paper 91-0524, 1991.

53. Beresh, S. J., Henfling, J. F., Spillers, R. W., and Pruett, B. O. M., “Fluctuation measurements in a supersonic turbulent Boundary Layer,” Physics of Fluids 2, 1959, pp. 290.

54. Kussoy, M. I. and Horstman, C. C., “Documentation of Two- and Three-Dimensional Hypersonic Shock Wave Boundary Layer Interaction Flows,” NASA TM 101075, January 1989.

55. Coleman, G. T., Stollery J. L., “Heat transfer from hypersonic turbulent flow at a wedge compression corner,” J. Fluid Mech., Vol. 56(4), 1972, pp. 741-752.

# Xu Han

## EDUCATION

**Ph.D. in Mechanical Engineering**, Department of Mechanical Engineering and Materials Science, Washington University in St. Louis, Saint Louis, MO. 2013-2018

**B.S. in Mechanical Engineering and Automation**, School of Mechanical Science and Engineering, Huazhong University of Science & Technology, Wuhan, China. 2009-2013

## PUBLICATIONS

**Han, X.,** Wray, T. J., Fiola, C., and Agarwal, R. K., "Computation of Flow in S-Ducts with Wray-Agarwal One-Equation Turbulence Model," Journal of Propulsion and Power, Vol.31, No. 5, 2015, pp. 1338-1349.

**Han, X.,** Wray, T. J., and Agarwal, R. K., "Application of a New DES Model Based on Wray-Agarwal Turbulence Model for Simulation of Wall-Bounded Flows with Separation," AIAA Aviation Meeting, Denver, CO, June 2017.

**Han, X.,** Rahman, M. M., and Agarwal, R. K., "Development and Application of a Wall Distance Free Wray-Agarwal Turbulence Model," AIAA Scitech Meeting, Kissimmee, FL, January 2018.

**Han, X.,** and Agarwal, R. K., "Application of a New IDDES Model Based on Wray-Agarwal Turbulence Model for Simulation of Wall-Bounded Flows with Separation," AIAA Scitech Meeting, Kissimmee, FL, January 2018.

**Han, X.,** Rahman, M. M., and Agarwal, R. K., "Wall-Distance Free Wray-Agarwal Turbulence Model with Elliptic Blending," AIAA Aviation Meeting, Atlanta, GA, June 2018.

**Han, X.,** and Agarwal, R. K., "A Density Variance Correction Based on Wray-Agarwal Turbulence Model for Simulation of Hypersonic Flows," AIAA Aviation Meeting, Atlanta, GA, June 2018.

## PROFESSIONAL MEMBERSHIP

American Institute of Aeronautics and Astronautics (AIAA)